DESIGN AND VERIFICATION OF AN OPTICAL SYSTEM TO INTERROGATE DERMALLY-IMPLANTED MICROPARTICLE SENSORS

A Dissertation

by

RUIQI LONG

Submitted to the Office of Graduate Studies of
Texas A&M University
in partial fulfillment of the requirements for the degree of

DOCTOR OF PHILOSOPHY

May 2012

Major Subject: Biomedical Engineering

Design and Verification of an Optical System to Interrogate

Dermally-implanted Microparticle Sensors

DESIGN AND VERIFICATION OF AN OPTICAL SYSTEM TO INTERROGATE DERMALLY-IMPLANTED MICROPARTICLE SENSORS

A Dissertation

by

RUIQI LONG

Submitted to the Office of Graduate Studies of
Texas A&M University
in partial fulfillment of the requirements for the degree of

DOCTOR OF PHILOSOPHY

Approved by:

Chair of Committee,	Michael J. McShane
Committee Members,	Javier A. Jo
	Kenith E. Meissner
	Won-jong Kim
Head of Department,	Gerard L. Coté

May 2012

Major Subject: Biomedical Engineering

ABSTRACT

Design and Verification of an Optical System to Interrogate Dermally-implanted Microparticle Sensors. (May 2012)

Ruiqi Long, B.S., Zhejiang University

Chair of Advisory Committee: Dr. Michael J. McShane

Diabetes mellitus affects 25.8 million Americans (8.3%) and over 300 million people worldwide. Clinical trials indicate that proper management of blood glucose levels is critical in preventing or delaying complications associated with diabetes. Thus, there is a common need to monitor and manage blood glucose properly for people with diabetes. However, the patients' compliance for recommended monitoring frequency is low due to the pain and inconvenience of current standard finger-pricking tests. To promote patient adherence to the recommended self-monitoring frequency, non-invasive/ minimally invasive glucose testing approaches are needed. Luminescent microparticle sensor is an attractive solution. For these sensors to be deployed *in vivo*, a matched optical system is needed to interrogate dermally-implanted sensors. This research project investigated the light propagation in skin and the interaction with implants using Monte Carlo modeling. The results of the modeling were used to design an optical system with high interrogation and collection efficiency (40~300 times improvement). The optical system was then constructed and evaluated experimentally. A stable skin phantom mimicking the optical properties of human skin was developed as a permanent evaluation medium to minimize the use of animals. The optical properties of the skin phantom matched the maximum published values of human skin in scattering and absorption over the spectral range of 540~700nm in order to avoid overestimation of the capability of the system. The significant photon loss observed at the

connection between the designed system and a commercial spectrometer was overcome using two optimized designs: a two-detector system and a customized low-resolution spectrometer system. Both optimization approaches effectively address the photon loss problem and each showed good SNR (>100) while maintaining a sufficient system resolution for use with fluorescent materials. Both systems are suitable for luminescence measurement, because broad bands of the luminescent spectrum are of interest. In the future, either system can be easily modified into a more compact system (e.g. handheld), and it can be directly coupled to an analog-to-digital converter and integrated circuits offering potential for a single compact and portable device for field use with luminescent diagnostic systems as well as implanted sensors.

DEDICATION

To my family

ACKNOWLEDGEMENTS

I would like to thank Dr. McShane for his immeasurable considerations, support and help on my research during my graduate study in Texas A&M University. I want to express my sincere appreciation to NIH (R01-EB000739) and Dr. Gerard L. Coté (BRP) for the financial support. I also would like to thank Dr. Kenith Meissner, Dr. Javier Jo and Dr. Won-jong Kim for serving on my advisory committee.

I am grateful to my colleagues: Brad Collier, Dustin Ritter, Jason Roberts, Jaebum Park, Ashvin Nagaraja, Rachel Unruh, Merene Philip, and Dr. Saurabh Singh for their priceless support and help. I also want to thank Dr. Jason Hirshburg for the help with integrating sphere and Paul Kauffman for the help with skin phantoms.

I would like to thank my parents, Xiaodong Zeng and Tianmin Long. I would not have finished this dissertation without their support and encouragement.

I would also like to thank my husband, Zhiyang Wang, for always standing beside me and support me. His encouragement and help are sources of my inspirations and motivations during this whole process.

NOMENCLATURE

I	intensity of transmitted light
I_0	intensity of incident light
T	transmission of light
μ_a	absorption coefficient
μ_s	scattering coefficient
μ_s'	reduced scattering coefficient
σ	absorption cross section
P	density of absorbers
l	path length of light
g	anisotropy factor
χ	a random variable
ξ	a computer generated random number
s	photon's free path length
μ_t	interaction coefficient
M_T	diffuse transmittance
M_R	diffuse reflectance
M_C	collimated transmittance
w	weight of a photon in Monte Carlo modeling
n	refractive index
λ	wavelength
D	diameter of the spheres of sensor model (μm)
S	center-to-center spacing of the spheres of sensor model (μm)

C	concentrations of glucose (mg/dL)
t	time
T	diffuse transmission measured with an integrating sphere
T_0	diffuse transmission without a sample
R	diffuse reflection measured with an integrating sphere
R_0	diffuse reflection without a sample
U	collimated transmission
U_0	collimated transmission without a sample
N	groove density of a grating (1/mm)
N’	total number of grooved illuminated
β	diffracted angle

TABLE OF CONTENTS

Page

Page

Page

LIST OF FIGURES

LIST OF TABLES

1. INTRODUCTION

1.1 Significance

Disturbance of biochemical substances in the body may indicate or cause medical or pathological conditions. For example, hypoxia (low oxygen) has been implicated in central nervous system pathology in a number of disorders including stroke, head trauma, neoplasia and neurodegenerative disease [1]. Elevated levels of uric acid accumulation can lead to gout, a painful arthritis; iron deficiency increases perinatal risks for mothers and overall infant mortality. Deficiency of iodine can cause mental retardation and brain damage [2]. Elevated lactate levels (>4mM) have been shown to be associated with circulatory failure and cardiac arrest [3]. Hypercholesterolemia is strongly associated with cardiovascular disease [4]. High levels of blood glucose may mark diabetes. To facilitate diagnosis or management of these medical conditions, it is important to develop technologies for sensing these biochemicals.

Among these available biochemical sensing technologies, glucose sensing is of special significance, because of the epidemic of diabetes. Diabetes mellitus affects 23.6 million Americans (7.8%) and over 300 million people worldwide; moreover, this total is expected to reach close to 500 million within 20 years [5, 6]. There are three main types of diabetes. Type 1 diabetes is called insulin-dependent diabetes and it results from the body's failure to produce insulin. Type 1 diabetes accounts for 5-10% of all diagnosed diabetes. Type 2 diabetes is called non-insulin-dependent diabetes. It usually results from insulin resistance, a condition in which cells fail to use insulin properly. This type of diabetes accounts for 90-95% of all diagnosed diabetes. Gestational diabetes is temporary and occurs during pregnancy. However, women who

---

This dissertation follows the style of Biomedical Optics Express.

have had gestational diabetes have a 40-60% chance of developing diabetes in the next 5-10 years. There are many serious complications associated with hyperglycemia that results from lack of glucose control due to diabetes, and the complications include cardiovascular disease, blindness, kidney damage, stroke, hypertension, lower-limb amputations, nephropathy, neuropathy, periodontal, gingivitis, cataract formation, and pregnancy difficulties [6, 7].

People with diabetes can still lower the occurrence or delay the progression of these complications by controlling blood glucose properly. People can use the results of glucose monitoring to make decisions about physical activity, food, and medications in order to control their glucose levels [8]. Clinical trials prove that proper management of blood glucose levels is critical in preventing or delaying the complications [9-11]. Therefore, all persons with diabetes share a common need to monitor and manage their blood glucose state properly.

The current gold-standard methods for patients to monitor blood glucose levels by themselves is the "finger-pricking" test, which requires lancing the skin to extract a blood sample that is then examined by a device using disposable test strips. This method is inconvenient, painful and introduces potential infections. Therefore, compliance to the recommended blood testing frequency (at least 3 times/day) is typically poor due to inconvenience and pain [12-14]. To enable better glucose control, the continuous glucose monitoring system (CGMS) has been recently developed to be commercially available. The purpose of CGMS is to provide continuous information of trends, magnitude and fluctuations of glucose instead of 3-4 blood measurements per day. These systems use a tiny sensor inserted into the skin to check glucose concentrations in tissue fluid. The sensor stays in place for several days to a week and then must be replaced. CGMS devices produced by DexCom (STS® Seven system), and Medtronic (Guardian® RT) have been approved by the U.S. Food and Drug Administration and are available for prescription. However, these devices still require

percutaneous insertion, which introduces potential infection pathway, and they have accuracy issues. Moreover, CGMS is **not** intended to replace day-to-day long-term glucose monitoring by patients themselves. Therefore, a less painful and more convenient way to facilitate self-monitoring of blood glucose is needed to promote patient adherence to recommended self-monitoring glucose testing. A number of studies about noninvasive/minimally-invasive glucose sensors are being pursued worldwide. Noninvasive/minimally-invasive sensing technologies are not only important to people with diabetes, but also are effective platform technologies that are critical for monitoring of other biochemical substances or nutrients to assess overall health [2].

1.2 Background

Currently, many potentially less invasive optical sensing technologies are under investigation including absorption spectroscopy, polarimetry, Raman spectroscopy, and fluorescence/phosphorescence [2]. Among these sensing technologies, fluorescence-based glucose sensing has the advantage of being highly sensitive and highly specific to the target analyte. Combinations of highly sensitive luminescence transduction methods with fiber-optic technology have shown particular promise [15-19]. These devices generally employ a probe consisting of a luminescence chemical assay immobilized within a selectively permeable membrane at the tip of an optical fiber. However, these fiber-optic transducers are still invasive during each measurement and have not been proven to meet the stability or reliability requirements for long-term in vivo functionality [20]. Dermally implanted luminescence-based microparticle biosensors are attractive alternatives, because the sensing chemistry is detached from the fiber tip, which enables completely noninvasive monitoring *in vivo* [2, 21-24].

The McShane group has previously reported several different luminescent chemo-optical transducer platforms that may meet the needs of such implantable biosensors; these include

examples of glucose sensors based on self-assembled hybrid microparticles and microcapsules [25-29]. One of these systems is based on the enzymatic oxidation of glucose catalyzed by the glucose oxidase (GOX) enzyme (Glucose+O_2+H_2O →Gluconic Acid+H_2O_2), which consumes oxygen as a co-substrate [29, 30]. Microparticle sensors are fabricated by loading glucose oxidase and immobilizing Pt(II) octaethylporphine (PtOEP) (a phosphorescent dye readily quenched by oxygen) inside the particles, and Rhodamine B-doped multilayer nano-film coating on the surfaces of microparticles provides reference emission, as well as transport control. Because oxygen inside each microparticle is depleted in proportion to glucose concentration, glucose can be indirectly monitored by measurement of PtOEP emission, which senses oxygen levels. Thus far, reaction-diffusion modeling and *in vitro* results suggest that these sensor systems can achieve adequate sensitivity, reliability, and longevity for long-term monitoring *in vivo* [29-32].

However, to deploy and interrogate luminescence-based dermally implanted sensors in vivo for on-demand monitoring, a number of key technical hurdles must be overcome. The microparticles must be engineered to be biocompatible, stable and produce signals strong enough for trans-dermal measurements. Assuming that this can be accomplished, it is also necessary to design a matched optoelectronic system to interrogate our dermally-implanted microparticle sensors. This system needs to be compact, portable, and of high efficiency to deliver excitation light, collect luminescence, and measure luminescence. A bifurcated optical fiber bundle is commonly used to deliver excitation light and to collect luminescence from a scattering medium, but the collection efficiency is limited because locations for the delivery of excitation light and those for collection of the luminescence are separate, thus the loss of luminescence, where the excitation light goes in is inevitable. To our knowledge, there is no commercial product or research report of a hardware design with high efficiency that is suitable for interrogation of

dermally-implanted sensors. The aim of this research was to develop a hardware system that will overcome the shortcomings of current bifurcated optical fiber.

1.3 Organization of sections

The sections of this dissertation have been organized so that the disseminated material is presented in a clear and logical sequence. Section 2 provides the theory of optical properties and Monte Carlo modeling for luminescence photon transportation in tissue. Section 3 is dedicated to modeling photon transportation in skin and the interaction with implants. Section 4 describes the optical design of the hardware system for sensor interrogation based on the modeling results obtained from the study in Section 3, and the corresponding experimental evaluation that was performed. This section also describes a skin phantom mimicking the optical properties of skin, which was developed as an evaluation medium for hardware testing. Section 5 focuses on the optimization work of the hardware system designed in Section 4 due to the inevitable photon loss observed during system evaluation performed in the last section. Section 6 concludes the work presented in this dissertation and discusses the implications of the research, and proposes future work which can aid in advancing this system to the next level of application.

2. THEORY OF TISSUE OPTICS AND MONTE CARLO MODELING

2.1 Optical properties

Optical properties of tissues are expressed in optical parameters such as absorption coefficient (μ_a), scattering coefficient (μ_s), anisotropy factor (g), refractive index (n), effective attenuation coefficient (μ_{eff}) and so on. The primary optical parameters used in all types of modeling for photon propagation in tissue are μ_a, μ_s, g, and n. To simulate luminescence, the quantum yield (Φ) will be used. These parameters characterize photon propagation in tissue, and they are obtained by calculating the measurement of observable quantities such as reflection, and transmission, etc. [33]

2.1.1 Absorption

The absorption process involves the interaction of the molecule in the ground state with a photon to promote an electron from a lower energy to a higher energy molecular orbital [34]. In biological tissues, there are several major absorbers. Protein and DNA are the main ultraviolet-absorbers, and the absorption increases as the wavelength gets shorter. Water is strong infrared absorbers and the absorption increases with longer wavelength. Whole blood is a strong absorber in the red-NIR regime, but the volume fraction is a few percent in tissue, thus the average absorption affecting light propagation in tissue is moderate except in blood vessels. Melanosomes are strong absorbers, as well, and most melanosomes are in epidermis and it varied a lot among different types of skin. Compared with other wavelength band, the absorption at red-NIR is relatively low, therefore, this region is called the diagnostic and therapeutic window [35, 36].

The absorbance of a substance is proportional to the concentration of absorbing species (Beer's law) in a substance of path-length (l) traversed by incident light (Lambert's law) [34]. The Beer-Lambert law states that there is a logarithmic dependence between the transmission (T) of light through a substance and the product of the absorption coefficient (μ_a) [length^{-1}] of the substance and the distance the light travels through the substance (l) [37], which is shown as in Equation (1). The absorption coefficient can be written as a product of a molar absorptivity (ε) of the absorber and the concentration of absorbers in the material, or it can be written as the product of absorption cross section (σ) and the (number) density (P) of absorbers. The absorption coefficient (μ_a) is defined as the probability of photon absorption per unit infinitesimal path-length [38]. Experimentally, the units for absorption coefficient (mm^{-1} or cm^{-1}) are inverse length. According to Beer-lambert law, the relationship between the intensity of incident light (I_0) and transmitted light (I) is as below.

$$T = \frac{I}{I_0} = e^{-\mu_a l} = e^{-\sigma P l} \tag{1}$$

2.1.2 Luminescence

Photo-luminescence is a radiative transition resulting from absorption of photons. There are two types of photo-luminescence: fluorescence and phosphorescence [39]. The Jablonski diagram (Figure 1) shows that there are various transitions open to the excited state after population to the ground state. In Figure 1, the solid arrows are radiative transitions as occurring by absorption or emission of a photon and dashed arrows represent non-radiative transitions. Internal conversion and intersystem crossing are two types of non-radiative transitions. Internal conversion occurs between states of the same spin multiplicity. A molecule that is directly excited into a state which is higher than S_1 will relax by internal conversion to S_1 state before emission can occur. Intersystem crossing (S_1 to T_1) is a non-radiative transition between states of different spin multiplicity and occurs via inversion of the spin of the excited electron [34]. Fluorescence takes place on the nanosecond scale and always emitted from the states of zeroth vibrational level of the first excited singlet state (S_1). Phosphorescence is originated from the triplet state (T_1). Once the molecule has reached triplet state, it will reside for a certain time (more than microseconds) before it decays to the ground state. This is because of the spin-forbidden transitions involved in the excited singlet-triplet and triplet-singlet (ground state) transitions. Therefore, the phosphorescence has longer lifetime [40].

Quantum yield (Φ) of luminescence is defined as the ratio of number of luminescence photon emitted to the number of photons that absorbed. The maximum luminescence quantum yield is 1, which means every photon absorbed results in a photon emitted. Compounds with quantum yield of 0.1 are still considered to be highly fluorescent. [41]

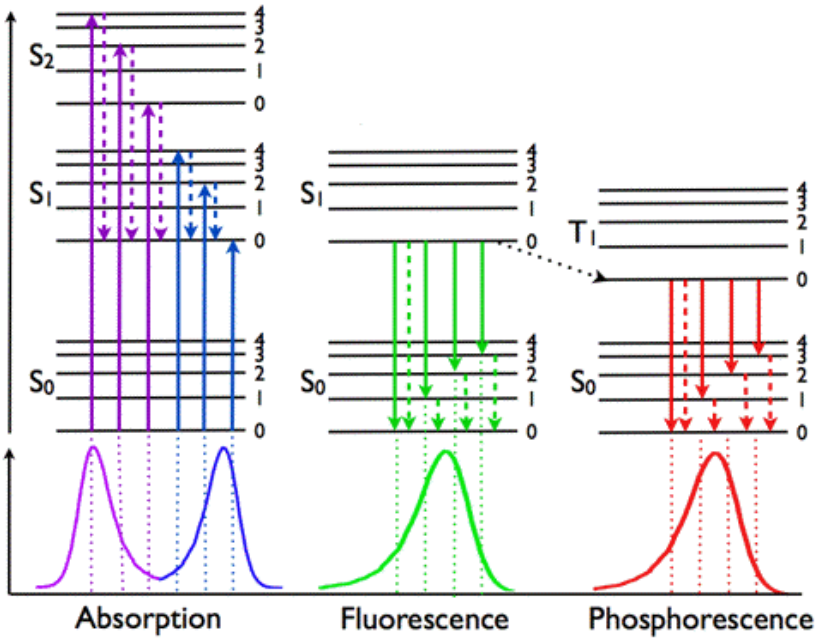

Figure 1. Jablonski diagram [40]

2.1.3 Scattering

Scattering of light is a general physical phenomenon where photons are forced to deviate from a straight trajectory by one or more localized non-uniformities in the medium through which they pass [42]. Light scattering occurs in media that contains variations in the refractive index (*n*), and such fluctuations can be discrete particles (scatterers) or more continuous variations in refractive index [43]. In biological tissues, there are many ultrastructures which can be scatterers. Membranes, collagen fibers, mitochondria nuclei, etc. are all biological scatterers. Scattering of light by the ultrastructres on the same size scale as wavelength can be described by Mie Theory, and structures which are much smaller than the wavelength can be described by Rayleigh scattering [44].

The scattering coefficient (μ_s) is defined as the probability of photon scattering per unit infinitesimal path-length [38]. Experimentally, the units for scattering coefficient (mm^{-1} or cm^{-1}) are inverse length. The angular dependence of scattering is called the scattering function, p(θ), which describes the probability of a photon scattering into a solid angle oriented at an angle (θ) relative to the photon's original trajectory. The Henyey-Greenstein scattering function is an expression which mimics the angular dependence of light scattering by small particles, which was initially used to describe scattering of light by interstellar dust clouds. This scattering function has proven to be useful in approximating the angular scattering dependence of single scattering events in biological tissues [45]. The Henyey-Greenstein function is as below in Equation (2):

$$p(\cos\theta) = \frac{1 - g^2}{2(1 + g^2 - 2g\cos\theta)^{3/2}} \tag{2}$$

g is the anisotropy factor and it is dimensionless. It is a measure of the amount of forward direction retained after a single scattering event. It is defined as the expectation value for cos(θ) as demonstrated in Equation (3), θ is the deflection angle from the original trajectory.

$$g = \int_0^{\pi} 2\pi p(\theta)\cos\theta\sin\theta d\theta = <\cos\theta> \tag{3}$$

2.1.4 Mean free path

In optics, the mean free path is the average distance covered by a moving photon between successive impacts [46] which modify its direction or energy or other properties [47]. When photons travel in biological tissues, the mean free path between photon-tissue interaction sties is

10-1000μm, and 100 μm is a typical value in the visible spectrum [33, 38]. The interaction coefficient μ_t is the probability of photon interaction per unit infinitesimal [38]. The interaction coefficient μ_t is equal to $\mu_a+\mu_s$, thus a mean free path between photon-tissue interaction sites is $1/\mu_t$, since μ_a and μ_s describe the average number of absorption and scattering events happening within a unit length.

2.2 Theory of Monte Carlo modeling

2.2.1 Sampling random variables

Monte Carlo modeling relies on the random sampling of variables from pre-defined probability distributions. A random variable χ is needed by modeling of photon propagation in medium. This variable can be the variable step size of a photon or the angle of deflection due to scattering [38]. The probability density function defines the distribution of χ over the interval (a,b) is as below in Euqation (4):

$$\int_a^b p(\chi) d\,\chi = 1 \tag{4}$$

To simulate photon propagation, a value for χ will be chosen repeatedly and randomly based on a pseudo-random number generator. A computer can provide a random variable (ξ) that is uniformly distributed over the interval (0,1). The cumulative distribution function of this uniformly distributed random variable is as below in Equation (5):

$$F(\xi) = \begin{cases} 0 & if\ \xi \leq 0 \\ \xi & if\ 0 < \xi \leq 1 \\ 1 & if\ \xi > 1 \end{cases} \tag{5}$$

To sample a non-uniformly distributed function p(χ), χ=f(ξ) is assumed to be a non-decreasing function that maps $\xi \in (0,1)$ to $\chi \in (a,b)$. The variables ξ and χ have a one-to-one mapping. This mapping approach leads to the equality of probabilities as below.

$$P\{f(0) < \chi \leq f(\xi_1)\} = P\{0 < \xi \leq \xi_1\} \tag{6}$$

If f(0)=a and f(ξ)= χ_1, thus $F_\chi(\chi_1)=F_\xi(\xi_1)$

Thus , Equation (7) can be converted into:

$$\int_a^{\chi_1} p(\chi)d\chi = F_\chi(\chi_1) = F_\xi(\xi_1) = \xi_1 \tag{7}$$

2.2.2 Moving photons

When the photon is launched or leaving the boundary, if the refractive index mismatch at the interface, specular reflection occurs. Specular reflectance (R_{spe}) can be calculated by Fresnel equation.

$$\int_a^{\chi_1} p(\chi)d\chi = F_\chi(\chi_1) = F_\xi(\xi_1) = \xi_1 \tag{8}$$

$$R_{spe} = \left(\frac{n_1 \cos\theta_i - n_2 \cos\theta_t}{n_1 \cos\theta_i + n_2 \cos\theta_t}\right)^2 \tag{9}$$

Similarly, transmittance (T_{spe}) is:

$$T_{spe} = 1 - R_s \tag{10}$$

In equation (9), n_1 and n_2 are the refractive index of medium where incident light and transmitted light travels. θ_i and θ_t are the angles of incident light and refracted light.

The step size of photons is sampled based on the probability distribution of photon's free path s (s>0). According to the definition of interaction coefficient μ_t, which is the probability of interaction per unit path-length in the interval (s',s'+ds'), thus the equation describes μ_t is as below [38]:

$$\mu_t = \frac{-dP\{s \geq s'\}}{P\{s \geq s'\}ds'} \tag{11}$$

This cumulative distribution function can be assigned to the uniformly distributed random number ξ. Therefore Equation (11) can be converted to:

$$s' = -\frac{ln(1-\xi)}{\mu_t} \tag{12}$$

And after substituting ξ for 1- ξ, the photon step size is as below. Therefore, the photon step size (s) can be sampled by a random value (ξ) generated by computer.

$$s = -\frac{ln(\xi)}{\mu_t} \tag{13}$$

Because the statistical average of –ln(ξ) : <-ln(ξ)>=1, the mean free path between photon-tissue interaction is $1/\mu_t$. Once the photon step size is sampled, the photon is ready to be moved in a 3-D way.

2.2.3 Photon absorption

After the photon takes a step, the attenuation of the photon weight due to absorption will be calculated. The fraction of the attenuated photon's weight ($_{\Delta}w$) is the ratio of μ_a to μ_t. Thus the updated photon's weight is [38] :

$$w' = w - \Delta w = w(1 - \frac{\mu_a}{\mu_t}) \tag{14}$$

2.2.4 Photon scattering

After the photon has been moved and the photon's weight has been updated, the photon is ready to be scattered. The deflection angle, $\theta \in [0, \pi)$ and azimuthal angle $\psi \in [0,2\pi)$ will be sampled. The probability distribution p(cosθ) for the cosine of deflection angle (θ) is described by Henyey-Greenstein function. Anisotropy factor (g) equals <cosθ>, thus g=0 indicates isotropic scattering and g=1 indicates very forward scattering. The choice for cosθ can be expressed as a function of random number ξ [38].

$$\cos\theta = \begin{cases} \frac{1}{2g}\left[1 + g^2 - \left(\frac{1 - g^2}{1 - g + 2g\xi}\right)^2\right] & if\ g > 0 \\ 2\xi - 1 & if\ g = 0 \end{cases} \tag{15}$$

Because the azimuthal angle (ψ) is uniformly distributed , thus it is sampled by

$$\psi = 2\pi\xi \tag{16}$$

2.2.5 Luminescence propagation

The luminescence illumination at each step for each excitation and each emission wavelength is calculated [48] using the equation below:

(17)

$$E_l = E\Phi \mathrm{m}(1 - e^{-\mu_{ax} \cdot s})$$

E is the excitation energy at the previous step, Φ is the quantum yield at excitation wavelength ; m is the emission factor for emission wavelength that is normalized from emission spectrum; μ_{ax} is the absorption coefficient of excitation wavelength, and l is the previous step size before luminescence takes place. After emission, the luminescence photon goes through the absorption and scattering in the medium which is the same process as excitation photons (Figure 2).

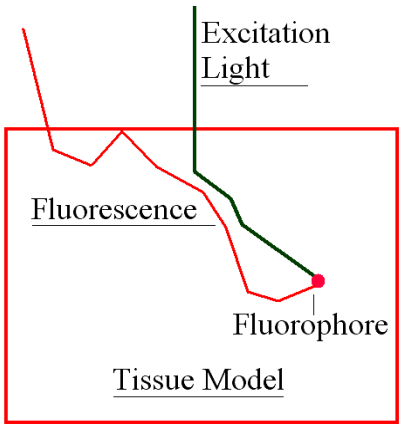

Figure 2. Scheme of Monte Carlo fluorescence modeling

2.2.6 Photon termination [38]

A photon can be terminated naturally by escaping from the medium. For a photon still propagating which has such little weight can occupy a lot computation resource. Therefore, proper photon termination must be executed to conserve energy without compromising the

distribution of photon energy deposition. The roulette technique is used to terminate photon. The roulette give the photon one chance in m of surviving with a weight of mw. If the photon does not survive, its weight is reduced to zero and it is terminated.

$$W = \begin{cases} mw & if\ \xi \leq 1/m \\ 0 & if\ \xi > 1/m \end{cases} \tag{18}$$

3. INVESTIGATION OF PHOTON TRANSPORTATION AND INTERACTION WITH IMPLANTS IN SKIN*

3.1 Significance and background

To assess the sensor performance in an implantation environment and to optimize the sensor configurations, it is necessary to evaluate how various tissue, particle, and particle distribution characteristics affect the measurement performance. These aspects include the size and tissue concentration of microparticle sensors, particle implantation depth, and scattering and absorption of light by tissue. Intuitively, one would expect implantation depth to influence the measurability of luminescence, because the attenuation of optical signal is proportional to the path-length of photon propagation. One might also anticipate that tissue scattering and absorption will result in distortion of spectral information from implants, due to the wavelength-dependent nature of tissue optical properties. The size of implants will affect the luminescent intensity, due to changing probability of excitation, whereas the particle concentration may result in different spectral distortions from tissue due to different spacing between particles. Finally, for the design of an efficient system for collection of escaping luminescence, it is also critical to determine the spatial distribution of escaping fluorescence.

Simulations can be of immense value in modeling this situation, allowing insight into the key parameters affecting escaping luminescence and guiding the design process. Monte Carlo modeling has been applied to simulate light propagation in tissues for nearly two decades [49]. The Monte Carlo method was coined by John von Neumann, Stanislaw Ulam and Nicholas Metropolis in 1940s, while they were working on Manhattan project in the Los Alamos National Laboratory [50]. Monte Carlo method uses random sampling to compute the results and it has been used to solve a variety of physical problems. In the application of Monte Carlo method, the

---

*Part of this section is reprinted with permission by R. Long and M. J. McShane, 2010, Journal of Biomedical Optics, 15, 027011, Copyright 2010 SPIE; R. Long, S. Singh, and M. J. McShane, 2008, Proc. SPIE, 686307, Copyright 2008 SPIE (2008).

expected value of a certain random variable in a stochastic model is equivalent to the value of a physical quantity to be determined. This method is most suited to calculation by a computer and tends to be used when it is infeasible to compute an accurate result with a deterministic algorithm [50]. Monte Carlo modeling offers a flexible yet rigorous approach toward photon propagation in turbid tissues. The modeling describes the photon transportation as the probability distributions of step size of photon movement and the angles of deflection [38].

As a computational modeling tool, Monte Carlo modeling can facilitate understanding of light distribution in tissues, as well as validation of analytical models of light transport [51]. A large number of studies have employed Monte Carlo simulations to assess the effect of excitation and emission geometries, sample dimensions, and absorption and scattering coefficients of sample fluorescence [52-60]. Monte Carlo has also been employed to investigate the relationship between the fluorescence originating from different layers within the tissue and the observed bulk tissue fluorescence spectrum [61-64]. A number of groups have employed Monte Carlo code in design of optical diagnostic instrument design. The optical diagnostic methods include laser Doppler flow-metry [65-79], fluorescence spectroscopy [80-86], reflectance spectroscopy [59, 87-90], and so on. For many optical diagnostic instrument designs, the design of fiber-optic probe is of great significance, because it is associated with signal intensity, sensitivity, resolution or signal-to-noise ratio. To design a fiber-optic probe, a lot of Monte Carlo modelings have been carried out to evaluate the effect of parameters of fiber-optic probe and the optical properties of tissue models. The parameters of fiber-optic probe include numerical aperture, diameter, source-detector distance, fiber orientation, shape of the fiber tip, and so on. Keijzer et al's paper [53] might be the first work of using Monte Carlo modeling to simulate fluorescent light propagation in turbid media. Pfefer et al [55, 85, 91] extensively studied the effects of numerical aperture, fiber diameter, source-detector separation, and probe-to-tissue distances on the fluorescence

detection. Qu et al [58, 59] used Monte carlo modelings to determine appropriate excitation-and-collection geometries with which the distortion of fluorescence spetra due to optical properties of tissues could be minimized. Jaillon et al[81] used the Monte Carlo simulation to design a beveled fiber-optic probe for improving the depth-resolved fluorescence measurement. Pogue et al's paper [56] is a typical example of using Monte Carlo code to design a fiber probe for quantitative fluorescence detection that could reduce the effect of intrinsic absorption and scattering in local background. For depth-resolved reflectance spectroscopy, Arifler et al's work [80] demonstrated the use of Monte Carlo code to design a compact fiber-optic probe capable of resolve reflectance spectra from two successive layers of biological tissue. Zhu et al's paper [92] demonstrated the use of Monte Carlo code to design a fiber-optic probe for depth-resolved fluorescence measurement. The time-resolved Monte Carlo code is also a powerful computational tool for studies of time-resolved spectroscopy [93-96].

In previous study, McShane el at introduced the use of Monte Carlo to model the transport of light through human skin and interaction with a subcutaneous (e.g. implanted) fluorescent sensing layer; in this work, a sensitivity study was performed to elucidate the effects of changing of optical properties and tissue and sensing layer characteristics on the escaping fluorescence [20]. While these previous studies have given insight into the key parameters affecting the observation of light produced by luminescent implants, two issues with these previous studies limit their broad applicability: (1) the restriction to flat (slab), uniform (homogeneous in x-y plane) geometries and (2) a single pair of excitation and emission wavelengths. These studies fall short of describing real microparticle-based systems with broadband emission relevant for sensing, and the information obtained is therefore insufficient for the design for an optical system to be employed for in vivo measurement. Instead, the interaction between light and skin as well as implanted microparticle sensors should be more accurately modeled with 3D, multi-

wavelength Monte Carlo simulations. Verkruysse et al's paper [97] analyzed the consequences of assumption of homogeneous model. The authors concluded that homogeneous model tended to attenuated more than the discrete absorber models, which intensified the necessity of using 3D modeling. OptiCAD, a recently-released commercial package allowing Monte Carlo ray tracing, has enabled this 3D modeling work.

In this Chapter, Monte Carlo modeling was applied to predict the characteristics of fluorescence escaping from tissue containing implanted microparticle sensors. The properties of the implanted particles (depth, size, spacing, spectral features) and the light source diameter were varied to determine the effects of these parameters on emitted light. The relative output power, spectral information, and the spatial distribution of escaping fluorescent emission were estimated and compared. The findings from these modeling studies supported the potential of in vivo measurement used implanted microspheres, and facilitated the design of hardware.

3.2 Methods

3.2.1 Software verification

Before using OptiCAD (V10.033) as modeling software, it was verified by analytical modeling method and MCML [98](Mote Carlo Modeling of light transport in multi-layered tissues in standard C). One-dimensional diffusion calculation for fluorescence [99] was carried out with MATLAB as the analytical modeling. A multi-layered tissue model and a fluorescent slab were used in the modeling. In analytical modeling, every model was 1-D, while in OptiCAD all the models were 3-D. The fluorescence escaping from the surface of the tissue model was collected by a photon capture film (Figure 3) in OptiCAD. In Figure 4, the discrete data points were obtained from OptiCAD, and the solid line was obtained from analytical modeling. A 3-D fluorescent slab were Thus, Figure 4 shows that the modeling results obtained from these two

approaches agreed well. Figure 5 shows the modeling results of transmittance after a slab with scatters and absorbers, and the results obtained from OptiCAD and MCML agreed well. According to the verifications with two types of approaches, it was concluded that it is reliable to use OptiCAD for 3-D monte carlo modeling.

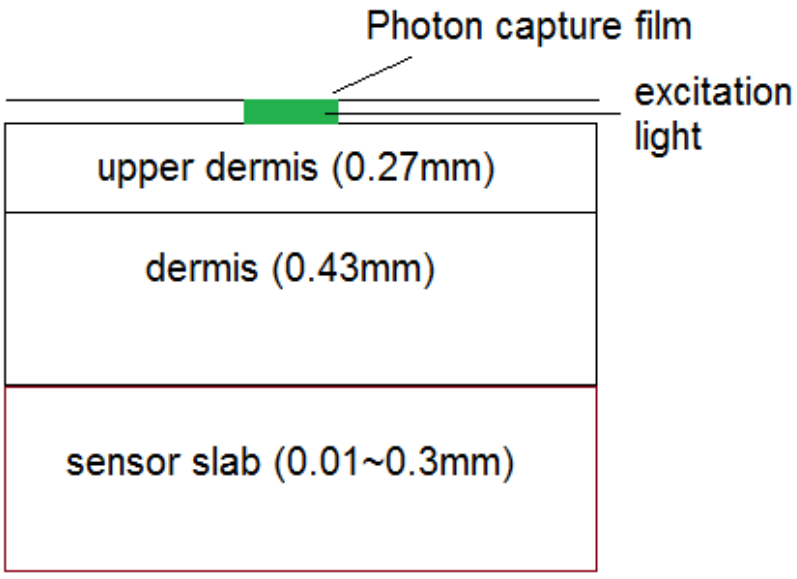

Figure 3. Geometry of the models in analytical modeling and in OptiCAD.

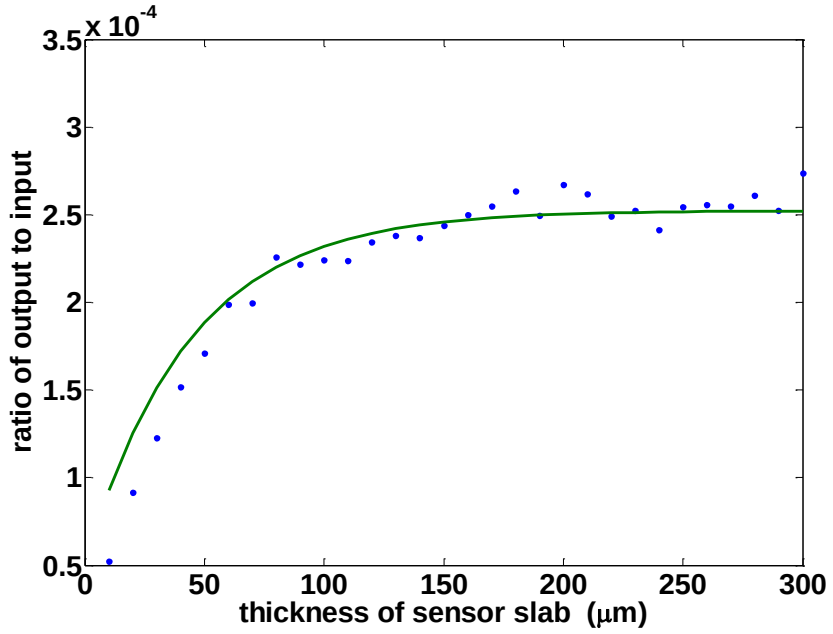

Figure 4. Compare analytical modeling and OptiCAD. Discrete data points were obtained from OptiCAD, and solid line was obtained from analytical modeling.

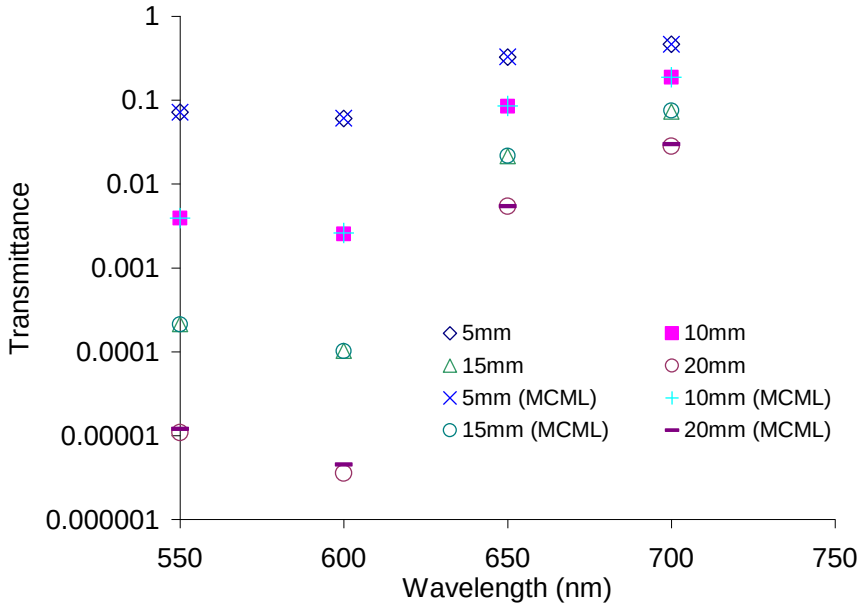

Figure 5. Compare the results obtained from OptiCAD and MCML.

3.2.2 Configuration of modeling system and optical properties

The modeling system was mainly consisted of a four-layered skin model and microsphere model. The four-layered skin model used in simulations was generated from an eight-layered model used by Zeng et al [62] to mimic the anatomical structure and optical properties of skins. The scheme of skin model is shown in Figure 6. The eight-layered model is simplified into a four-layered model comprising one layer above the reticular dermis, a reticular dermis layer, a layer below the reticular dermis, and a subcutaneous fat layer. Stratum corneum (SC) is 10μm, epidermis (ED) is 80μm, papillary dermis (PD) is 100μm, reticular dermis (RD) is 1500μm, dermis is 160μm, upper blood plexus (UBP) is 80μm; lower blood plexus (LBP) is 70μm, and subcutaneous fat is 2mm. In Figure 6, SC+EP+PD+UBP=Upper dermis (270μm), RD = Dermis (1500μm), and LBP+Dermis=Deep Dermis (230μm). Our interest lies in the reticular dermis

(270 μm to 1770 μm), where the microparticle sensors are intended to be introduced and retained in the tissue much like cosmetic dermal-filling agents or tattoos [100], therefore all of the skin layers above or below the reticular dermis were assumed to be homogeneous to simplify the skin models. The four-layer model was designed as a disk of 4-mm height and 30-mm diameter; this radial (lateral) extent of each layer was sufficient to be considered infinitely large compared to the size of the excitation light source and sensor models

.

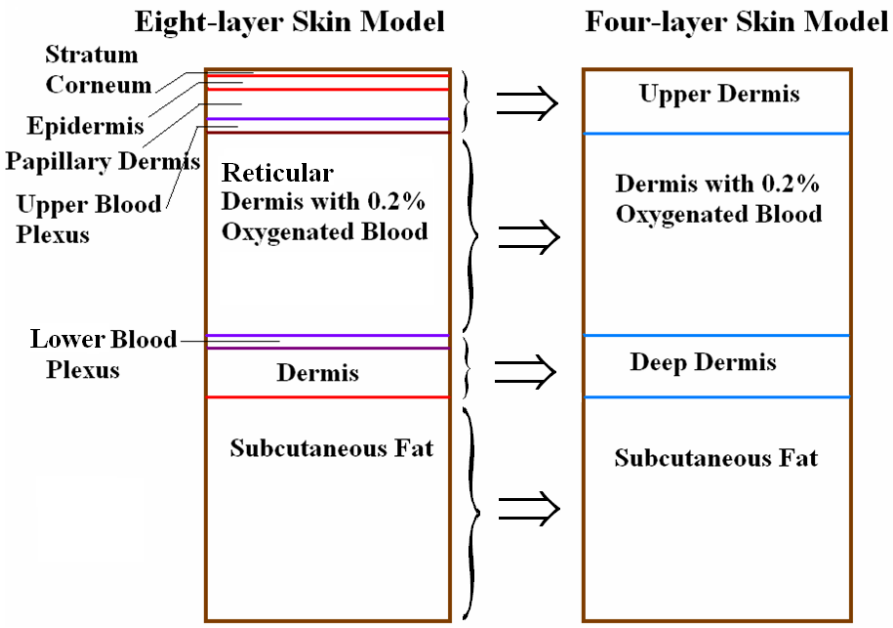

Figure 6. Eight-layer model and four-layer model.

The wavelength-dependent optical properties of the eight-layered model (absorption and scattering coefficients, scattering anisotropy, and refractive index) were extracted from multiple sources based on a review of the literature on tissue optical properties [62, 101, 102]. The optical parameters of the four-layer model were calculated as a weighted average by adding the products of the optical parameters of the eight layer model and the corresponding volume factors according to their volume contributions to each layer of the four-layer model [62, 103]. For example, the calculation for the optical parameters of deep dermis in the four-layer model can be expressed as in Equation (19):

$$\begin{bmatrix} n \\ \mu_a \\ \mu_s \\ g \end{bmatrix} = \begin{bmatrix} n(LBP) & n(Dermis) \\ \mu_a(LBP) & \mu_a(Dermis) \\ \mu_s(LBP) & \mu_s(Dermis) \\ g(LBP) & g(Dermis) \end{bmatrix} \times \begin{bmatrix} \frac{Vol(LBP)}{Vol(Deep\ dermis)} \\ \frac{Vol(Dermis)}{Vol(Deep\ dermis)} \end{bmatrix} \quad (19)$$

The optical properties of skin models and sensor models at each 4of the emission wavelengths (570nm, 585nm, 620nm, 635nm, 645nm and 665nm) were specified (Table 1) to track the emitted luminescent photons.

Table 1 The optical properties for each layer of the four-layer skin model at each of the seven wavelengths used in simulation.

SC+EP+Derm+UBP	wavelength (nm)	n	μ_a (mm^{-1})	μ_s (mm^{-1})	g
	540	1.40	2.53	47.30	0.77
	570	1.40	2.41	45.76	0.77
	585	1.40	1.80	44.73	0.77
	620	1.40	1.35	42.70	0.77
	635	1.40	1.35	42.31	0.77
	645	1.40	1.36	42.02	0.77
	665	1.40	1.39	41.78	0.77
Derm with 0.2% Blood	wavelength (nm)	n	μ_a (mm^{-1})	μ_s (mm^{-1})	g
	540	1.40	0.55	46.01	0.77
	570	1.40	0.54	44.51	0.77
	585	1.40	0.48	43.01	0.77
	620	1.40	0.44	40.42	0.77
	635	1.40	0.43	40.27	0.77
	645	1.40	0.42	40.17	0.77
	665	1.40	0.41	40.02	0.77
LBP+Derm	wavelength (nm)	n	μ_a (mm^{-1})	μ_s (mm^{-1})	g
	540	1.38	9.12	47.10	0.83
	570	1.38	8.57	46.01	0.83
	585	1.38	3.48	44.92	0.83
	620	1.38	0.42	43.03	0.83
	635	1.38	0.40	42.92	0.83
	645	1.38	0.39	42.85	0.83
	665	1.38	0.37	42.74	0.83
Subcutaneous Fat	540 - 665	1.46	-	-	-

The microsphere sensors were assumed to follow the previous work on micro-particle sensor engineering, where the spheres contain platinum octaethylporphine (PtOEP) and rhodamine isothiocyanate (RITC) as indicator and reference dyes, respectively [29, 30]. Briefly, glucose oxidase and PtOEP were immobilized inside of porous microparticles, which were then coated with diffusion-limited nano-films tagged with RITC as reference dye.

The luminescence properties of the microsphere sensors are shown in Figure 7. The emission spectra were obtained in experiments. A green LED was used for excitation and a fiber-optic spectrometer with a bifurcated fiber bundle was used to collect and measure emission. The emission spectrum of microparticles attached to a microscope slide within a flow-through channel was measured during exposure to phosphate buffers containing different glucose concentrations (flow rate: 4 mL/min; oxygen concentration: 277 (μM). Spectra collected at 0, 50, 100, 150, and 250 mg/dL were recorded for use in this theoretical study. The absorption coefficient (11.16 mm^{-1}) was calculated from the molar extinction coefficient of PtOEP at 540 nm, assuming a uniform concentration of 10 nM inside the particles (determined experimentally), while scattering internal to the spheres was neglected [104]. A refractive index of 1.5 was assumed for the particles, based on their silicate nature. As the size of the particles is an experimentally controllable variable that affects sensor response as well as host response, this parameter was also varied in the simulations to reveal the effects of particle size on emission properties.

In this study, the implanted sensors are modeled as “patches” (Figure 8) comprising uniform microspheres positioned within the “dermis” of the four-layer model; the microspheres were assumed to be hexagonally packed into a cylindrical slab. In Figure 8, “D” is the sphere diameter and “S” is the center-to-center spacing. Since the particles could be engineered to have different size, and the in vivo packing density can be varied to a degree by controlling the

injection concentration, the diameters of microspheres and center-to-center spacing for adjacent spheres (Table 2) were varied from 20μm to 100μm to simulate the influence of these parameters on escaping emission signal. The real microparticle sensors have a certain size distribution, but the average size is around 20μm. Any spheres with smaller size may have a bigger possibility to be "eaten" by the cells (Phagocytosis). If the particles are bigger than 100μm, it injection needles might be clogged during injection. Thus, the sphere size was chosen between 20 and 100μm in modeling. The center-to-center spacing was varied to change the packing efficiency to loosely packed (0.5%) to tightly packed (74%). Table 2 shows that the sensor names in the simulations are D100S100, D60S100, D20S100, D60S60, D20S60, and D20S20, where the values following the "D" and "S" correspond to the diameter and the center-to-center spacing between two adjacent spheres for each case given below, respectively. It is noted that, in reality, one has very little control over the final particle distribution in tissue; however, the study was aimed at identifying the potential negative consequences of uneven or inconsistent distribution on collection of emission.

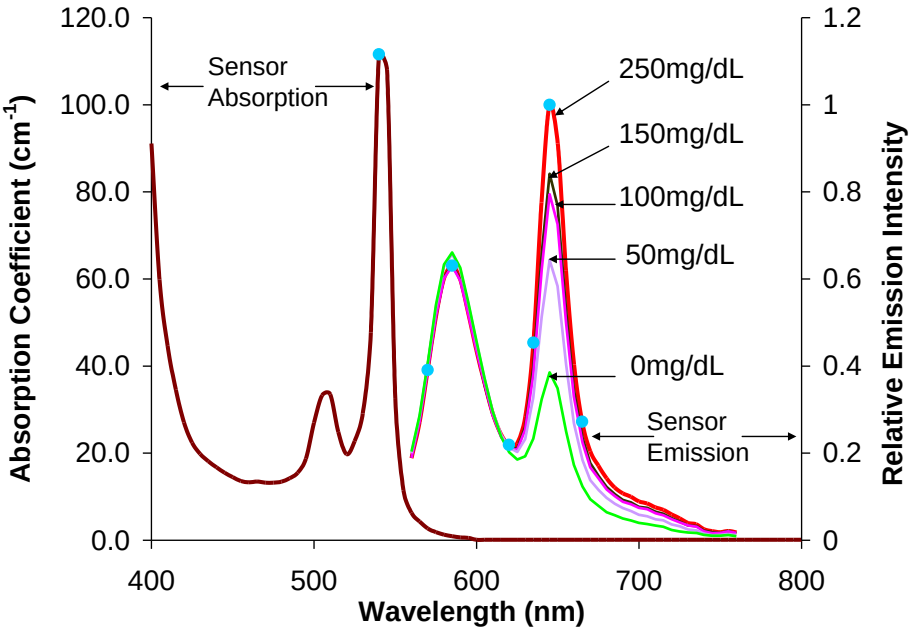

Figure 7. Excitation and emission spectra of sensor particles, as well as spectral properties of a model light source (green filter). For the absorption spectrum shown, [PtOEP] is 10nM. Environmental [glucose] is 250mg/dL. Blue circles and numbers indicate the wavelengths selected for the simulation.

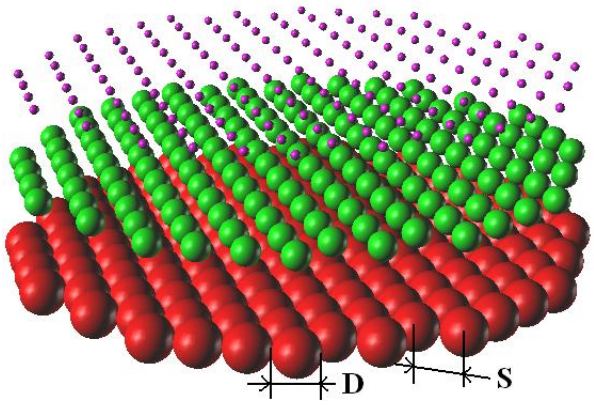

Figure 8. Scheme of the sensor models.

Table 2 Geometric parameters of the six microsphere sensor models used in simulations

D (μm)	S (μm)	Packing efficiency
100	100	74.05%
60	100	15.99%
20	100	0.59%
60	60	74.05%
20	60	2.74%
20	20	74.05%

The scheme of the modeling system is illustrated in Figure 8, including the geometric layout and the excitation source at normal incidence relative to the skin surface. Figure 8 indicates the relative position of excitation light source, implanted fluorescent sensing microparticles, and photon capture film. The long pass filter below the photon capture film is block scattered excitation light. The distance between photon capture film and the surface of skin model is 10μm and that between long pass filter and the surface of skin model is 9.8μm. Though not shown this figure, the lateral extent of the skin model and the photon capture film (30mm) was much larger than the sensor patch size in all cases (1.2-6mm). The models of the microspheres were embedded in the skin model, thus the optical properties of the tissue surrounding and between the microspheres were the same as those of the skin model. Each sphere was modeled as an independent object, and the set of spheres was arranged into a cylindrical array with different packing efficiency.

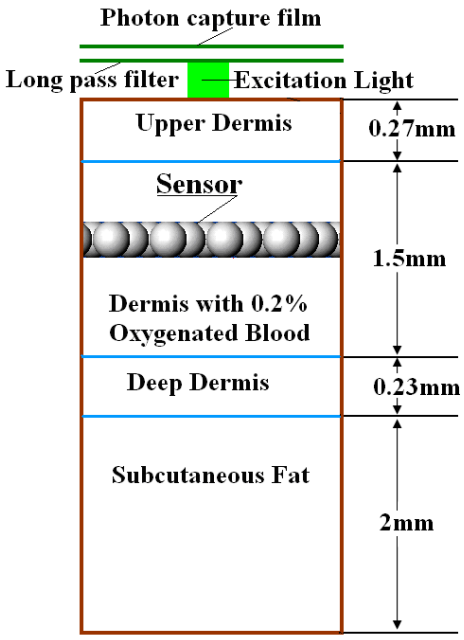

Figure 9. Scheme of simulation system.

To simulate fluorescence emission escaping from the surface of the skin, one excitation wavelength (540nm) and six discrete emission wavelengths (570, 585, 620, 635, 645, and 665nm) were selected from the excitation and emission spectra of sensors to capture the key features (as shown in Figure 7 of the excitation and emission spectra). In the simulations, excitation light underwent absorption and scattering while traveling through the superficial tissue before striking a sphere. Once the excitation photons enter a sphere, fluorescence occurs with isotropic directionality. The fluorescence inside a sphere was generated along each excitation ray according to a randomized distance, sampled from a uniform distribution with an average step size between fluorescence events that was specified as the radius of the sphere. The fluorescent

light emitted by a sphere, once escaped from the sphere, would undergo further absorption and scattering in the skin model. When rays were incident upon an interface between tissue and surface of another sphere, reflection occurred. Since the absorption coefficient of spheres was high, the fluorescence emission from a sphere tended to emit more from the surface than that emitted from the inner space. Moreover, since the excitation light came from the top of the skin model, the emission tended to be emitted more from the sphere surfaces close to the skin surface. The luminescent emission rays propagating through the skin model and finally escaping from the surface of the skin model were collected by a "photon capture film" detector, which recorded the energy and location information of every escaping ray hitting on the film. Below the photon capture film, an ideal long-pass filter was attached to remove all excitation light from the captured rays. The collimated excitation light source was perpendicular to the surface of the skin model and was placed directly below the long-pass filter. The photon capture film and the long-pass filter were placed above the surface of the skin model. The distance between the photon capture film and the surface of the skin model was small enough to ensure the film would capture all the escaping rays. Thus, the photon distribution on the film was an accurate representation of the predicted escaping photon distribution on the surface of the skin model.

3.2.3 Study of excitation fluence distribution in skin

To determine a reasonable dimension for 3D models of skin and microsphere sensors, the depth-dependent spatial distribution of excitation fluence in skin model was investigated. The problem was broken into two parts: (1) Determining the irradiance distribution of a unit excitation light for different depths in tissue; and (2) Determining the circular areas which confine different fractions of unit excitation radiant power at different depths in the skin model. To study these two questions, the skin model was broken up into a series of sections with increasing thickness,

and a photon capture film was positioned at the bottom of every skin model section to capture all the exiting excitation light after undergoing absorption and scattering (Figure 10). The backscattering light reaching each depth from the deeper depth was not simulated in these models, because the excitation light hit the sensors from top to bottom, and the sensors would absorb most excitation light, thus there would be no such amount of backscattered light as that appearing when there were no sensors embedded in the skin model. In this situation, the refractive index of the skin model matched that of ambient to eliminate the total internal reflection. Thirty simulations were performed in triplicate for each of 30 different depths in the skin model, starting at 30μm (close to upper boundary of Upper Dermis) and moving to 2mm (close to the lower boundary of Deep Dermis). In each simulation run, 90000 rays were used. The initial diameter of skin model was 30mm, it would be increased as needed.

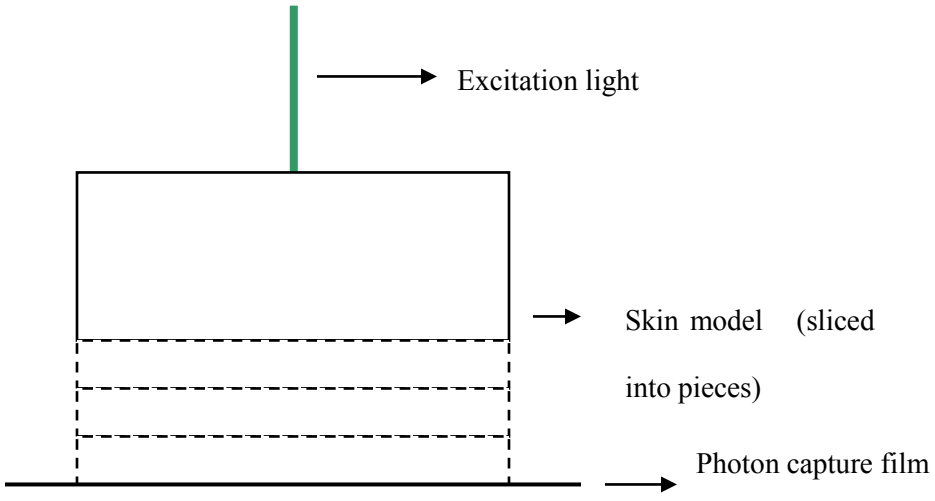

Figure 10. Scheme of the modeling system for investigation of excitation fluence in skin.

3.2.4 Investigation of sensor performance after implantation

To investigate the potential to accurately measure changes in sensor implant spectral properties, the impact of the absorption and scattering of tissue, as well as the microparticle size distribution and concentration for different sensor models with different environmental glucose concentrations were studied. The emission spectra recorded from *in vitro* analysis of sensors at environmental glucose concentrations of 0, 100, and 250mg/mL (Figure 7) were used. Simulations were performed with the six output wavelengths (570, 585, 620, 635, 645 and 665nm) weighted by the relative emission for different glucose concentrations. The ratios of emission intensity (I) of 645nm to that of 585nm were calculated from the output spectra of each sensor emission spectrum corresponding to each glucose concentration using the equation below.

$$R_{645/585}(C,t) = \frac{I_{sen}(645,C,t)}{I_{ref}(585,t)} \tag{20}$$

where $I_{sen}(645, C, t)$ is the emission intensity at 645nm of sensing dyes at the glucose concentration (C), and t is the time; $I_{ref}(585, t)$ is the emission intensity at 585nm of the reference dye, and it is irrelevant to glucose concentrations (C). The percentage change in 645nm/585nm emission peak ratios versus glucose concentration was calculated using the equation below:

$$\%change = \left[\frac{R_{645/585}(C,t) - R_{645/585}(0,t)}{R_{645/585}(0,t_0)}\right] \cdot 100\% \tag{21}$$

where, t_0 is the time when glucose concentration was 0mg/dL.

When glucose concentration was 0mg/mL, the 645nm/585nm emission peak ratio was defined as the baseline value. The percentage changes of peak ratios were plotted as a sensor response curve. Response curves for six different sensor models were compared. The diameter of the spheres was set to 100, 60, and 20μm, and the center-to-center spacing was set to 100, 60, and 20μm. The packing configuration of the sensor patch model was maintained at hexagonal

packing and the total number of spheres was constant, as this would best represent the situation of injecting a fixed number of particles with different final distributions. All the sensor models used in this group simulation were one-layer versions, fixed at an implantation depth of 700μm. The light source was the 100μm×100μm square. There were two groups of simulations. In group A, the absorption coefficient (μ_a) of the microsphere sensors was scaled according to the volume of the spheres in order to make the product of μ_a and the volume of each sphere constant. In group B, the simulations for different glucose concentrations were repeated with a constant absorption coefficient (11.16 mm^{-1} @540nm) for all models. The simulation details were given in Table 3.

Table 3. Models used in assessing effects of sensor configuration on tracking changes in emission.

Sphere Diameter (D) (μm)	Spacing (S) (μm)	Sphere number per layer	Sensor model diameter (mm)	Absorption Coefficient@540nm (mm^{-1})		Light source	Number of Rays	Repetitions
				Group A	Group B			
100	100	1459	4	11.16	11.16	100μm × 100μm square	1.0E+04	5
60	100	1459	4	51.67			1.0E+04	5
20	100	1459	4	1395			1.6E+05	5
60	60	1459	2.4	51.67			1.0E+04	5
20	60	1460	2.4	1395			9.0E+04	3
20	20	1462	0.8	1395			4.0E+04	3

3.2.5 Investigation of measurability versus implant depths

To implement *in vivo* measurement, it is possible that the implantation depths will be difficult to control with high precision; it is likely that particles will be distributed over different depths in the tissue. Thus, an assessment of measurability versus implantation depth is essential to

understand the potential quantitative impact of this practical issue on emission. For these simulations, a single layer of tight-packed sensors 100μm in diameter with 100μm center-to-center spacing ("D100S100") was used. According to the assessment of spatial distribution of excitation fluence in skin model, the sensor patch was set to be 6mm in diameter (3260 spheres) to ensure the sensor patch size is much larger than that of the unit input light source (100μm× 100μm square). This was verified as described in Section 2.4.1. The absorption coefficient at 540nm of microparticle sensors was kept at 11.16mm^{-1}. The depth of the sensor patch was varied from 400 to 1700μm, values representative of typical values for the upper and lower boundaries of the dermis layer. Fourteen simulations were performed for each of 14 depths over this range, and each simulation was repeated 3 times.

3.2.6 Prediction of spatial distribution of escaping luminescence

To design a highly efficient matched optical system for excitation delivery and emission collection, it is necessary to investigate the spatial distribution of the output signal. Using the simulation results for depth-dependent simulations with the 100μm×100μm unit light source in the previous section, 2D convolutions were performed to estimate responses to a large flat circular light source with the diameter ranging from 1mm to 10mm. Because the excitation light source needed a certain dimension in this CAD environment, and could not be simulated as an infinitely-small pencil beam in OptiCAD, the 1-D convolution method [105], which was mostly used in simulations for a finite incident photon beam, could not be applied in our simulations. Therefore, 2-D convolution, which is able to convolve a 2-D response, was performed with MATLAB to predict the spatial distribution of escaping luminescence responsing to incident excitation light sources with different sizes.

3.2.7 Assessment of absolute luminescence response

To maximize the luminescence output and minimize the number of microparticles and amount of dye for *in vivo* implantation, it is critical to assess the fluorescent output for different sensor configurations and dye distributions. This task can be broken into three parts: (1) Investigating the impact of changes in sphere packing efficiency; (2) Assessing the impact on output due to the changes of dye concentration per sphere and effective dye concentration, given the same total quantity of dye; (3) Assessing the effects of having more particles in a stacked (layered) structure. The simulation details are summarized in Table 4.

For Step 1, the impact of sphere packing efficiency was investigated by varying center-to-center spacing with a constant sphere size. Simulations were completed for three different one-layer sensor models with a sphere size of 20μm diameter, where center-to-center spacing was varied from 20μm to 100μm (D20S100, D20S60, D20S20). In these simulations, the absorption coefficient of microparticle sensor models was fixed; thus, the effective dye concentration (the product of dye concentration per sphere and sphere packing efficiency (Table 2)) decreased with decreasing sphere packing efficiency (increasing spacing). The maximum diameter of the sensor patches was 1.2mm, and the light source was a 2.4mm diameter uniform flat circular incident beam, ensuring all the sensor particles could be excited by excitation light.

For Step 2, the impact of dye concentration was assessed with all six sensor models (D100S100, D60S100, D20S100, D60S60, D20S60 and D20S20). The size of sensor patch models and the light source size were the same as those used in Step 1. The absorption coefficients of microparticle sensor models were scaled according to the volume of each sphere and particle numbers so as to make the product of the absorption coefficients, the volume per sphere and the particle number constant. Thus, each sensor model had the same quantity of dye

and the sensor models with the same center-to-center spacing have the same effective dye concentration.

For Step 3, effects of having more particles in a stacked (layered) structure were assessed with three different multilayer sensor models (D100S100, D60S100 and D20S100). In these simulations, all of the sensor patch models were 4mm in diameter and a unit input light source (100μm×100μm square) was used. The number of stacked layers of sensors was varied from one to three, and the absorption coefficients of microparticle sensor models were again scaled according to the volume per sphere. Thus, the product of absorption coefficients and sphere volume was constant, and the effective dye concentration in the tissue was constant for different sensor models.

Table 4. Overview of simulations used to investigate sensor size/spacing/layer effects. Note: All of the sensor models in this series of simulations were located at the same depth (700μm).

	Step 1			Step 2						Step 3		
Sensor Model	D20S100	D20S60	D20S20	D100S100	D60S100	D20S100	D60S60	D20S60	D20S20	D100S100	D60S100	D20S100
Sphere Diameter (D) (μm)	20	20	20	100	60	20	60	20	20	100	60	20
Sphere Packing Efficiency	**0.59%**	**2.74%**	**74.05%**	74.05%	15.99%	0.59%	74.05%	2.74%	74.05%	74.05%	15.99%	0.59%
Center-to-center spacing (S) (μm)	100	60	20	100	100	100	60	60	20	100	100	100
Number of spheres/layer	151	367	3259	151	151	151	367	367	3259	1459	1459	1459
Light source	2.4mm diameter circular irradiance: 1mW/mm^2			2.4mm diameter circular irradiance: 1mW/mm^2						100μm x 100μm square irradiance: 1mW/mm2		
Sensor model diameter (mm)	1.2			1.2						4		
Number of sensor model layers	1			1						1 2 3		
Absorption Coefficient@540 nm (mm^{-1})	11.16	11.16	11.16	1.93	8.92	240.86	3.67	99.10	11.16	11.16	51.67	1395.00
Dye concentration per sphere (nM)	**10.00**	**10.00**	**10.00**	1.73	7.99	215.83	3.29	88.80	10.00	10.00	46.30	1250.00
Effective dye concentration (nM)	0.06	0.27	7.40	1.28	1.28	1.28	2.44	2.44	7.40	**7.40**	**7.40**	**7.40**
Total amount of dye (mol)	6.33E-18	1.54E-17	1.37E-16	**1.37E-16**	**1.37E-16**	**1.37E-16**	**1.37E-16**	**1.37E-16**	**1.37E-16**	7.64E-15 1.53E-14 2.29E-14	7.64E-15 1.53E-14 2.29E-14	7.64E-15 1.53E-14 2.29E-14
Number of Rays	4.0E+06	2.1E+06	2.3E+05	2.3E+05	6.4E+05	4.0E+06	2.3E+05	2.1E+06	2.3E+05	1.0E+04	1.0E+04	1.6E+05
Repetitions	3			3						3		

3.3 Results and discussions

3.3.1 Excitation fluence distribution in skin

Figure 11 is a plot of the predicted spatial distribution of the relative fluence of excitation light (relative fluence of excitation light that was normalized with incident light) in the skin model. The lateral diameter of skin model was 30mm and the diameter of excitation light source was 100μm. The key point from this graph was that the beam spreads to cover a maximum cross section of a few millimeters, such that the sensor patch with 6mm diameter should be sufficient to ensure that the excitation beam did not exceed the path dimensions. As the light penetrated the tissue, the excitation intensity decreased from 10^{-2} to 10^{-8} from the upper boundary to the lower boundary of dermis layer, with an exponential decay following the expected profile. This is more clearly revealed in Figure 12, which is a plot of relative power of excitation light versus depth. In each layer of skin model, the relative power plotted in log-scale decreased linearly with depth.

Figure 13 is a plot of the radii for different fraction of total power at different depths, which is useful in understanding the lateral spreading of the light relative to the incident beam and sensor implant. The 99.9% beam radii range from 0.71 to 2.44mm at the upper boundary and lower boundary of dermis, respectively, indicating that cylindrical models centered at the origin with diameter greater than 4.88mm can be considered as infinitely large compared with the size of unit light source. To ensure that the skin model and sensor models are infinitely large, 30mm diameter skin model and 6mm diameter sensor patch are sufficient for light source size of 100μm.

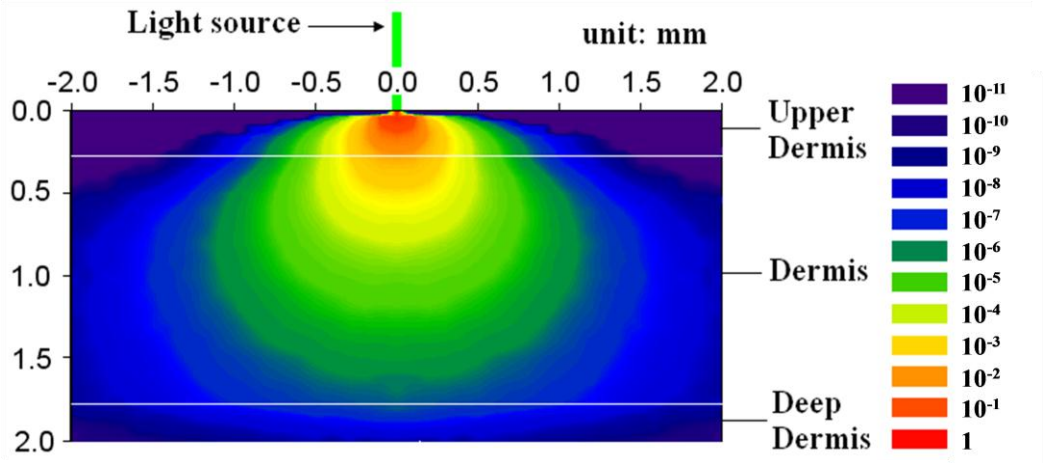

Figure 11. Spatial distribution of relative irradiance (intensity) of excitation light in skin model. The color bar indicates the relative the relative intensity from 1 to 10^{-11}. The green line at the origin indicates the green color of the light source. The light source is a uniform-intensity circle with diameter of 100µm. The thickness values for Upper Dermis, Dermis and Deep Dermis were 270µm, 1500µm, 230µm, respectively

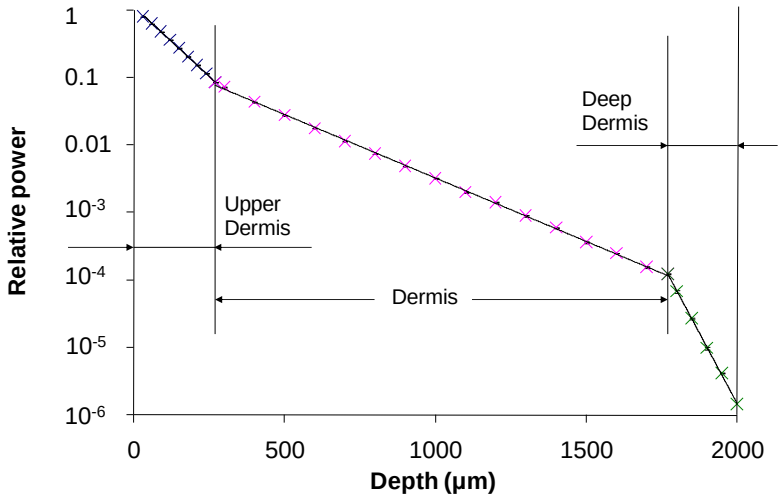

Figure 12. Simulation output for relative power of excitation light versus depth. Error bars (3 runs @ 10,000 rays) were too small to be observed on a plot.

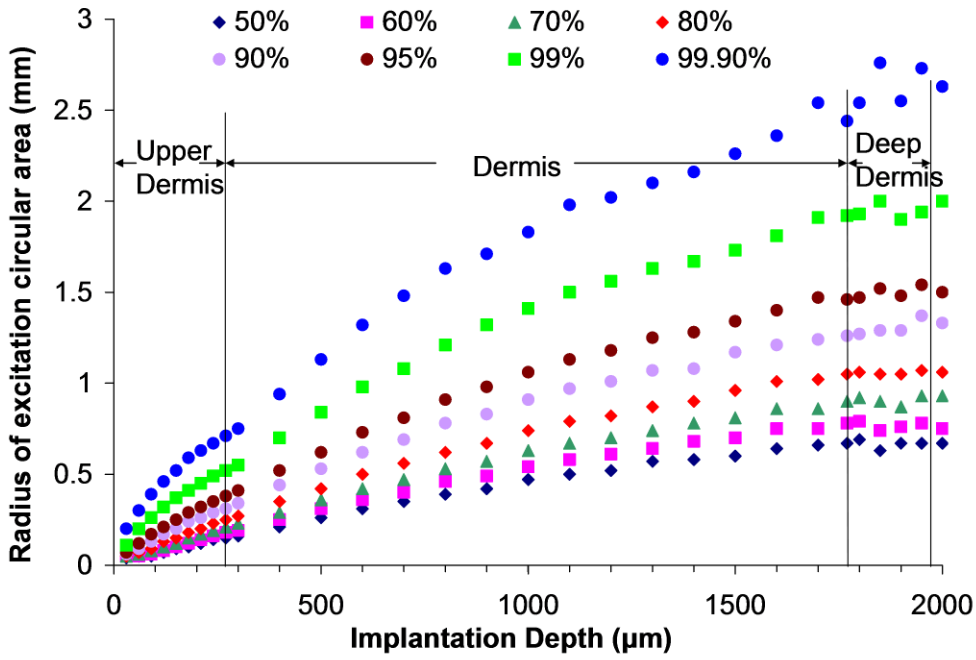

Figure 13. Radius of excitation areas with different fraction of total excitation power versus depth. The light source considered in theses case was a circle with diameter of 100μm.

3.3.2 Sensor performance after implantation

The simulated peak intensity ratios (645/585nm) versus glucose concentration were compared with those obtained from experiments in a flow-through system simulations. The predicted peak ratio values were significantly higher than the *in vitro* measured values, due to spectral distortion introduced from absorption and scattering of tissue and sensors; specifically, the shorter wavelengths are attenuated more than the longer wavelengths. Figure 14 (a) and (b) showed the simulated peak ratios of 645nm to 585nm emission when the absorption coefficient (μ_a) of the microsphere sensors was scaled according to the volume of the spheres in order to make the product of μ_a and the volume of each sphere constant (group A in Table 3). Figure 14(a) and (b)

showed the simulated peak ratios of 645nm to 585nm emission when absorption coefficient was kept as an constant at 11.16 mm^{-1} @540nm for all sensor models (group B in Table 3).

However, when considering the need to measure changes in emission and correlate those with biochemical changes in the sensor environment, it is the percentage change in the peak ratio with analyte concentration that is most relevant. The percentage change of peak ratios was calculated as in Equation (25). The simulated percentage changes of peak ratios were shown in Figure 15 and 16. Figure 15 (a) and (b) were the results of simulations of group A (Table 3), and Figure 16 (a) and (b) were the results of group B(Table 3). From Figure 15 and 16, it is clear that all the data fall around the same *in vitro* curve. Figure 15(b) and Figure 16(b) are a statistical analysis of Figure 15(a) and Figure 16(a), where each of the 95% confidence intervals include the corresponding calibration curve (*in vitro* curve) value, with the single exception of the small spheres with small spacing (tight packing, D20S20) at 250 mg/dL. This proves that the changes in emission will be essentially identical to those observed *in vitro*, enabling direct application of *in vitro* calibration with single-point correction, without additional significant effects from apparently strong spectral distortions. The single case of statistically different output indicates that the spectral distortion introduced by the tissue will require a new calibration model to be established for *in vivo* analysis.

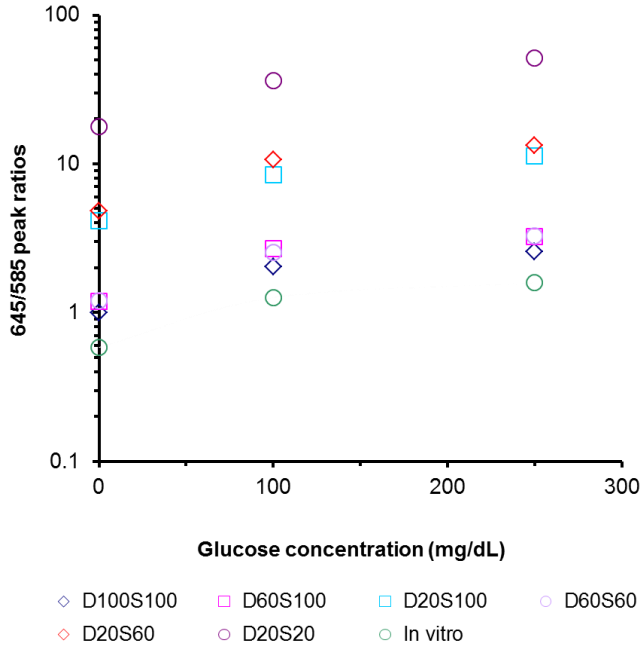

(a)

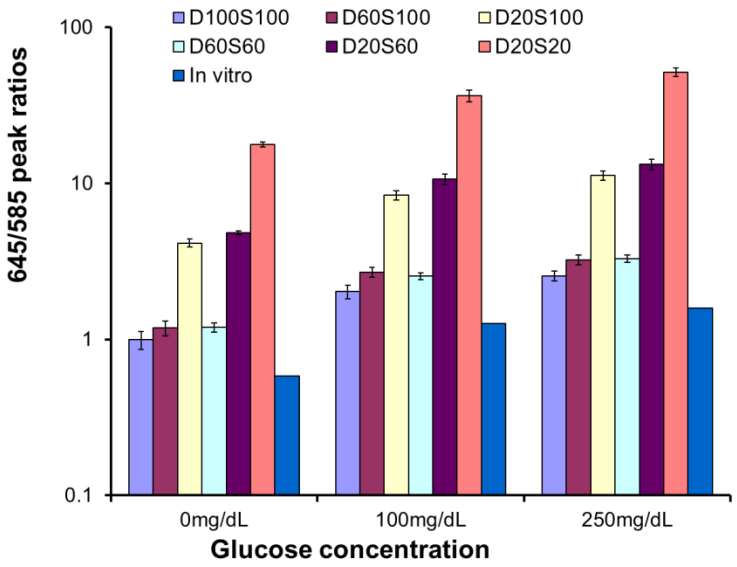

(b)

Figure 14. (a) Peak ratios of 645nm to 585nm emission when the absorption coefficient of sensors was scaled (simulation group A in Table 3). (b) statistical analysis of the peak ratios. Error bars are 95% confidence interval.

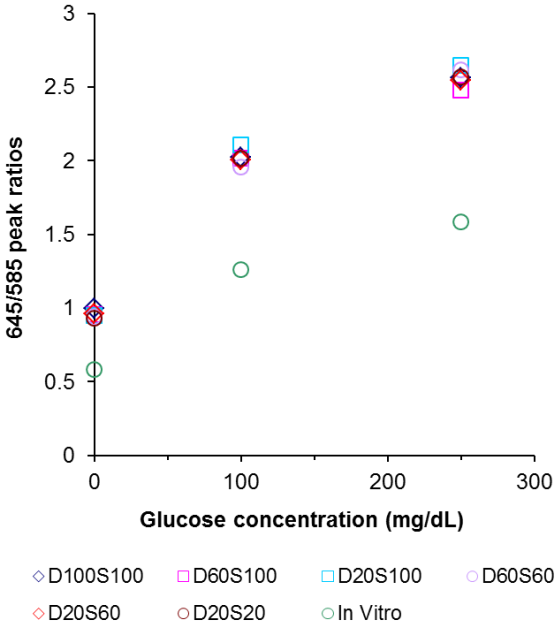

(a)

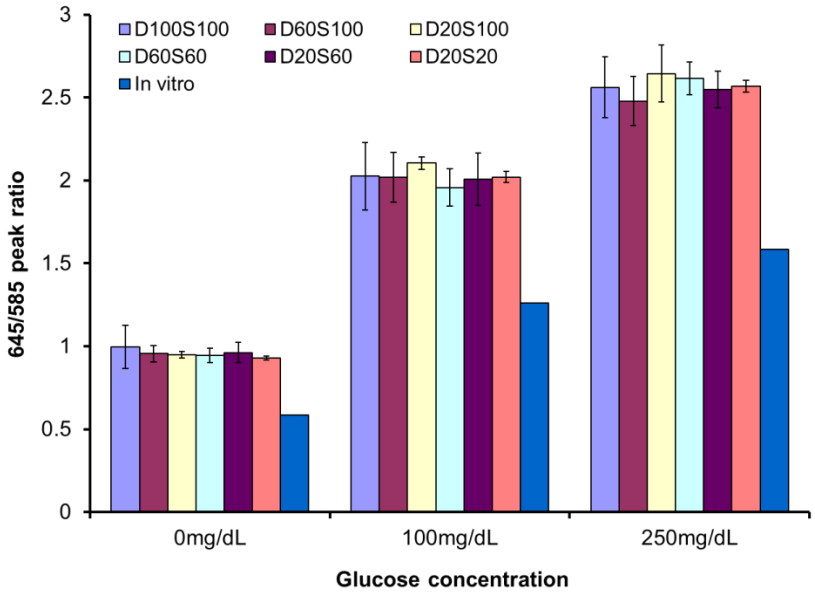

(b)

Figure 15. (a) Peak ratios of 645nm to 585nm emission when the absorption coefficient of sensors was constant (simulation group B in Table 3). (b) statistical analysis of the peak ratios. Error bars are 95% confidence interval.

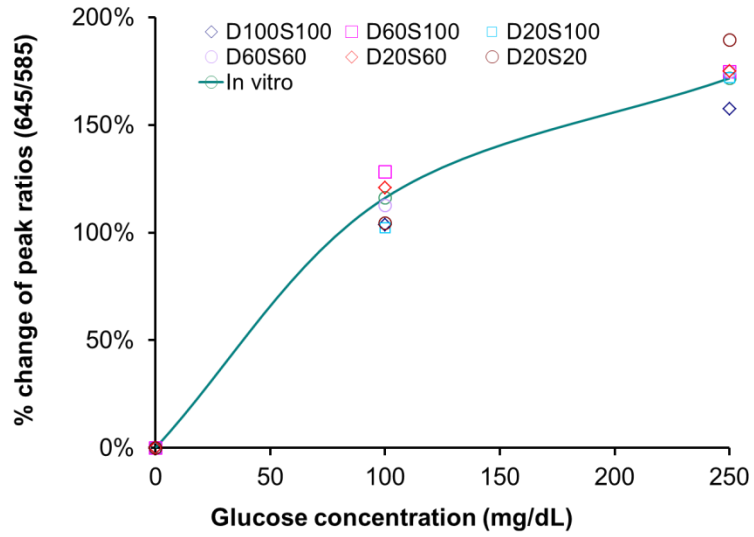

(a)

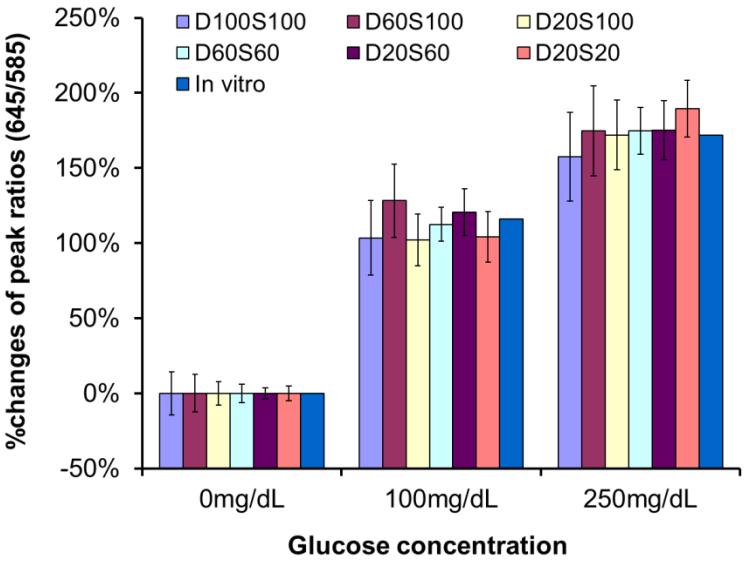

(b)

Figure 16. (a) Percentage changes of peak ratios (645/585) when the absorption coefficient of sensors was scaled (group A in Table 3). (b) statistical analysis of (a). Error bars are 95% confidence interval.

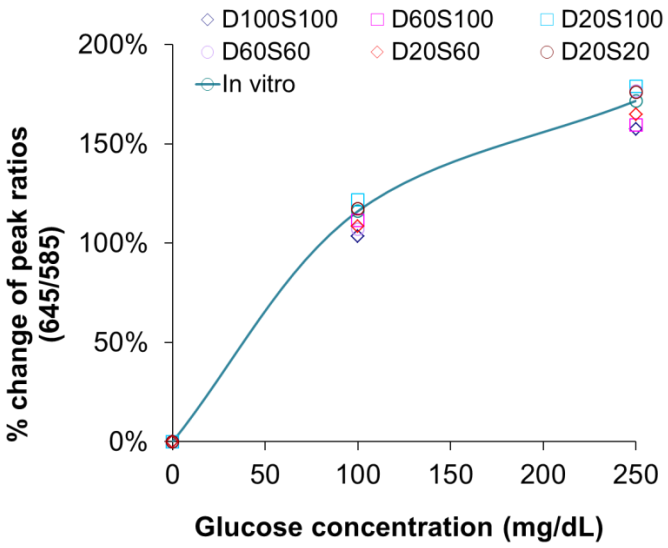

(a)

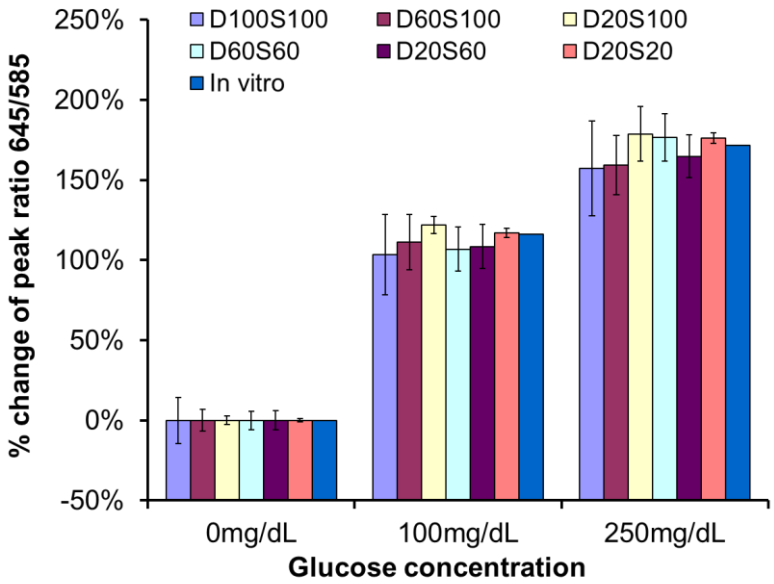

(b)

Figure 17. (a) Percentage changes of peak ratios (645/585) when the absorption coefficient of sensors was constant (group B in Table 3). (b) statistical analysis of (a). Error bars are 95% confidence invertal.

3.3.3 Effects of varying implantation depths

The predicted emission spectrum from implanted sensors versus the implantation depths is given in Figure 18. As shown in this graph, the relative intensity decreases as the implants are located deeper in tissue. The ratio of total escaping fluorescence power to that of the total excitation power is also shown in Figure 19 [106], from which it can be observed that the ratio of output power (fluorescence emission light escaping from the skin surface) to the input excitation power ranges from 10^{-3} to 10^{-6} for sensors at the upper and lower boundaries of the dermis (400μm and 1700μm from the skin surface, respectively). Therefore, the efficiency of fluorescence ranges from approximately one photon per 1000 input photons to one photon per 1,000,000 input photons. On a practical level, this means that a 1mW excitation light source with 1mW/mm^2 input intensity the expected minimal output intensity is 1nW. Thus, the output should be detectable using common detectors such as avalanche photodiodes or photomultiplier tubes, regardless of implant depth. It is noteworthy that the maximum permissible exposure (MPE) for human skin is given as 2mW/mm^2 [107], and therefore these numbers are realistically achievable.

The peak ratios values for the emission (645/ 585nm) versus implantation depth are given in Figure 20. In this graph, the peak ratios increases slightly as the sensor goes deeper, this is mainly because the shorter wavelength is absorbed more than longer wavelength since 585nm is close to one of the absorption peaks of hemoglobin. This observation has two important implications for our work. First, the peak ratio is not very strongly dependent on depth, such that implants residing between 500 and 1000mm depths are expected to have the same output signal.

Second, the peak ratio does significantly increase relative to the value expected without tissue, indicating that the measurements could be susceptible to fluctuations in optical properties of tissue superficial to and in between sensor particles. For example, changes in hemoglobin saturation will alter the absorption of light emitted by sensors at 585nm, which would subsequently change the corresponding measured intensity ratio. It is worth mentioning that these sensors could monitored with luminescence lifetime analysis, which would rely on the emission from the longer-wavelength oxygen-sensitive porphyrin (645nm for PtOEP, or 700nm if the palladium version of the same molecule is used); in this case, varying attenuation due to tissue would have even less influence on measured signals due to the longer wavelength and the inherently robust nature of lifetime analysis. Thorough consideration of factors such as skin color, dynamic chromophore concentration changes, oxygenation shifts, and scattering increases due to formation of a fibrous collagen capsule around the implants will be given in future studies; however, the focus of this work is on studying the effects of sensor configurations, implant depths, and excitation beam characteristics on the spatial and spectral distribution of escaping light.

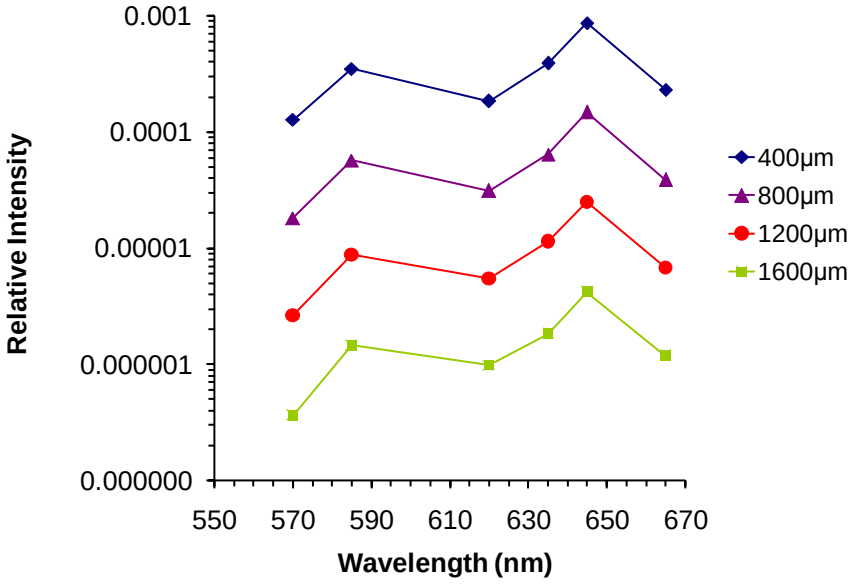

Figure 18. Spectrum of escaping fluorescence relative input light at different sensor implantation depth. The log scale intensity axis highlights the exponential depth dependence. The sensor configuration was a single layer of tight-packed particles 100µm in diameter with 100 µm center-to-center spacing ("D100S100").

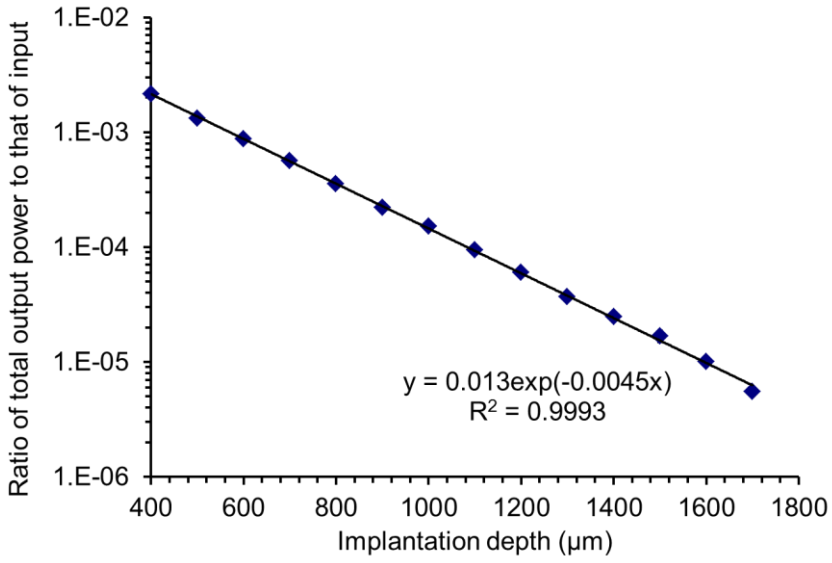

Figure 19. Ratio of total escaping fluorescence power to the total input excitation power versus depth. Inset is log-scale plot. The environmental glucose concentration used for emission spectra was 250mg/dL (the spectra obtained from prototype sensors exposed to 250mg/dL *in vitro* were used). The absorption coefficient (@540nm) was kept at 11.16 mm^{-1}.

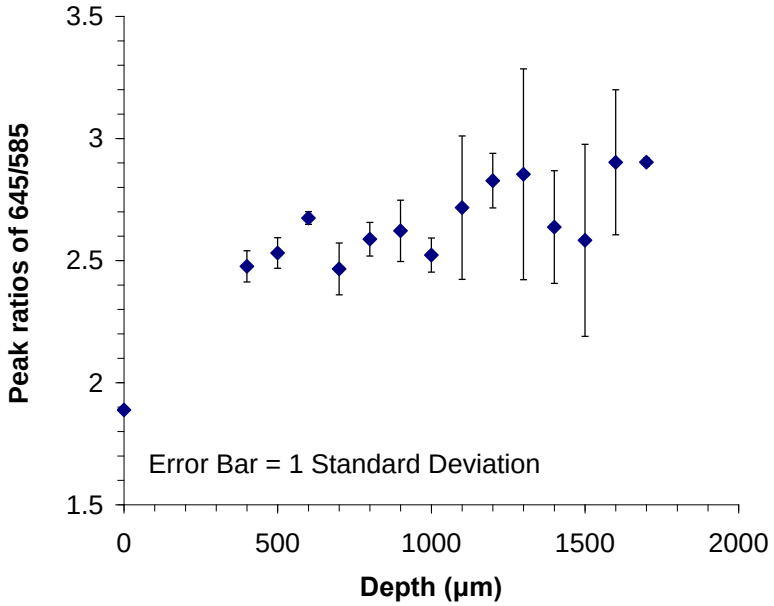

Figure 20. Peak ratios of emission at 645nm to that at 585nm versus implantation depths

3.3.4 Spatial distribution of escaping luminescence

Figure 21 is a plot of the spatial distribution of relative integrated escaping power versus distance from the center of the light source. As shown, the integrated output power increases quickly with distance, which illustrates that the emission output power drops rapidly with distance from the light source center (origin). However, for the 1mm radius light source, the scattering of light in the tissue results in continuing increases in emission beyond the edges of the input beam. The escaping photons become more broadly distributed as the implantation depth increases. In all cases, at least 50% of the total integrated output power is confined within a circular area with 2 mm radius. When the goal is to capture 90% of the output light, the required capture radius increases to 1.5-5.0 mm, depending upon the implant depth. Similarly, a capture radius of 1.75 to 6.9mm will be required to confine 95% of total signal power.

Figure 22 contains a surface plot, where the surface height represents the radius for a circular area that confines 95% of total escaping fluorescence power collected on the photon capture film. The surfaces were computed for different implant depths as well as different light source diameters. It can be seen that, even for a light source with 10mm diameter and sensors implanted close to the lower boundary of dermis, a circular area with a radius of 9mm was able to confine 95% of total output power. Thus, in general, deeper implants require larger field of view for collection optics to avoid throwing away photons, but efficient collection of output for dermal implants can still be achieved with relatively small-area optics; a standard 1-inch optical system will be sufficient.

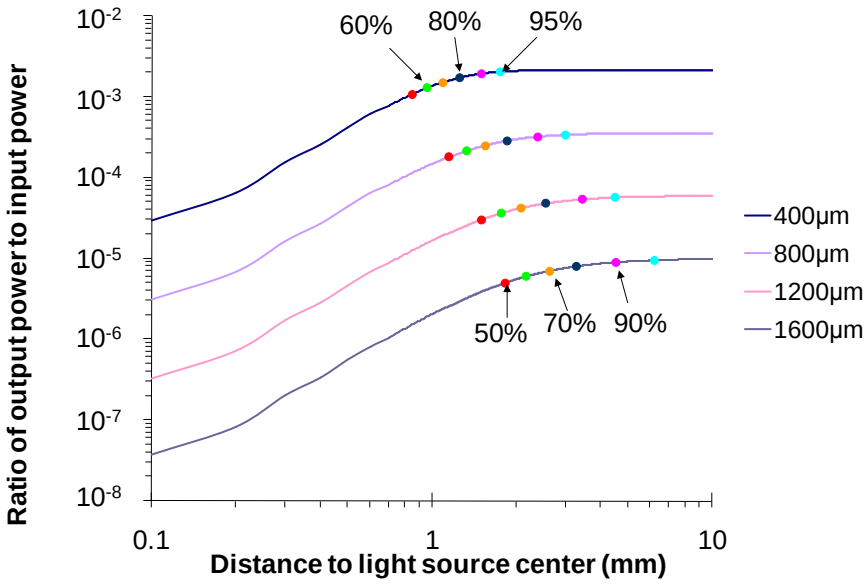

Figure 21. Spatial distribution of integrated power versus implantation depths. (Excitation light source size = 2mm in diameter). The discrete color data points of different colors represent different fraction of total escaping fluorescent power when the sensor was positioned at a certain depths.

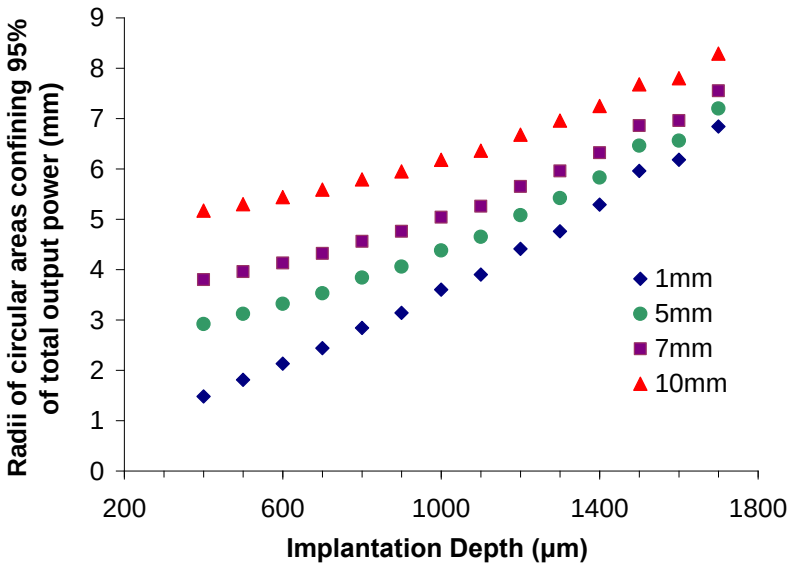

Figure 22. Radii of circular area confining different fraction of total escaping fluorescence power versus implantation depths and size of excitation light source.

Since the angle of escape and numerical aperture of the optics involved will also determine the efficiency of collection, I also investigated the angular distribution of escaping fluorescence versus different implantation depths (data not shown). The angle of escape was found to decrease linearly with cos(θ) (matches Lambert's cosine law), and therefore high-numerical aperture optics are desirable for capturing emission. There was no significant effect of implant depth on angular distribution (p-value = 1.0, α=0.05, paired t-test). Thus, the spatial distribution of escaping fluorescence is the most critical factor of optical system design.

3.3.5 Absolute luminescence response

Figure 23 contains a plot representing the results of Step 1 (Table 4) simulations used to investigate the impact of sphere packing efficiency of sensor models (see Table 3). In these

simulations, the dye concentration per sphere was kept constant (bold numbers in the column of Step 1 in Table 4), meaning that the effective concentration of dye in the tissue decreased with lower packing efficiency. Intuitively, one would expect the fluorescence output per sphere would be reduced by less sphere packing efficiency because of relatively more absorption induced by tissue; however, it is evident from these results that the output per sphere for the D20S20 sensor model is smaller than those of D20S60 and D20S100, even though the total output of D20S20 is the largest. This is attributed to a higher probability of interaction between laterally scattered excitation light and particles in loosely-packed (center-to-center distance = 60 or 100μm) sensor models or the lower probability of re-absorption by loosely-packed spheres. Accordingly, the D20S60 and D20S100 sensor models will have more output than that of D20S20, if the three sensor models have the same number of spheres and the light source is large enough to ensure all the spheres are uniformly excited. Thus, if a large enough light source is used to uniformly excite all the particles regardless the particle spatial distribution, a lower sphere packing efficiency will not reduce the total fluorescence output.

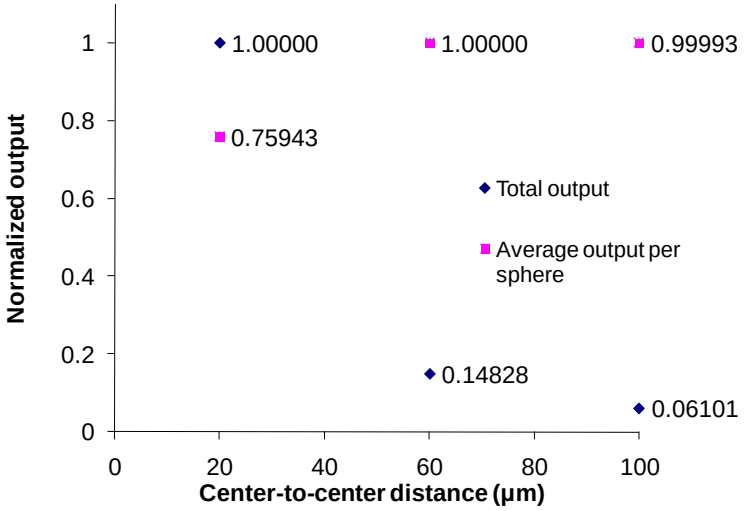

Figure 23. Normalized output for sensor models with different packing efficiency, including total output from each sensor-patch model, and average emission per sphere in each sensor-patch model.

In reality, implementation of *in vivo* injections will result in difficulty of controlling the implantation area with high precision; it is also likely that particles will be distributed with different projection areas in the tissue, thus a sufficiently large light source with constant irradiance is preferred to avoid reducing fluorescence output due to the unpredicted projection area change of injected sensors in tissue.

Figure 24 contains the results of Step 2 (Table 4), where six different sensor models were used to assess how different dye concentration per sphere and effective tissue dye concentration affect the escaping fluorescence, given the same quantity of dye (see bold numbers in the column of Step 1 in Table 4). As shown in this graph, though every sensor model had the same total amount of dye in the entire patch of particles, the output is dramatically different. The output from tightly-packed models (D100S100, D60S60, and D20S20) was higher than that from loosely-packed versions. The D20S100 has the smallest output, though the dye concentration

per sphere of D100S100 is the smallest and that of D20S100 is the highest. According to the simulation results, the tightly-packed sensors produce stronger signals than loosely-packing sensors, even when the amount of dye in the sensor patch remains constant. The average output per sphere of loosely-packed spheres (empty symbols) were higher than that of tightly-packed models, which again proved that the loosely-packed sphere models have a lower inner filter effect than the tighter-packed versions. Since these sensor models had the same amount of dye, the ones cases having the same effective dye concentration should produce the same amount of luminescence emission as if the sensor was a homogeneous model. Though the effective dye concentration of "D100S100", "D60S100" and "D20S100" were all 1.28nM, the estimates for total output power of these models were not the same. Neither were the outputs of "D60S60" and "D20S60,"which also had the same concentration. This highlights the inadequacy of a homogeneous model, a fact that was previously discussed in the context of discrete absorbers for accurate representations [97].

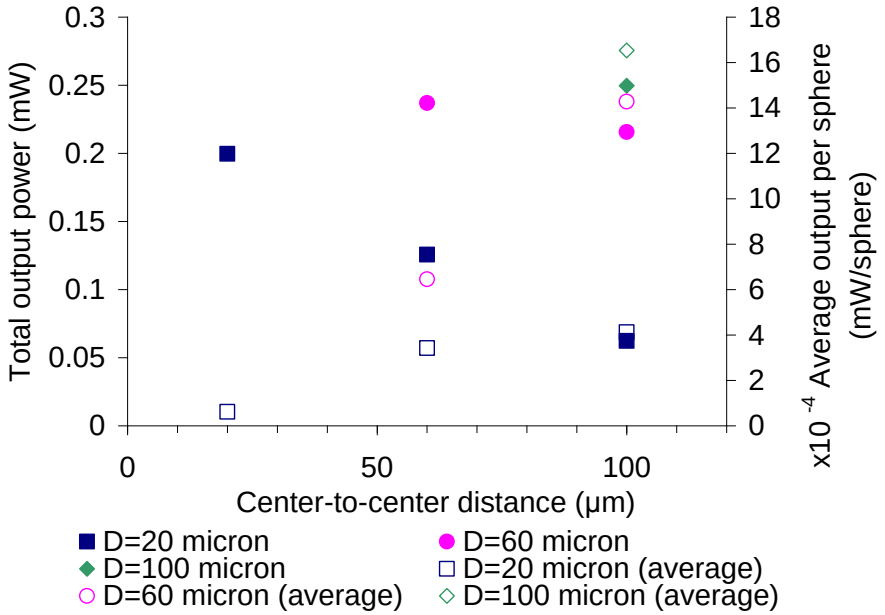

Figure 24. Relative output for different sensor models. All the sensor patches were 1.2 mm in diameter, and the uniform light source was 2.4 mm in diameter with intensity of 1 mW/mm2. The absorption coefficients of D100S100, D60S100, D20S100, D60S60, D20S60, and D20S20 were 1.93 mm^{-1}, 8.92 mm^{-1}, 240.86mm^{-1}, 3.67 mm^{-1}, 99.10 mm^{-1}, and 11.16 mm^{-1}, respectively.

Figure 25 contains the results of simulations for Step 3 (Table 4), designed to assess the effects of multiple layers of microparticles (see Table 2). One to three layers of D100S100, D20S100 and D20S100 sensor models were used, and all the sensor models have the same effective dye concentration (Table 4). The output of 2-layer D100S100 and 3-layer D100S100 are 20.3% and 20.9% higher than that of 1-layer D100S100, respectively. The output of 2-layer D20S100 and 3-layer D20S100 are 47.5% and 75.5% higher than that of 1-layer D20S100. Interestingly, while adding more layers to tightly-packed sensor models does not increase fluorescence output as much as loose-packing sensor models, the output of just one layer of tight-packed particles is still higher than that of several layers of loosely-packed sensors. Thus,

the tighter the particles are packed, the less sensitive to changing number of layers and the higher the output power.

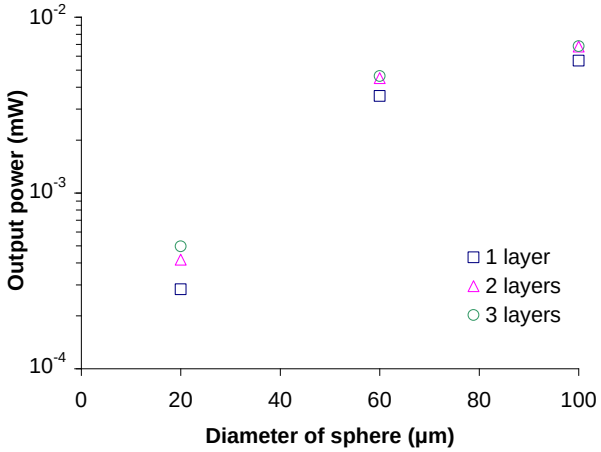

Figure 25. Output for different sensor models with different numbers of layers. Light source is 100 m100 m square with intensity 1mW/mm^2. The absorption coefficients of D100S100, D60S100, and D20S100 were 11.16 mm^{-1}, 51.67 mm^{-1}, and 1395 mm^{-1}, respectively. Models with the same number of layers had the same number of particles.

In summary of this phase of the work, the simulation results corroborate our experimental efforts in highlighting that tight packing is preferred for maximal signals. That is, when the total quantity of dye is limited, if concentration per sphere is already maximized and given a fixed light source size, the sensors with high packing efficiency is always preferred, because sensors with high packing efficiency can yield higher output with fewer particles compared with sensors with smaller packing efficiency.

3.4 Conclusions

Three-dimensional, multi-wavelength simulations of light interaction with tissue and luminescent materials have enabled us to gain insight into the expected behavior of implantable biosensors. The simulations described here reveal key factors influencing the generation and collection of fluorescence from sensors implanted in the dermis at different depths and concentrations, which provides critical information for future work in instrument design. The simulation results show that the depths of implantation strongly influence the measurability of signal. The deeper the sensor is located, the more the signal is attenuated. With strong scattering and absorption of both excitation and emission light due to overlying tissue, the predicted ratio of output to input power ranges from 10^{-3} to 10^{-6}; and the signals generated from implants should be detectable at all depths within the dermis using sensitive detectors. The assessment of the spatial distribution of escaping fluorescence also provides useful information; it was found that 95% total signal (escaping fluorescence), even when excited with a 10mm diameter light source can be confined within a circular area on skin surface with diameter smaller than 18mm, which facilitates design of a matched optoelectronic system for efficient delivery of excitation, collection and analysis of luminescence response. Analysis of fluorescence output of different sensor configurations also indicates that the tightly-packed sensors are preferred because they yield higher fluorescence output with fewer particles. Thus, it is preferred to implant particles in a single site with high concentration. If the light source size can be varied with constant irradiance, a large light source is preferred to overcome the influence of unpredicted projection area change of implanted sensors in tissue. However, it is hard to control the particle distribution during implantation, and even though the tightly packed particles can yield more luminescence output, there are still other factors affecting the luminescence. For example, if the particles are packed densely, the space between particles for diffusion of blood glucose or oxygen may not be

enough for the sensors' response. Taking into multiply factors into consideration, if the highest dye concentration per sphere is achievable, moderately high particle concentrations for injection is desirable. The results of simulations to predict sensor *in vivo* performance show that the spectral distortion resulting from the absorption and scattering of the skin, particle size, or particle concentrations has minimal influence over the predicted ratiometric measurements. The focus of this work was to determine the effects of sensor configurations, implant depths, and excitation beam characteristics on the intensity, spatial and spectral distribution of escaping light. However, it is acknowledged that many practical questions regarding other factors that may also perturb the optical signals must also be answered before monitoring can be considered realistic. These include, for example, investigation of the influence of changes in blood volume, hemoglobin concentration and saturation, oxygenation shifts, and scattering increases due to formation of a fibrous collagen capsule around the implants.

In all, this simulation work supported the potential to accurately measure the output of luminescent implants and facilitated the design of a simple optical hardware system to communicate with dermally-implanted sensors. The purpose of the research in Section 3 was to investigate the photo transportation and interaction with implanted sensors. The results predicted the output signal after implantation, which facilitated the optical design in Section 4. The hardware design in Section 4 was based on the results in this section. These results not only could facilitate the hardware design for our dermally-implantable microparticle luminescent glucose sensors, they also were helpful for the design of other luminescent sensors implanted in skin.

4. DESIGN AND EVALUATION OF AN OPTICAL SYSTEM FOR SENSOR INTERROGATION*

4.1 Significance and background

To deploy and interrogate luminescence-based dermally implanted sensors *in vivo* for on-demand monitoring, it is necessary to design a matched optoelectronic system to interrogate our dermally-implanted microparticle sensors. It needs to be of high efficiency to deliver excitation light, collect luminescence, and measure luminescence. A bifurcated optical fiber bundle is commonly used to deliver excitation light and to collect luminescence from a scattering medium, but the excitation and collection efficiency is limited due to the numerical aperture and size limitation. In order to enlarge the probe size, a customized fiber bundle with hundreds fibers are used, but it is still costly, and the collection efficiency is still limited because locations for delivery of excitation light and those for collection of luminescence are separate, thus it is inevitable to lose luminescence coming from where excitation light goes in. To our knowledge, there is no commercial product or research report of a hardware design with high efficiency that is suitable for interrogation of dermally-implanted luminescence sensors. The aim of this chapter is to develop a hardware system that will overcome the shortcomings of current bifurcated optical fiber with respect to excitation and emission collection efficiency.

To evaluate the designed system while minimizing animal use, an evaluation phantom is needed. Thus, a stable and repeatable skin phantom mimicking optical properties of human skin is necessary to develop. Because of the stability and repeatability of the phantoms, they are useful in 1) initially testing system designs; 2) facilitate optimization of signal to noise ratio in existing system; 3) performing routine quality control; 4) comparing performance between system.[108] The history of tissue-simulating phantoms for optical diagnostic system began in

*Part of this section is reprinted with permission by R. Long, B. Collier, J. Roberts, and M. J. McShane, 2010, Proc. SPIE 757205, Copyright [2010] SPIE.

the early 1980s with the surge of clinical interest in near-infrared trans-illumination for breast cancer imaging [109-112]. Later interest rose from applications in photodynamic therapy and pulsed laser treatment [113-118]. In the early 1990s, generation of various types of tissue phantoms was spurred due to the introduction of spatially-resolved, time-resolved, and frequency-domain spectroscopy and imaging techniques. [119-124] In recent years, the applications of light in medicine have increased rapidly, since cosmetic laser surgery is a major commercial driving force. The research on tomography [125-130], photodynamic therapy, [114, 118, 131], etc, keeps the development of tissue-simulating phantom processing and important.

4.2 Methods

The aims of the hardware system design were 1) efficient delivery of excitation photons; 2) numerical aperture as large as possible (0.5~0.9) to obtain high collection efficiency; 3) compact size.

4.2.1 Hardware design

The hardware system for delivery of excitation light and collection of luminescent light was designed based on the results of modeling work, which was performed in the last section. The hardware system was consisted of the components to deliver excitation light, collect luminescence, and couple light into a commercial spectrometer. The measurement of spectrum of luminescence was performed with the commercial spectrometer. The aim of the system design is to overcome the shortcoming of bifurcated fiber bundle. Figure 26 is a scheme of the hardware design. The green LED was the excitation light source, since the sensors absorb green light strongly. Even though the sensors absorb light with shorter wavelength (such as UV) more strongly, the UV tends to denature the enzyme inside the sensors, and it is easier for the skin to

get burnt from UV light. Thus green light was chosen as excitation light source. The green LED light was collimated through a lens and delivered onto the dichroic mirror, and it was reflected by the dichroic mirror and focused onto the skin surface. The excited luminescent photons escaped from the skin surface and then were collected by the optical system. The luminescent light was collimated and went through the dichroic mirror and finally coupled into the spectrometer. In order to maximized the collection efficiency, which is defined as the ratio of luminescent photons collected by the system to the total luminescent photons escaping from the skin surface, modeling work were performed with OptiCAD to analyze the collection efficiency with variance optics.

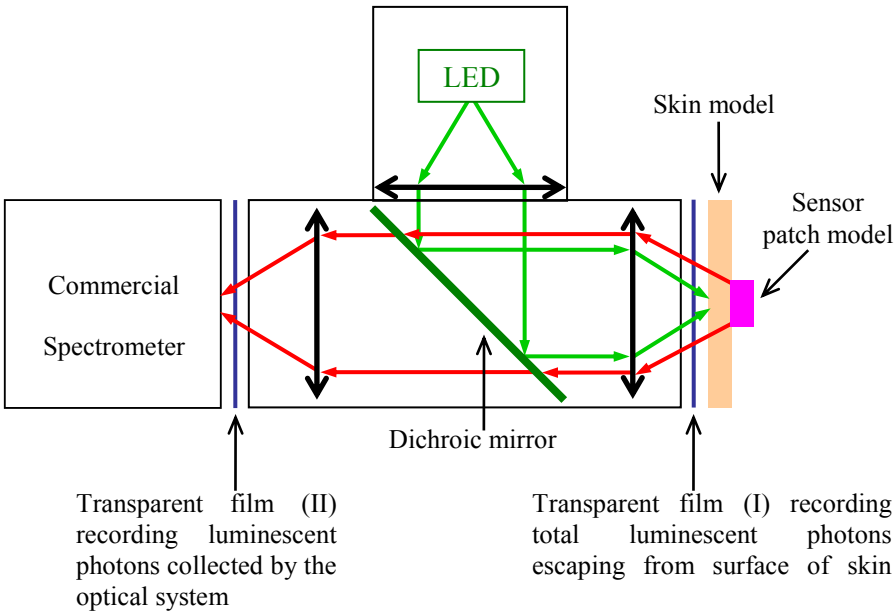

Figure 26. Scheme of modeling system for hardware design

In modeling, lens models were imported from the lens catalogue of OptiCAD, if using commercially available lenses. If not, lens models were designed according to the desired parameters. However, in order to reduce the cost, off-the-shelf lenses were preferred, unless a customized lens would greatly enhance the performance. Filters and mirrors were modeled as 100% transmittance or 100% reflectance initially to simulate an ideal situation. Sensor model and skin model were close to the real dimensions that would be used in experiments. The total escaping luminescent photons were recorded with the transparent film (I) (Figure 22) covering the surface of the skin model. The total luminescent photons collected by the hardware system were recorded with the transparent film (II) in the middle of Figure 22. Thus, the collection efficiency was equal to the ratios of the photons collected by the transparent film (II) to those collected by the film (I). The collection efficiency was optimized by varying lens position and lens shape until it reached maximum. The design criteria of the hardware system are 1) high interrogation and collection efficiency; 2) compact; 3) use off-the-shelf optics as many as possible to make it cost-effective. Interrogation efficiency is the ratio of the input excitation light power to that of luminescent photons collected with the hardware. Collection efficiency is the ratio of total escaping luminescence to that collected by the hardware. Though the interrogation efficiency depends on the implantation depths, optical properties of skin (phantom), and the size and concentration of the sensors, it was compared under the same conditions.

To evaluate a designed hardware system, evaluation medium is needed. In order to minimize the animal use, a skin phantom that matches the optical properties of skin is desirable for the experimental evaluation.

4.2.2 Development of evaluation phantom

A silicone based phantom was made to meet the criteria for our purposes (1) matching the optical properties of skin; (2) stable; (3) easily moldable; and (4) suitable for use in the dynamic test apparatus. The skin phantom would be used as an upper layer covering the sensor patch immobilized on a microscope glass slide to test the capability of the optical hardware during *in vitro* static test and then it could be used in a flow chamber system for later dynamic *in vitro* test. The anatomy structure of skin varies in different types and depends on the location of skin. Optical properties also vary in skin structure, age, color, body temperature, blood perfusion and locations. Moreover, the published optical properties of skin varied as well, particularly (reduced) scattering coefficients. Therefore, the goal was to make a skin phantom that sufficiently matches the highest values of published optical properties so as to present the worst-case scenario in terms of attention. If our hardware system is capable of detecting luminescent signal of sensors propagating through the developed phantoms, it should be sufficient to be moved forward into animal experiments and clinical tests.

4.2.2.1 Recipe design

Optical properties (μ_a, μ_s, g) of skin are dominated by epidermis and dermis [102], because absorption coefficients are mostly dependent on volume fraction of melanosomes in epidermis and cutaneous blood perfusion in dermis, while scattering coefficient and anisotropy factor (g) is dominated by dermis layer due to its big volume fraction in skin. Therefore, the extracted optical properties from publications were the averaged optical properties of epidermis and dermis layer according to their volume fraction in skin. To calculate average optical properties, the thickness of epidermis (100μm) and dermis (1900μm) are referred [62].

The main component of phantom is silicone elastomer base (SYLGARD® USA). Refractive index of silicone elastomer (1.410~1.414) [132] is similar to that of soft mammalian tissue (1.33-1.50) [133]. The main absorbing material used to mimic the main absorption attributes over excitation and emission range of our sensors (500nm-700nm) was cosmetic powder (Color Genius Pressed Powder, Deep Beige, Max Factor, Italy) [134]. Red ink (DESIGN Higgins®, SANFORD) was used as additional absorber to mimic the absorption properties of oxygenated blood. The scattering agent was Aluminum Oxide (Al_2O_3) powder (<10μm 99.7 % metals basis, Sigma Aldrich®).

The target μ_a is the volumetric average μ_a of skin based on a seven-layered skin structure [24]. The absorption coefficients of stratum corneum (10μm), epidermis (80μm), three dermis layer (100,1500, and 160μm), upper blood plexus (10% dermis and 90% blood, 80μm [24]) and deep blood plexus (90% blood and 10% dermis, 70μm [24]) were extracted from Van Gemert's paper [25] except the properties of blood which was extracted from [26]. All the absorption coefficients were averaged according to their volume fractions [20, 24, 27]. Because the absorption coefficients are mostly dependent on volume fraction of melanosomes in epidermis and cutaneous blood perfusion in dermis, the absorption coefficient (μ_a) of skin is dominated by epidermis and dermis [25]. The absorption spectrum (Figure 27) of red ink diluted by a factor of 5000 in deionized water and attenuation spectrum (Figure 27) of 1mg cosmetic powder diluted in 2mL silicone elastomer and cured for one hour at 70°C were measured by a spectrometer (USB 2000, Ocean Optics Inc.). Attenuation coefficient of the cosmetic powder used was close to that of cosmetic powder with same color and brand used in [134].

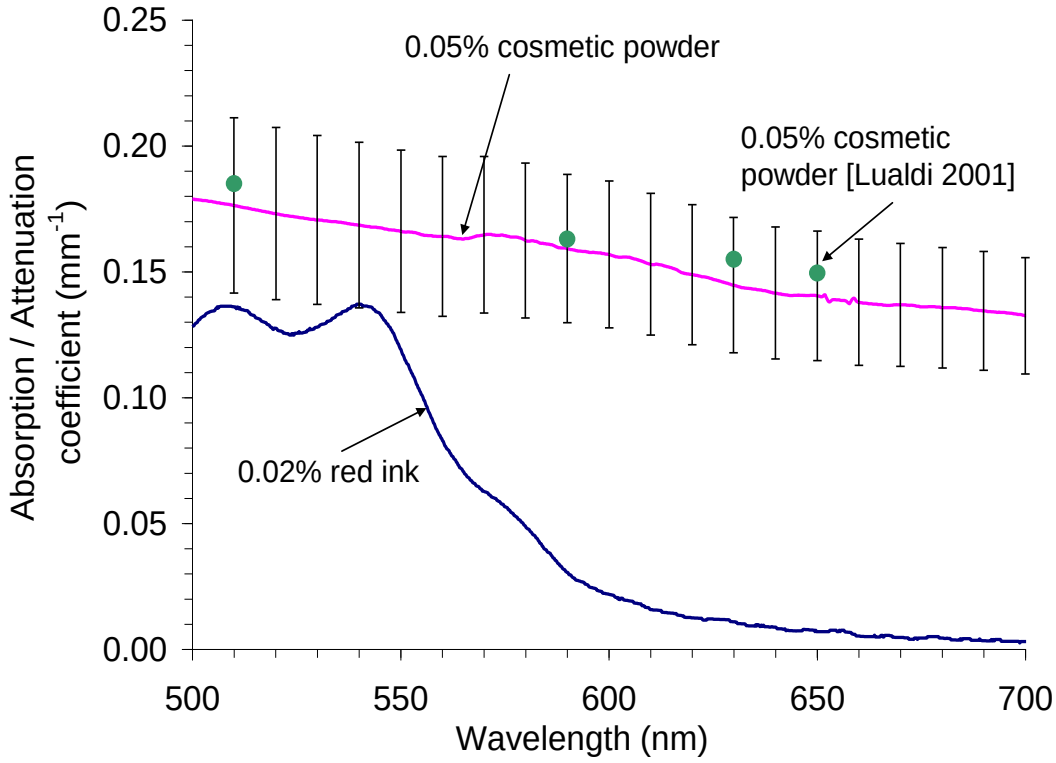

Figure 27. Absorption spectra of red ink (0.02% in deionized water) and attenuation spectra of cosmetic powder (1mg per 2mL silicone base) and error bars are one standard deviation. The solid circles are attenuation coefficients of cosmetic powder with the same color and same brand used in [134] .

The target μ_s or μ_s' were the volumetric average of μ_s' of epidermis (100μm, Wan et al [29]) and dermis (1900μm , Anderson et al [30]). Because μ_s' directly affects the effective attenuation coefficient ($\mu_{eff}^2 = 3\mu_a \times (\mu_a + \mu_s')$), the reduced scattering coefficient ($\mu_s' = (1-g) \times \mu_s$) of phantoms needed to be close to the maximum values of published data. So far, to our

knowledge, the highest reduced scattering coefficients of epidermis and dermis were calculated from Wan et al [29] and Anderson et al's [30] results of absorption parameter (K) and scattering parameter (S) of Kubelka-Munk model obtained from integrating sphere measurements, respectively. Conversion of Kubelka-Munk parameters (*K* and *S*) to absorption and reduced scattering coefficients (μ_a and μ_s') was using $\mu_a = \eta K$, and $\mu_s' = \chi S$ as the method in ref [25]. The thickness of epidermis for the calculation of volumetric average was 100μm and that of dermis was 1900μm [28]. Because the μ_s and μ_s' are dominated by dermis layer due to its big volume fraction in skin, most of the optical properties extracted from publications were the averaged optical properties of epidermis and dermis according to their volume fraction in skin. The concentration of Al_2O_3 powder in uncured elastomer base was predicted using Mie theory [31]. The scattering coefficient of Al_2O_3 powder in uncured elastomer base was calculated using Mie-theory assuming all the Al_2O_3 particles were uniform spheres with diameter 5.612μm that was the mode particle size of Al_2O_3 powder. Table 5 shows the parameters used in Mie scattering calculation and the calculated results [135]. The sphere concentration was 1.43×10^{-3} spheres/μm^3 and all the imagine index of refraction were 0 and number of angles was 200 in calculations, and Mie scattering calculation were carried out with online calculator [135]. The difference of predicted reduced scattering coefficients and those of skin were smaller than 10% except the one at 645nm.

Table 5. Parameters used in Mie Theory Calculation and results of calculation.

Wavelength (nm)	Refractive index		μ_s' (mm^{-1})				
	Silicone Elastomer	Al_2O_3	Epidermis [Wan] 100μm	Dermi [Anderson & Parrish] 1900μm	Skin (averaged)	Al_2O_3 (Mie Theory)	difference
540	1.41	1.77	13.25	11.10	11.20	10.32	7.87%
570	1.41	1.77	12.75	10.22	10.35	9.68	6.41%
585	1.41	1.77	12.69	9.85	9.99	9.32	6.74%
620	1.41	1.77	12.38	9.18	9.34	9.44	-1.06%
635	1.41	1.77	12.13	8.98	9.13	9.19	-0.61%
645	1.41	1.77	11.94	8.86	9.02	10.72	-18.84%
665	1.41	1.76	11.81	8.71	8.86	9.13	-3.02%

The final recipe of skin phantoms was settled to be 97.7mg Al_2O_3 powder, 12.66mg cosmetic powder, 1.67μL red ink in every 1mL silicone elastomer base (SYLGARD® USA).

4.2.2.2 Procedure of phantom fabrication

Al_2O_3 powder, cosmetic powder, and red ink into silicone elastomer base were mixed according to the recipe. The mixture was sonicated and stirred until homogeneous and then curing agent was added at 1:10 volumetric ratios of agent to base. The resulting mixture was stirred and cast into 34mm diameter molds (plastic Petri dishes) or spread onto a glass slide to achieve thinner phantom. After applying vacuum to remove bubbles in the mixture, the samples were cured at 70◦C for one hour in an oven. The thickness of phantoms ranged from 30μm to 1.8mm which was varied by dispensing different uncured elastomer volume into molds or applying pressure on two glass slides to sandwich uncured silicone mixture.

4.2.2.3 Determination of optical properties

The absorption coefficient (μ_a), reduced scattering (μ_s'), scattering coefficient (μ_s), and anisotropy factor (g) of cured skin phantoms were determined by integrating sphere (IS) measurement systems (Figure 24) and Inverse Adding-Doubling (IAD) software package (v 3.5.10, 11 May 2009) [136]. Total diffuse reflection (R) and diffuse transmission (T) were collected by the integrating sphere, and were spectrally analyzed with a grating-CCD spectrometer (USB 4000, Ocean Optics, Inc.). There two approaches of integrating sphere measurements: single-sphere and double-sphere. The single sphere means that one sphere is used at a time for diffuse reflectance or transmittance measurement, and two-sphere means that two integrating spheres are used at a time to measure reflectance and transmittance simultaneously. There are pros and cons to use two spheres. If the sample's optical properties change dynamically, then it is important to measure reflectance and transmittance simultaneously. However, it is difficult to make good contact on both sides of the samples with the two spheres, and it is hard to make the sphere calibration for the two-sphere system [137]. Because skin phantoms are of good thermal and chemical stability, it is not necessary to measure reflectance and transmittance simultaneously. Thus single-sphere measurements were performed. Spectrum of collimated (unscattered) transmission (U) was measured with setup shown in Figure 25. A pinhole (Thorlabs, Inc) was used to confine acceptance angle. Detector port (port 2 in Figure 24) of integrating sphere was connected with the spectrometer via a fiber (1mm core and 0.5 NA). Parameters of the integrating sphere (Labsphere®, North Sutton, New Hamsphere) were as follows: sphere diameter = 101.6mm; diameter of sample port (port 3 in Figure 2) = 12.7mm; diameter of entrance port (port 1 in Figure 26) = 12.7mm; diameter of detector port (port 2 in Figure 26) = 1mm, reflectivity of inner wall = 96%. The light source was Tungsten halogen light

source (LS-1, Ocean Optics, Inc.) emitting light collimated by a collimating lens (F220SMA, Thorlabs, Inc.). All the samples were sandwiched between two 1mm-thick microscope glass slides. IAD is a method to calculate optical properties of a sample by iteratively solving the radiative transport equation until the solution matches the input values of diffuse reflectance (M_R), diffuse transmittance (M_T) and (if desired) collimated transmittance (M_C) [138] that were calculated from measured R, T, and U.

For measurements of diffuse reflection (R), the light source was placed at the entrance port (port 1 in Figure 26) and sample was placed at sample port (port 3 in Figure 26). Integration time of the spectrometer was 1 second and the dark background spectra were subtracted in all measurements. The collimated illumination beam formed a spot 6mm in diameter on a sample. Because the distance from the edge of the illumination beam on the sample to the edge of sample port was 3.35mm that could be considered much larger than the lateral light propagation distance which was determined by $1/(\mu_a+\mu_s') \approx 1/(0.5+8) \approx 0.118$ (mm), then relatively little light should be lost out the side of the sample [139]. 10% and 50% reflectance standards (SRS-10-010, SRS-50 010, Labsphere®, North Sutton, New Hamsphire) (R=10% and R=50%) were used to get reflection spectra ($R_{10\%}$ and $R_{50\%}$) for calibration. Then diffuse reflectance (M_R) was calculated using the equation below:

$$M_R = \frac{R - R_{10\%}}{R_{50\%} - R_{10\%}} \times 40\% + 10\% \tag{22}$$

For diffuse transmission (T) measurement, the collimated light source was placed in front of the sample port (port 3) forming an illumination spot on a sample with diameter of 6mm again. Integration time of the spectrometer was 1 second, and dark background spectra were

extracted in all measurement, as well. The entrance port (port 1 in Figure 28) was blocked. Then diffuse transmittance (M_T) was calculated using equation as below:

$$M_T = \frac{T}{T_0} \tag{23}$$

T_0 was the spectrum collected without a sample present at the sample port.

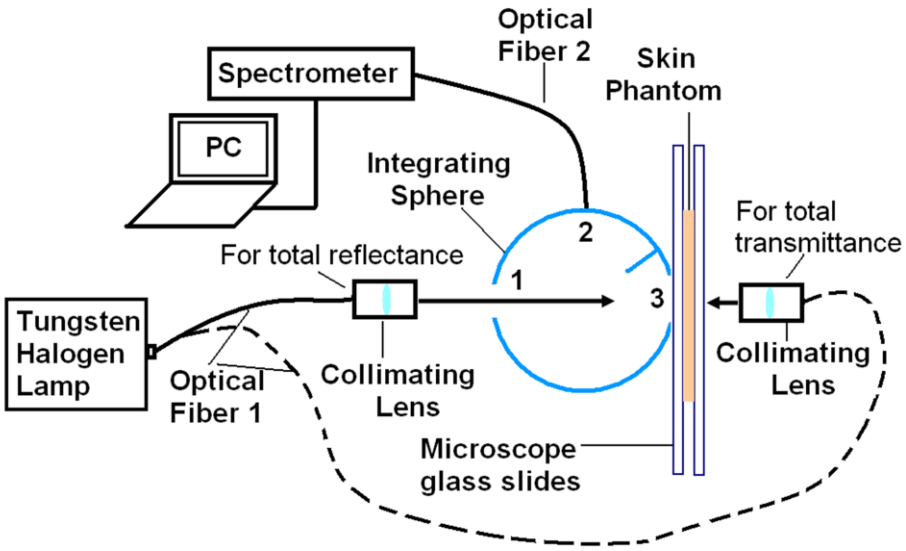

Figure 28. Scheme of integration sphere system to measure optical properties of skin phantoms

For collimated (unscattered) transmission (U) measurement (Figure 29), a pin hole (Thorlabs) with diameter of 0.86mm was placed in front of the spectrometer to limit the acceptance angle to 0.16°. Spectra of unscattered transmission (U) were collected by the spectrometer via optical fiber 3 (400μm core and NA 0.37) (Figure 25) coupled to the

collimating lens 2 (Thorlabs) attached to the pinhole. Collimated transmittance was calculated using equation below:

$$M_C = \frac{U}{U_0} \tag{24}$$

U is the spectrum of unscattered transmission of a sample and U_0 is the transmission spectrum without a sample at the sample port.

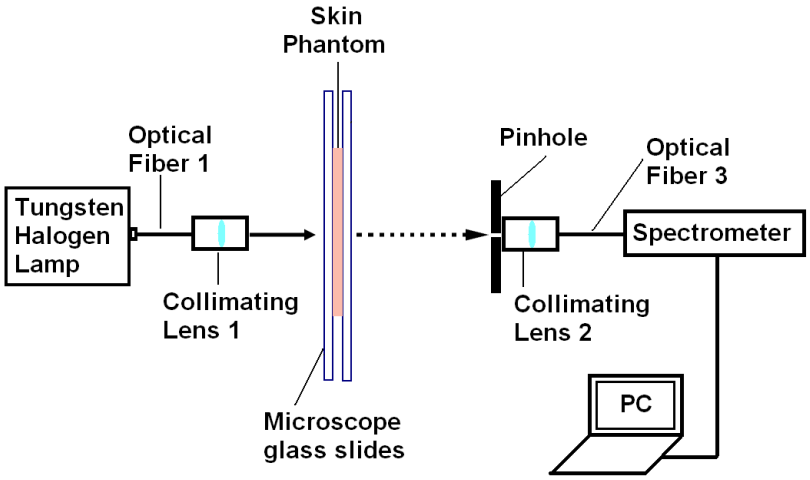

Figure 29. Scheme of system for measurement of collimated transmission.

Some samples were too thick to get a reliable signal, to make sure the collimated transmittance are reliable, collimated transmittance was plotted versus the sample thickness to check if this line was exponentially decreasing versus sample thickness. Input of diffuse reflectance (M_R), transmittance (M_T) and collimated transmittance (M_C) (three-measurement) in IAD calculation would yield absorption coefficients (μa), reduced scattering coefficients ($\mu s' = (1-g) \times \mu_s$) and anisotropy factor (g), so scattering coefficient (μ_s) could be calculated according to μ_s' and g. Input of only diffuse reflectance and transmittance would yield only absorption coefficients (μa) and reduced scattering coefficients (μ_s') from "two-measurement" calculation in IAD.

After the skin phantoms were developed, the simulations and experimental evaluations for the developed hardware system and the skin phantoms were performed to validate the accuracy of the developed phantom, and the simulations including Monte Carlo modeling and geometric ray-tracing for the system.

4.2.3 Simulation system

Simulations were performed using OptiCAD® (v10.046). The simulation system (Figure 30) modeled all the optics needed. All 1-inch spherical lens models were imported from the lens catalog of OptiCAD®. The models of aspheric lens were downloaded from the lens company's website as CAD files and imported into OptiCAD. Refractive index of glasses of lenses was imported from the source material of OptiCAD®. Aspheric lens models were tested in OptiCAD® with glass material applied in all cases, and the simulated focal lengths matched those reported in product data sheets. The simulations considered one excitation (540nm) and six emission wavelengths (570, 585, 620, 635, 645 and 665nm). The emission spectrum used in

simulations was collected when the sensors were exposed to air. As shown in Figure 26, the "photon capture film" was used as a "detector" to capture luminescent emission photons which would be collected by the optical fiber (NA=0.37, core diameter = 400μm). The size of the photon capture film and distance to the optical fiber confined the entrance numerical aperture to 0.22 that was the same as the commercial spectrometer used in experiments. A tube was positioned outside the aspheric lens to block the laterally reflected luminescent emission photons. The emission angle of the light source was shaped as a 60° cone. A homogeneous phantom model was created and the optical properties of phantom model were the values determined by integrating sphere measurement and IAD calculation. The refractive index of silicone elastomer for the six wavelengths (540, 570, 585, 620, 635 and 645nm) used in simulation was determined by using the equation below [132].

$$n = A + \frac{B}{\lambda^2} + \frac{C}{\lambda^4} \tag{25}$$

where, A = 1.399249923, B = 6.19643289×10^{-3}, C = -5.2646592×10^{-4}, λ is wavelength in vacuum with unit μm.

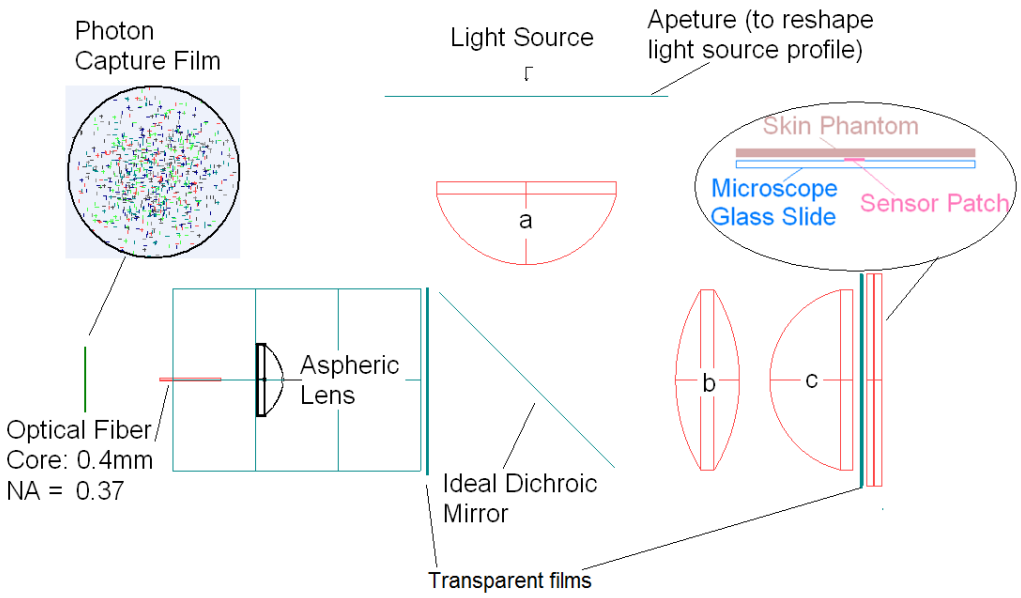

Figure 30. Scheme of simulation for the optical system. The photon capture film was used to model the detector situated at the position of the collimating lens in the spectrometer that confined the entrance numerical aperture to 0.22.

Microparticle sensor patch was modeled as a cylindrical slab with 3mm in diameter and 20μm high to mimic the dimension of sensor patch we used in experiment. Because the microparticle sensor samples were covered by a skin phantom but not embedded in skin phantom and the microparticles were dried and condensed packed, a homogeneous slab model should be sufficient to model *in vitro* situation. The absorption coefficient of sensors was calculated from the molar extinction coefficient ($11.16 mm^{-1}$) of sensors fabricated containing platinum octaethylporphine (PtOEP) and rhodamine isothiocyanate (RITC) as indicator and reference dyes, respectively [30]. Simulations were carried out for phantom models with different thickness to compare the results obtained from experiments.

Simulations of bifurcated fiber bundle (Figure 31) used previously were performed as well. The fiber bundle model is an approximation of the real fiber bundle used, since the excitation fibers and emission fibers were not randomly distributed as that of real fiber bundle. Other than that, fiber bundle model has the same parameters. The light source is shaped as a 25° cone to match the numerical aperture of fiber bundle that is 0.22. In figure 24, the photon capture film is attached at the end of emission fibers to collect photons delivered by the fibers. Covering film 1 with a 2.6mm diameter aperture at the center is used to block all the excitation photons leaking from the fiber bundle. Covering film 2 is a transparent film used to record total escaping photons. The phantom model and sensor model are the same as that in the previous simulation system.

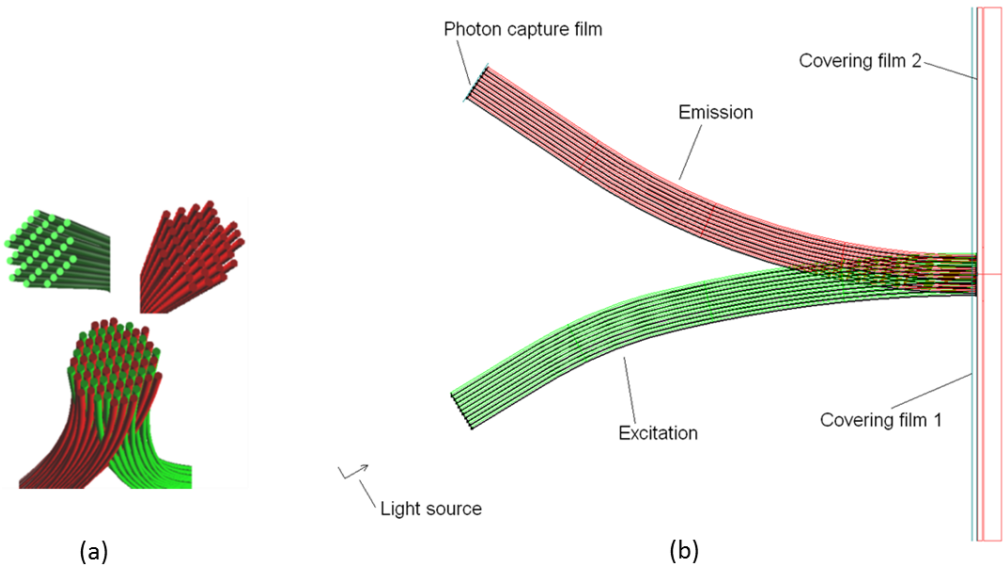

Figure 31. Scheme of simulation system of bifurcated fiber bundle system. Core is 200μm in diameter. NA=0.2; 37 fibers for excitation; 41 fibers for emission

4.2.4 *In vitro* experimental evaluation

4.2.4.1 Static experiments

Static *in vitro* experiments were performed to evaluate 1) accuracy of the measured optical properties of phantoms; 2) accuracy of the simulation system including Monte Carlo ray-tracing and geometric ray-tracing; and 3) the capability of the designed hardware working with the developed highly-scattering skin phantoms. A patch of sensor samples were immobilized on double-sided sticky tape attached to a glass slide and then it was covered by a skin phantom. Skin phantoms were placed adjacent to the last lens of part B of hardware (Figure 28) in experiments. The hardware system was mounted vertically in experiments. It delivered and focused excitation light on to a skin phantom and collected emission of sensors propagating through covering skin phantoms with different thickness. Power of excitation light focused on the skin phantom was 0.25mW and forming a spot with 2.5mm in diameter, so the average exposure intensity on a skin phantom was 0.051mW/mm^2 that was 39times smaller than the Maximum Permissible Exposure of human skin (MPE=2mW/mm^2)[107]. A grating-CCD spectrometer (USB 4000, Ocean Optics Inc.) connected with the hardware via an optical fiber was used to spectrally analyze luminescent emission collected. The integration time of the spectrometer was 25ms for every measurement in static *in vitro* experiment.

4.2.4.2 Dynamic experiment

Sodium alginate (low viscosity, 250 counts/s, MW 12-80 kDa), (3-glycidyloxypropyl) trimethoxysilane (GPTS), ammonium hydroxide, glucose oxidase (GOx, type VII from Aspergillus niger, 198 k units/g solid), catalase (CAT, from bovine liver, 2950 k units/g solid), β-D-glucose, and sodium acetate buffer were obtained from Sigma. Rhodamine isothiocyanate (RITC), sodium poly (styrene sulfonate) (PSS, MW ~70 kDa) and poly (allylamine

hydrochloride) (PAH, MW ~70 kDa) were obtained from Aldrich. Platinum(II) octaethylporphine (PtOEP) was purchased from Frontier Scientific. Tetrahydrofuran (THF, Fluka) and N-(3-dimethylaminopropyl)-N-ethylcarbodiimide hydrochloride (EDC) were obtained from Fluka. N-hydroxysulfosuccinimide sodium salt (NHSS) was purchased from Toronto Research Chemicals, Inc. An alginate-silica ("algilica") precursor was prepared by stirring a solution comprising 1.5 wt% aqueous alginate solution and glycidyl silane (GPTS) in a 1:1 volumetric ratio. Then, 2 mL of the precursor was added to 3 mL of water, and 1.25 mL of 10 M NH4OH was added to initiate the sol-gel process, followed by the addition of 10 mL of water and an additional stirring time of 40 min. An electrical sensing zone particle sizer (Micromeritic orifice was used to obtain the size distribution and concentration of particles comprising the stock suspension. In dynamic *in vitro* experiment, a flow-chamber apparatus (Figure 32) was used to control environmental variables (oxygen, glucose concentrations). Part B of hardware system was coupled into the flow-chamber to excite a sensor patch and collect luminescent emission. Setup of the hardware system and mobilization of the sensor patch were the same as that in static experiment, except that a sensor patch mobilized on a glass slide was then covered by a skin phantom on the other side of glass slide (Figure 32), because swelling of silicone skin phantom due to inner pressure of chamber needed to be avoided in order to keep thickness of the phantom constant. Excitation light from a green LED (λpeak=530nm, LS-530, Sandhouse, Dunedin, Florida, USA) was focused on the skin phantom with thickness of 372μm. The power of excitation light focused on the skin phantom was much smaller than that used in previous static *in vivo* experiment to avoid intense photon bleaching of sensors. Integration time of the spectrometer was 3s. All of the instrumentation (pumps, oxygen electrodes, mass-flow controllers, and the spectrometer) was controlled by a PC using a custom LabVIEW Virtual Instrument (National Instruments). The test was performed with the help of Brad Collier.

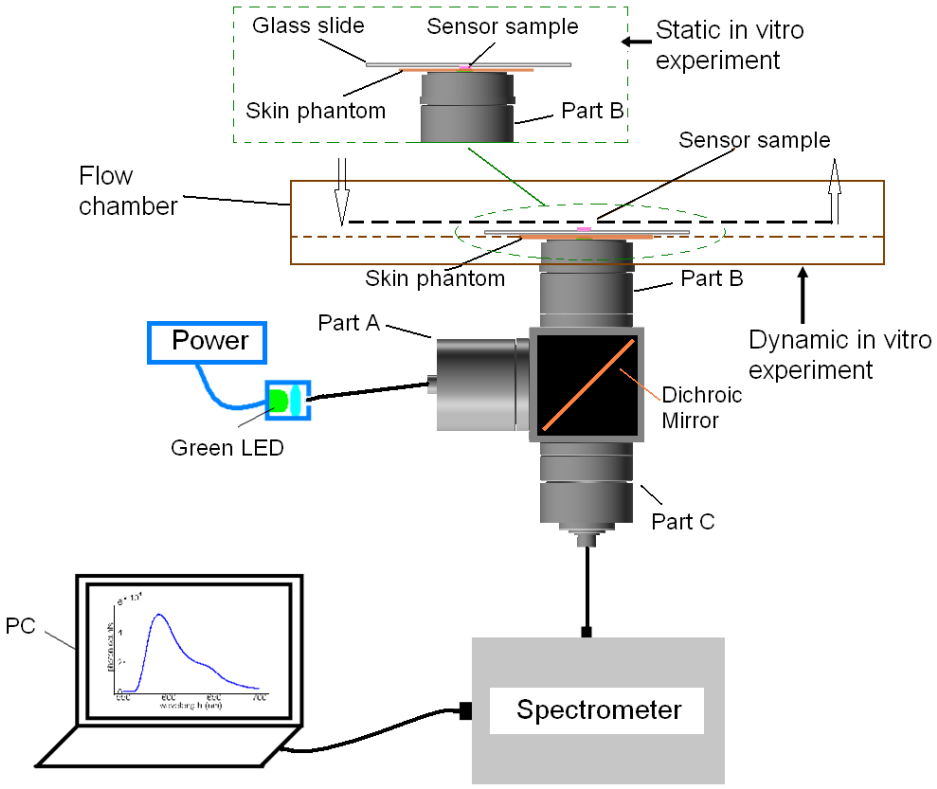

Figure 32. Scheme of static and dynamic experimental system

4.3 Results and discussions

4.3.1 Efficiency of hardware system

The simulated interrogation and collection efficiency of the hardware system was compared with that of the fiber bundle in Figure 33. The interrogation efficiency of hardware system was 200 times higher than that of the fiber bundle without a phantom covered on a sensor patch, and it dropped as the phantom went thicker, and it was 37 times higher than that of the fiber bundle with a 1.01mm phantom. Because the escaping luminescent photons spread wider at the deeper implantation depth, more photons escaped from the system. The collection efficiency of the

system was 320 times higher without a phantom and dropped to 62 times higher than that of the fiber bundle when the sensor was covered with a 1.01mm phantom covering. We also tested the interrogation efficiency experimentally using a power meter. The designed hardware system was ~100 times higher than that of the fiber bundle without phantom covered. The luminescent signal was too small for the power meter when covered with a phantom. This mainly because the sensors mobilized on a slide were not uniform and all the light source, filters and dichroic mirror in simulations were ideal but not in the experiment. There was a big photon loss up to 99.4% observed in experiments due to fiber connections of the spectrometer, so we could not use spectrometer to test the interrogation efficiency. The big photon loss needed to be overcome in the next stage.

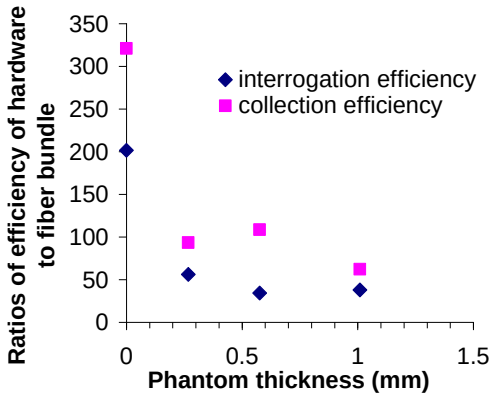

Figure 33. Simulated interrogation efficiency of the system.

A diagram of the hardware design is provided as below. In Figure 34, part A is for coupling of excitation light into the system. A plano-convex lens (D=25.4mm, f=25.4mm) is

used to collimate the excitation light from a green LED (λ_{peak}=530nm). The excitation filter in part A (560nm short pass, 3RD560SP, Omega) was used to cut the spreading tail of light source in the longer wavelength range. The dichroic mirror (Omega) mounted 45° was used to reflect excitation light into part B and to allow emission light to go through. Part B focused excitation light onto skin (phantom). A bi-convex lens (f=25.4mm) and a plano-convex lens (f=25.4mm) are used to focus the excitation light onto skin. Part C is for coupling of collected luminescent emission light into a spectrometer via an optical fiber (NA=0.37, D=0.4mm). An aspheric lens (NA=0.51, f=7.86mm, Thorlabs®) is used to couple luminescence light into the fiber. The emission filter in part C (3RD570LP, Omega) was used to filter out the excitation light leaking from the dichroic mirror.

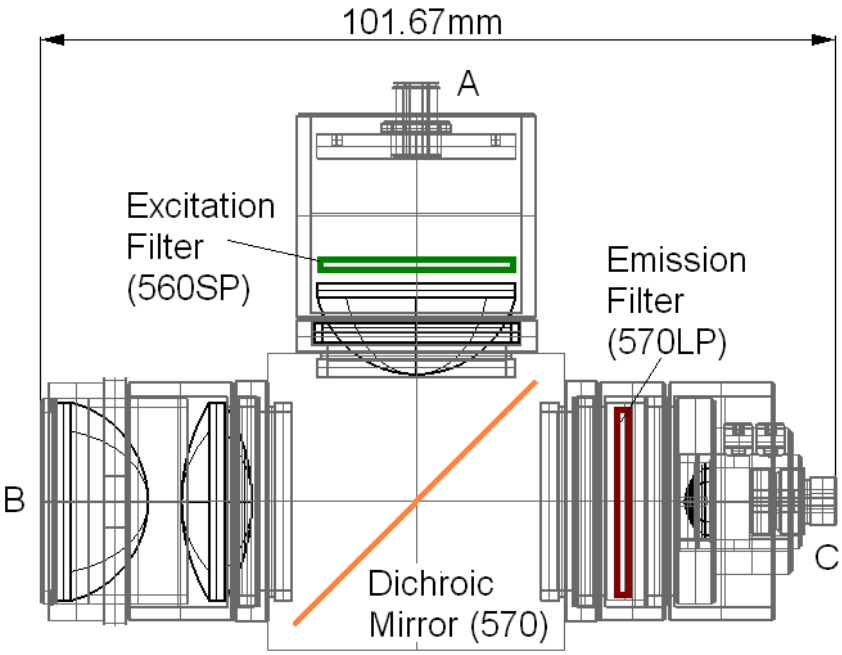

Figure 34. Diagram of the optical system.

4.3.2 Optical properties of evaluation phantom

For the phantoms with reliable collimated transmittance (four of fourteen samples), absorption coefficient (μ_a), scattering coefficient (μ_s), and anisotropy factor (g) were obtained from "three-measurement" with MR, MT, and MC as inputs in IAD calculation. For other phantoms that were too thick to get reliable collimated transmittance (ten of fourteen total samples), absorption coefficient (μ_a) and reduced scattering coefficient ($\mu_s' = (1-g) \times \mu_s$) were obtained through "two-measurement" with MR and MT as inputs in IAD calculation.

The optical properties of skin phantoms were calculated using IAD software with the input of M_R, M_T and M_C (if desired). To check the collimated transmittance (M_C) was reliable or not, it was plotted versus thickness of samples. Figure 31 contains a plot of averaged collimated transmittance at six wavelengths (540, 570, 585, 620, 635, 645, and 665nm) from which it can be seen that the reliable collimated transmittance (solid circles in Figure 35) decreased exponentionally versus phantom thickness. The unreliable M_C (solid triangles in Figure 35) would not be used as input in the three measurement method in IAD calculation. Data point "a" was eliminated, because R-square (0.87) was smaller than 0.95 if data point "a" was involved in linear regression. Data points "b – f " were eliminated since they were smaller than 7.5×10^{-5} which had the same order of magnitude as the smallest resolution of collimated transmittance (2.5×10^{-5}) determined by the maximum photon counts (40000) detected during measurement. Data points g - j were originally zeros and were added 1×10^{-6} to be plotted in log scale in Figure 35. Intercept of the linear regression line must pass through the value when the phantom thickness was zero, which was the transmittance calculated from Fresnel's law . This can be roughly calculated using the refractive indices of glass (n = 1.5) and air (n = 1), when the multiple internal reflectances were neglected. When sample thickness was 0, the calculated $M_C = 0.96^4 = 0.85$, which was close to the measured values (0.85). Unreliable data points may be

attributed to the thickness of phantoms that were too thick, and movement artifact in the measurement.

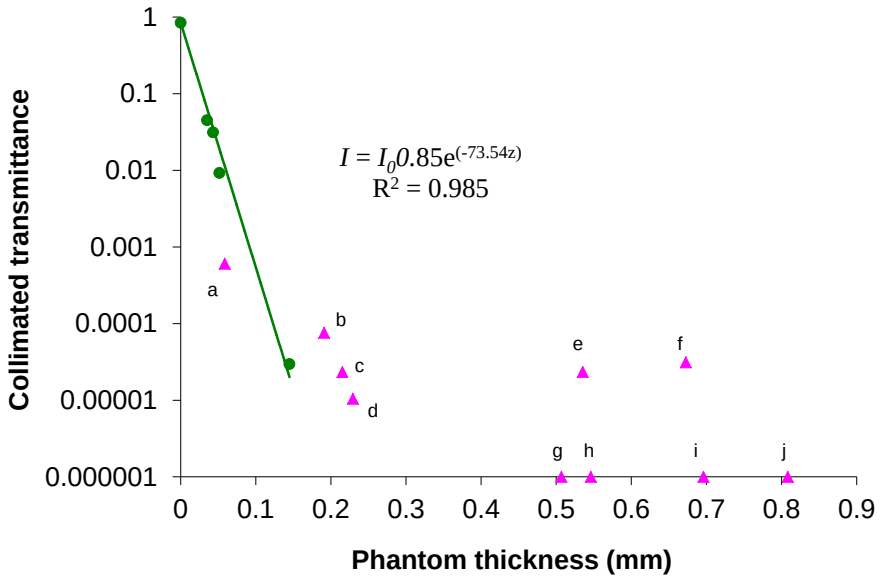

Figure 35. Collimated transmittance versus phantom thickness.

For the phantoms with reliable collimated transmittance (four of fourteen samples), absorption coefficient (μ_a), scattering coefficient (μ_s), and anisotropy factor (g) were obtained from "three-measurement" with M_R, M_T, and M_C as inputs in IAD calculation. For other phantoms that were too thick to get reliable collimated transmittance (ten of fourteen total samples), absorption coefficient (μ_a) and reduced scattering coefficient ($\mu_s' = (1\text{-}g) \times \mu_s$) were obtained through "two-measurement" with M_R and M_T as inputs in IAD calculation.

The measured optical properties (μ_a μ_s' μ_s g) were presented in Figure 36-39, and the

error bars are one standard deviation. In Figure 36, solid diamonds are measured μ_a of phantoms. The solid line and dashed lines are extracted from Jacques' work [140-142]. Solid line at the top is the μ_a of darkly pigmented skin (melanosome 30.5%); the dashed line in the middle is the μ_a of the moderately pigmented skin (melanosome 13.8%); dashed line at the bottom is the μ_a of light skin (melanosome 3.8%); open circles are extracted from Bashkatove et al's work [139]; open triangles are extracted from Prahl's thesis [143]; open diamonds are extracted from Chan et al's paper [144] ; open squares are the volumetric average μ_a of skin based on the μ_a of stratum corneum, epidermis and dermis summarized in Van Gemert's paper [102]. The phantom data agreed well with the μ_a (solid line in Fig. 2) of darkly pigmented adult's skin with a typical volume fraction of oxygenated-blood 0.2% in dermis, and they also agreed well with μ_a (open squares) summarized in Van Gemert's paper , and at longer wavelength range, μ_a of phantoms agreed with Chan et al's data (open diamonds) . Other than these data, they are higher than other published data. Jacques' data (solid line and dashed lines) were the volumetrically averaged value of μ_a of epidermis (100μm) and μ_a of dermis (1900μm) [145]. In Jacques' work, μ_a of epidermis was the sum of μ_a of skin baseline and μ_a of melanosome. Absorption (μ_a) of skin baseline was based on the measurement of bloodless rat skin using integrating sphere from unpublished data of Huang and Jacques [140], and μ_a of melanosome was based on the various published studies of the threshold exposure for explosive vaporization of melanosomes by pulsed lasers at various wavelengths [140-142]. The fractions of melanosome used for calculation of μ_a of epidermis are 3.8%, 13.8% and 30.5% which are the average value of fraction for light skin, moderately pigmented skin and darkly pigmented skin [142]. Bashkatove's Data (open circles) [139] were the μ_a of samples obtained from post-mortem examinations. Prahl's [143] data (open triangles) was obtained from bloodless human dermis. Chan's data (open diamonds) in were the absorption coefficients of a Caucasion female donor (age 72).

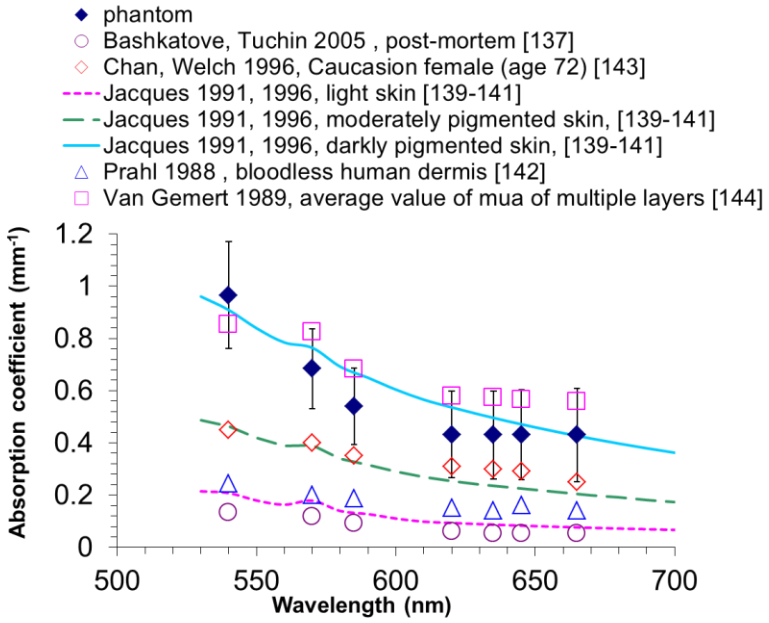

Figure 36. Absorption coefficients

The reduced scattering coefficients (μ_s') of phantoms were compared with those in publications in Figure 37. Solid diamonds are μs' of phantoms; open squares are the volumetric average μs' of epidermis and dermis extracted from Wan et al [146] and Anderson's [147] work respectively; dashed line is extracted from Jacque's work [140, 148]; open triangles were extracted from Prahl's thesis [143]; open circles are extracted from Bashkatove et al's paper [139]; open diamonds were extracted from Chan's paper [144]; crosses were predicted $\mu s'$ based on Mie scattering. The μ_s' of phantoms (solid diamonds) were obtained from fourteen samples using "two-measurement" IAD calculations. The phantom data did not have an obvious decreasing trend versus wavelength, which was similar as the predicted values (crosses in Figure 33) by Mie scattering calculations. The reduced scattering coefficients of phantoms were higher

than most published data except the averaged of Wan [146]and Anderson's [147] data at shorter wavelength, but μ_s' of phantoms agreed well at longer wavelength with them.

The published μ_s' of skin were averaged according to the volume fraction of epidermis (100μm) and dermis (1900μm) [145]. Jacques' data (dashed line) was the sum of μ_s' of Mie scattering from collagen fibers and μ_s' of Rayleigh scattering from small-scale structures [140, 148]. Predicted values (crosses) were results of Mie scattering caclulation based on the uncured silicone base assuming 5.6μm Al_2O_3 sphere with 1.43×10^{-3} spheres/μm^3 uniformly distributed.

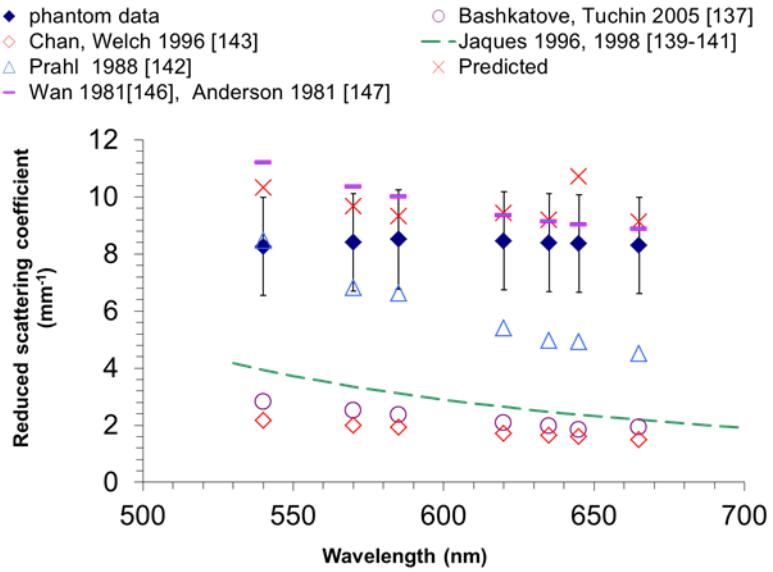

Figure 37. Reduced scattering coefficients (μ_s').

The measured scattering coefficients (μs) of phantoms were compared with published scattering coefficients in Figure 38. The measured scattering coefficients of phantoms were obtained from calculation of reduced scattering and anisotropy factor obtained from four of

fourteen samples calculated with "three-measurement" method of IAD. Scattering coefficients from publication varied a lot, as well, while the phantom data were close to one of maximum value of published data. Scattering coefficients of Jacques' data (dashed lines) were calculated from the reduced scattering coefficients with the g varied from 0.7 to 0.95 [140, 148, 149]. The predicted data (×) in Figure 38 were calculated from Mie scattering.

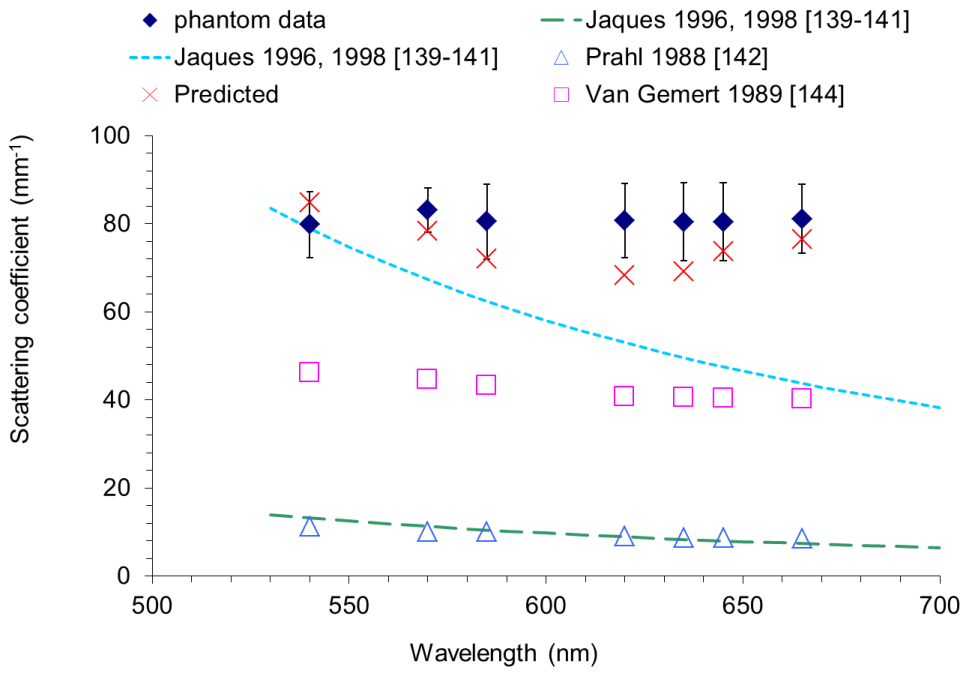

Figure 38. Scattering coefficient (μs)

Measured anisotropy factors (g) of the phantoms (solid diamonds) given in Figure 39 were also obtained from four of fourteen samples with "three-measurement" method of IAD. The g were within the range 0.7 to 0.95 which is the range of anisotropy factors of skin in [140, 149]. The anisotropy factors of phantoms were close to upper boundary of published values, as

well as the predicted values (crosses). However, for the photon diffusion in biological tissue which involves many scattering events, the details of scattering coefficient (μ_s) and anisotropy factor (g) become less important than reduced scattering coefficient (μ_s') [140]. As long as the anisotropy factor and scattering coefficients of phantoms are in between the maximum and minimum published values, and they should be sufficient for our purpose.

The optical properties of skin phantoms were aimed to match the maximum published values to our knowledge to present an evaluation medium of highest attenuation. The absorption coefficient of phantoms matched those of darkly pigmented skin published so far. The reduced scattering coefficients also matched the highest published values to our knowledge. As system evaluation mediums, the skin phantoms can enable the system testing and optimization without unnecessary use of animal or human tissue.

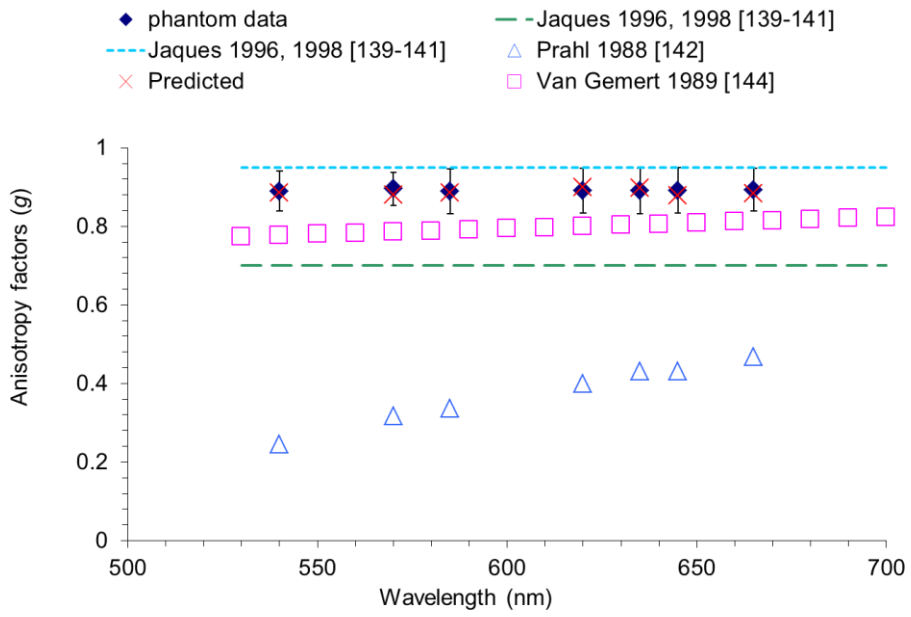

Figure 39. Anisotropy factors (g).

4.3.3 Comparison of static experiment and simulations

In experiments, the emission generated from a patch of sensor samples and transporting through a skin phantom was collected by the optical system and analyzed by the spectrometer. In simulations, six wavelengths were simulated for the optical system and skin phantom models with various thicknesses. The attenuation ratios at three typical wavelengths (585, 620 and 645nm) were calculated for comparison. In Figure 40, solid triangles are results of simulations that were applied parameters resulting in maximum effective attenuation coefficients, which predict the lower boundary of attenuation ratios. The solid squares are results to predict the upper boundary of attenuation ratios. In Figure 40, all the experimental data (open diamonds) fall in between the predicted upper and lower boundary of attenuation ratios, which proved the accuracy of measured optical properties of phantom. The slopes of experimental data in Fig. 36 were 10.52, 10.01, and 10.08 for 585, 620 and 645nm, respectively. The average effective attenuation coefficients ($\mu_{eff}^2 = 3\mu_a \times (\mu_a + \mu_s')$) of phantoms are 5.17, 3.83, 3.40, and 3.37 (1/mm) for 540, 585, 620 and 645nm, respectively. The total attenuation of luminescence should be associated with the sum of μ_{eff} of excitation (540nm) and emission (585, 620, 640nm) wavelengths. Because 540nm was the only excitation wavelength simulated, the sum of μ_{eff} of excitation wavelength and emission wavelengths were 9.0, 8.57, 8.55 (1/mm) for 585, 620 and 645nm respectively. The differences of the slopes in Fig. 36 and the sum of μ_{eff} of excitation and emission were around 15%, this may be attributed to the differences of interrogation efficiency between the cases without phantom and those with phantoms.

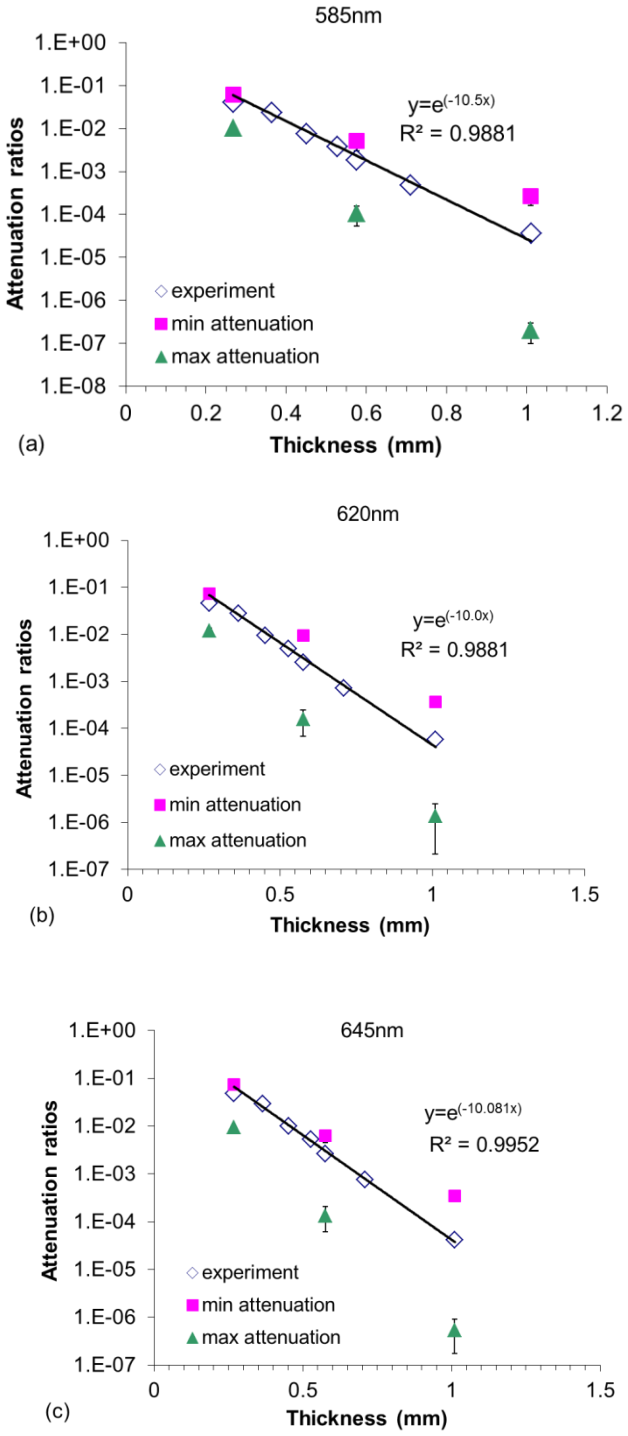

Figure 40. Attenuation ratios of emission intensity with a phantom covered to that without a phantom covered.

In previous work [150], the measurability of luminescent signal was predicted and the luminescent signals generated from implants were concluded to be detectable at all depths (0.5~1.7mm) within the dermis using detectors such as avalanche photodiodes or photomultiplier tubes. The intensity of excitation light focused on skin phantoms in static *in vitro* experiment was 0.051mW/mm^2 that was 40 times smaller than MPE of human skin. In experiments, the luminescent signal through phantoms up to 1010μm thick was detectable using a grating CCD spectrometer. The detectability was determined according to the detectable signal that was on the same order of magnitude of dark signal. Therefore, any signal smaller than that should be unreliable. If the incident excitation light was the MPE of human skin, the detectable thickness could be around 1357μm according the equations in Figure 19. The measurability also depends on the types of detectors, if a more sensitive detector would be used, the detectable thickness could be greater.

4.3.4 Dynamic experiment

Figure 41 (a) and (b) are the result obtained from in dynamic flow-chamber in vitro test. Luminescent emission through a 372μm skin phantom was collected by the hardware. The percentage changes of peak ratios (PtOEP 645nm /RITC 585nm) versus different glucose concentrations. The baseline is the peak ratio at zero glucose concentration. The analytical range is defined as the concentration range of glucose which can be statistically differentiated. The lower limit of the analytical range is defined as detection limit, while the upper limit is the analyte concentration observed when the response profile deviates 10% from linearity.[29] In Figure 41, it was observed that upper limit of the analytical range was smaller than 100mgL. The analytical range of 2~120mg/dL was reported [29, 30] previously. This might be attributed to several factors: 1) the filters in the optical system were not ideal so they could not filter out of

the back scattered excitation light which introduce more noise; 2) there were some interference between the reference emission and sensing emission. The scattering coefficient of the phantom used in this experiment was ~80mm^{-1} which is much higher than that of animal skin. Figure 37 indicates that the sensor response through a 337μm skin phantom to different glucose concentration was measurable, though the analytical range was affected. Thus, it was anticipated that there should be no significant obstacle to observe the sensor response to variation of glucose in vivo analysis with this optical system.

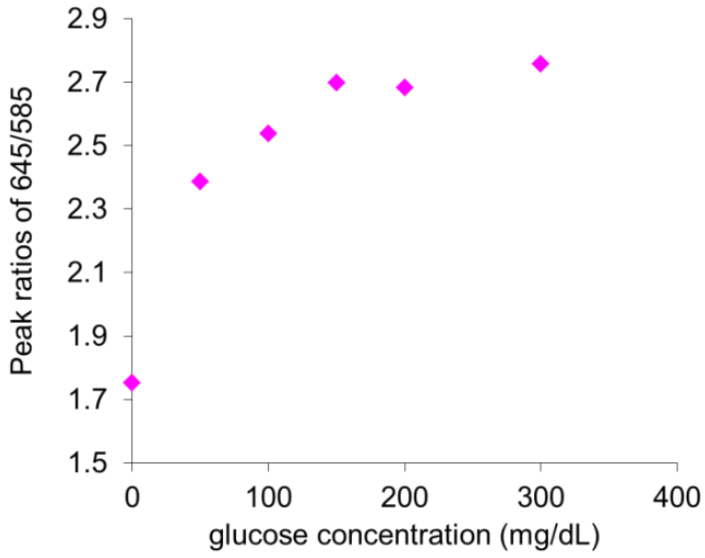

Figure 41. (a) in vitro data of peak ratios (645nm/585nm), (b) % changes of peak ratios (645nm/585nm) versus glucose concentration.

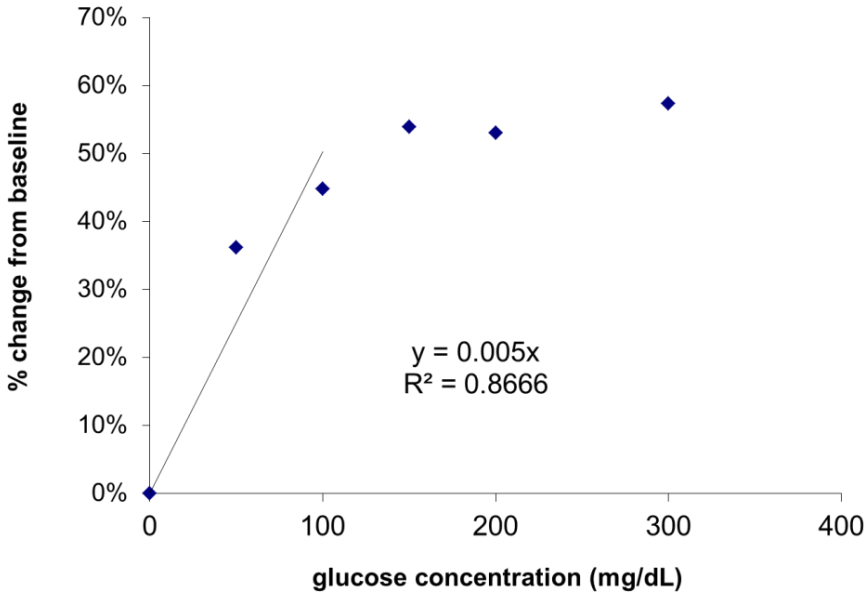

Figure 41. Continued

4.4 Conclusions

An optical system of high efficiency was designed to interrogate dermally-implanted microparticle sensors. The evaluation medium is the developed silicone-based skin phantoms which match the maximum value of the published optical properties of human skin. The phantoms have advantages of stability and feasibility to produce multi-layered structures and can be used to facilitate the evaluation and optimization of the hardware system. Experimental validations showed a good agreement with results of simulations, proving the accuracy of measured optical properties of developed skin phantom, and the accuracy of the simulation system including Monte Carlo ray-tracing and geometric ray-tracing. Further development and many more experiments are required to establish whether the proposed implantable sensor technology can yield accurate blood glucose predictions, and how long the implants can operate

in situ. However, these evaluation of the hardware system with skin phantoms indicate that there should be no obstacles for the optical hardware to meet expectations for *in vivo* analysis of implants. The phantoms and optical system will be used for extensive *in vitro* sensor validation prior to use in animal experiments, and more animal experiments will be carried out in the future, as well. We also need to point out that photon loss at the connections of hardware needs to be overcome for optimal performance in the future.

5. OPTIMIZATION OF THE OPTICAL SYSTEM

5.1 Significance and background

5.1.1 The problem of photon loss with commercial spectrometer

During experimental evaluations performed in Section 4, it was noticed that the system efficiency was compromised due to the photon losses between the fiber connections and the entrance aperture of the CCD spectrometer. The photon loss was found to be 99.97% with a 0.7mm thick phantom when measured with a power meter. This matched predictions from simulations wherein the photon loss between the fiber and entrance aperture of a spectrometer was greater than 99.9% with covering phantom models, and it went up as thickness of phantoms increased. Even without a phantom covering on the model of a sensor patch, there was still 99.85% of photon loss at the entrance of the spectrometer. Photon loss of the system in simulations was around 99.93%, 99.96% and 99.97% with 0.268, 0.576 and 1.01mm thick phantom models, respectively. The problem of photon loss is an inevitable trade-off of the spectrometer, and highlights the need for a custom solution to improve optical efficiency for the weak signals expected from implanted sensors.

5.1.2 The optics of spectrometers [150]

5.1.2.1 Basic structure

There are many configurations of an optical spectrometer, but the basic structure of an optical spectrometer consists illumination, collimation, dispersing, focusing and detection system (Figure 42). Illumination is the object that a spectroscopic system is applied to study. It can be a certain light source, or luminescence from a sample excited by a light source. The collimation system is composed of an entrance slit and collimating optics. Light that enters the entrance slit

is collimated by collimating optics before getting dispersed. The size of the entrance slit can affect the system resolution and throughput. The dispersing system can be a grating or a prism, which depends on the applications. The dispersing system also controls the spectral resolution. The focusing system focuses the dispersed light onto the image plane. The detection system receives the images of dispersed light and represents the intensity of the images in terms of electronic signals.

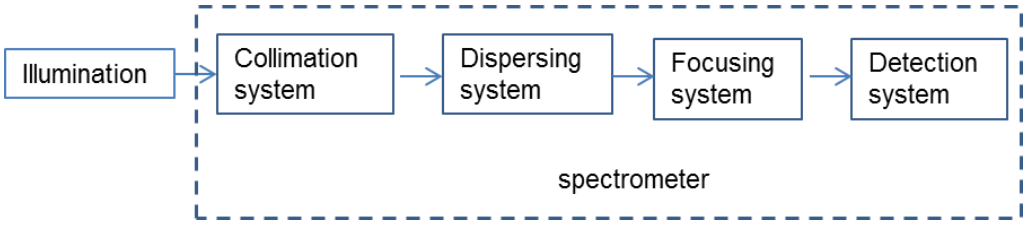

Figure 42. Scheme of a basic spectrometer

The dispersing system is the major part of a spectrometer. The most common dispersing components used in spectrometers are prisms and diffraction gratings. The advantage of a dispersing prism (Figure 43) is that it has nearly 100% transmission efficiency. However, the disperse angle is small compared with a diffraction grating. Either enlarging the work space or adding multiple mirrors may work when using prisms, but it is hard to build a compact setup.

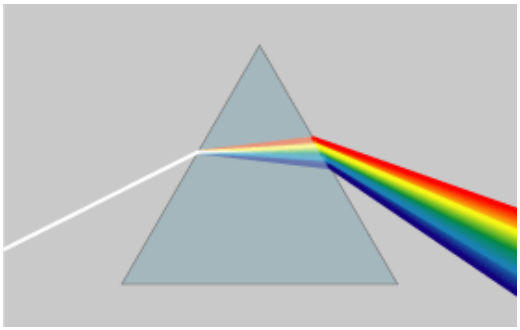

Figure 43. Dispersion prism. [151]

A diffraction grating (Figure 44) is a collection of reflecting (or transmitting) elements separated by a distance comparable to the wavelength of light under study[152]. A reflection diffraction grating consists of a grating superimposed on a reflective surface, whereas a transmission diffraction grating consists of a grating superimposed on a transparent surface.[153] The most fundamental grating equation that states the relationship between the groove density of a grating and the angles of the incident and diffracted beams is given as:

$$\sin\alpha + \sin\beta = 10^{-6}Nm\lambda \qquad (26)$$

In the grating equation, N(1/mm) is the groove density of a grating, m is the diffraction order, α and β are the incident and diffracted angles, and λ (nm) is the incident wavelength.

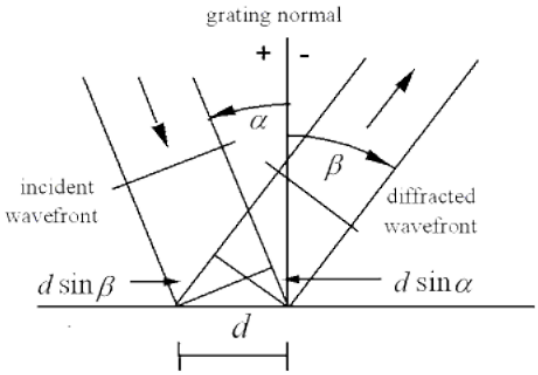

Figure 44. Geometry of diffraction, for planar wavefront. [153]

5.1.2.2 Dispersion of a grating

The angular dispersion is the angular spread $d\beta$ of a spectrum of order m between the wavelength λ and $\lambda+d\lambda$. The angular dispersion can be obtained by differentiating the grating equation, and is defined as:

$$\frac{d\beta}{d\lambda} = \frac{10^{-6}Nm}{cos\beta} \tag{27}$$

The ratio of $d\beta$ and $d\lambda$ is angular dispersion. As the groove density (N) increases, the angular dispersion increases, which means that the angular separation between wavelengths increases for a given order m as the groove density increases.

The linear dispersion of a grating system is the product of the angular dispersion and the effective focal length (f) of the grating system. It defines the extent to which a spectral interval is spread out across the focal plane of a spectrometer.

$$\frac{dx}{d\lambda} = \frac{10^{-6}m}{cos\beta} f \tag{28}$$

where, f is the effective exit focal length in mm.

The linear dispersion is the ratio of *dx* to *dλ*. Thus, according to the linear dispersion equation above, we can see that a longer effective focal length (*f*) can yield a bigger linear dispersion, which means that a spectral interval can spread out wider across the focal plane. The reciprocal linear dispersion (*dλ/dx*) is called the "plate factor" (*pf*). The *pf* is a measure of the change in wavelength (nm) responding to a change in position along the spectrum. A longer focal length can result in a smaller plate factor, which results in a smaller change in wavelength responding to a change in location, so longer focal length can result in a better wavelength resolution.

5.1.2.3 Resolving power, spectral resolution and band-pass [152]

Resolving power is a theoretical concept and is given by:

$$R = \frac{\lambda}{d\lambda} \tag{29}$$

where, $d\lambda$ is the limit of resolution, the difference in wavelength between two lines of equal intensity that can be distinguished. The theoretical resolving power of a planar diffraction grating is given as:

$$R=mN' \tag{30}$$

where *m* is the diffraction order, and *N'* is the total number of grooves illuminated on the surface of a grating. The grating equation can be used to replace m as below:

$$R = \frac{10^6 N(\sin\alpha + \sin\beta)}{n\lambda} \tag{31}$$

where, *W* is the illuminated width of the grating. $W = \frac{N\prime}{N}$

thus , $R = \frac{10^6 W(\sin\alpha+\sin\beta)}{\lambda}$

because $|\sin\alpha + \sin\beta| < 2$

The maximum attainable resolving power is:

$$R_{max} = \frac{2 \times 10^6 W}{\lambda} \tag{32}$$

The degree to which the theoretical resolving power is attained depends not only on the incident and diffraction angles, but also on the quality of the grating surface, the uniformity of the groove spacing, the quality of the associated optics, the width of the slits and detector elements, and aberrations. Any departure of the diffracted wavefront greater than λ/10 will result in a loss of resolving power due to aberrations at the image plane.

Though the resolving power can be considered as a characteristic of the grating, it is important to note that the ability to resolve two wavelengths depends not only on the grating but also on the dimensions and locations of the entrance and exit slits, the aberrations in the images, and the magnification of the images. The minimum wavelength difference between two wavelengths that can be resolved unambiguously can be determined by convolving the image of the entrance aperture (at the image plane) with the exit aperture (or detector element). This ability of a grating system to resolve wavelengths is arguably more relevant than resolving power, since it takes into account the image effects of the instrument system. Resolving power is a dimensionless quantity, and resolution has spectral units.

The band-pass and resolution are both used as a measure of the instrument's ability to separate adjacent spectral lines. The band-pass (BP) of an instrument is the spectral interval that can be isolated. It depends on the following factors: the width of the grating, system aberrations, spatial resolution of the detector, and entrance and exit slit widths. Spectrometers are not perfect: they produce an apparent spectral broadening of the purely monochromatic wavelength. The line profile has finite width and is known as the instrument line profile (instrumental bandpass). An estimation for bandpass is the product of the exit slit width w' and the reciprocal linear dispersion.

$$BP \approx W' \times P \tag{33}$$

An instrument with a smaller bandpass can resolve wavelengths that are closer together than an instrument with a larger bandpass. The bandpass can be reduced by decreasing the width of the slit, but usually at the expense of decreasing light power as well.

Assuming monochromatic light, the bandpass is defined as the full width at half maximum (FWHM) of the trace. Because any spectral structure is the sum of infinite number of single monochromatic lines at different wavelengths, the relationship between the instrumental line profile, the real spectrum and the recorded spectrum is given by:

$$F(\lambda) = B(\lambda) * P(\lambda) \tag{34}$$

The recorded function *F(λ)* is the convolution of the real spectrum *B(λ)* and the instrumental line profile *P(λ)*. The shape of the instrumental line profile is a function of various parameters: 1) the width of the entrance slit; 2) the width of the exit slit or of one pixel; 3) aberrations; 4) quality of the system's components and alignment; 5) diffraction phenomena. Each of these factors can be characterized by a special function $P_i(\lambda)$, thus the overall instrumental line profile P(λ) is related to the convolution of the individual terms:

$$P(\lambda)=P_1(\lambda)*P_2(\lambda)*\ldots*P_i(\lambda) \tag{35}$$

Thus, a spectrometer with a smaller-width slit, smaller-pixel detector and less aberration can have a narrower instrumental line profile, which results in a better spectral resolving ability. In summary, according to the definitions of linear dispersion, resolving power, and bandpass, the spectral resolving ability of a spectrometer is mainly dependent on these factors: 1) groove density of the grating (if a grating is used); 2) the effective focal length of the spectrometer; 3) the size of the pixels on the detectors (exit aperture); 4) size of entrance aperture and slit; 5) system aberrations.

5.1.2.4 Throughput and etendue [150]

Geometric etendue, (G), characterizes the ability of an optical system to accept light. It is a function of the area (S) of the emitting source and the solid angle (Q), into which it propagates. Etendue is a limiting function of system throughput.

$$G = \iint dSdQ \tag{36}$$

In a spectroscopic system, the etendue is estimated by:

$$G \approx S_{es} \times Q \tag{37}$$

where, S_{es} is the area of the entrance slit.

Thus, the throughput of the system basically depends on 1) size of entrance aperture and slit; 2) numerical aperture. Thus, there is an inevitable trade-off between spectral resolution and throughput of a spectrometer system. As noted above, spectral resolution can be increased by decreasing the entrance slit and numerical aperture that can result in smaller aberrations at the expense of sacrificing the light power.

5.1.2.5 The optical invariant

The optical invariant (Lagrange invariant) is a constant for an optical system. In Figure 45, the optical invariant throughout the entire system is defined as below:

$$Inv = hnu = h'n'u' \tag{38}$$

where, h and h' are the heights of object (S) and image (S'), u and u' are the ray slopes of object and image, and n and n' are the refractive index of object space and image space, respectively.

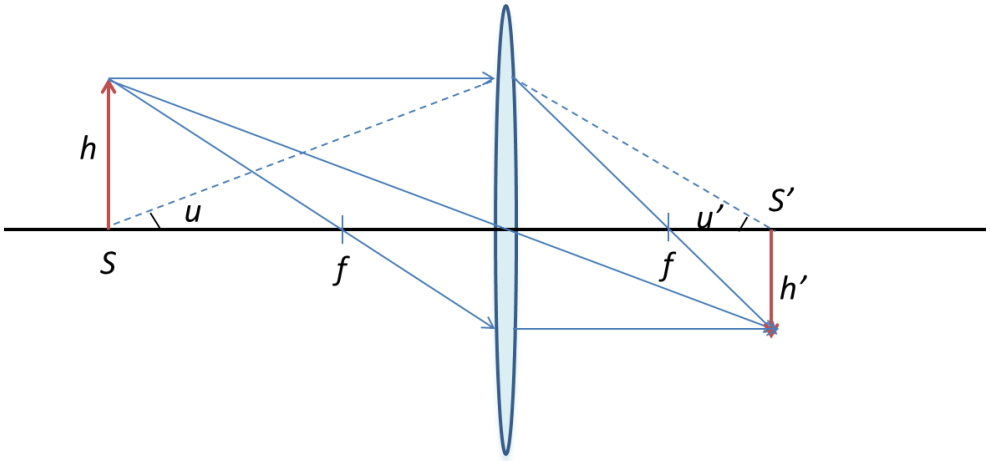

Figure 45. An example of an optical system

Thus, the equation above can be rearranged to give a generalized expression for the magnification of an optical system:

$$m = \frac{h'}{h} = \frac{nu}{n'u'} \tag{39}$$

As the image magnification increases the angular magnification decreases. Therefore the problem of photon loss is caused by the "illumination" being bigger than the entrance slit/aperture of the collimation system. In section 4, the optical system was designed to deliver excitation light and collect luminescence emission generated from implantable sensors. Therefore, this system formed an image of the luminescence spot onto the entrance slit/aperture of the spectrometer. The luminescence spot was generated from the implanted sensor patch and was blurred a lot while travsersing the skin or phantoms. The image size of the luminescence spot is determined by the transverse (lateral) magnification (m), and the output numerical

aperture (NA_{out}) is determined by angular magnification, which is the reciprocal of the transverse magnification ($1/m$). Therefore, the image size decreases as the output numerical aperture increases. However, typically the size and numerical aperture of entrance aperture in a commercial spectrometer is small in order to increase resolution and decrease the effect of aberrations. Because the NA_{in} was already designed to be big enough to capture as much luminescence light as possible, a small image size and small NA_{out} cannot be obtained simultaneously; thus, it is important to recognize that the photon loss at the connection of the optical system and a commercial spectrometer is inevitable.

5.1.3 Rationale of system optimization

The entrance aperture and slit of most current commercial spectrometers are usually small (~hundreds microns) due to the aim of obtaining high spectral resolution and compact structure. The design aiming for high resolution results in decreased signal intensity due to the trade-off between spectral resolution and input energy. The optical system (designed in section 4) for delivery of excitation and collection of emissions can be considered as the illumination part of a spectrometer system as shown in Figure 38. Moreover, for luminescence measurements, only specific, relatively broad bands of the spectrum are of interest. For example (Figure 46), our ratiometric sensors exhibit emission peaks at 585nm (FWHM≈50nm) and 645nm (FWHM≈30nm). Furthermore, luminescent signals collected from tissue or implants will be strongly attenuated by tissue scattering and absorption ($\sim 10^{-4}$); therefore, signal power should take priority over spectral resolution for luminescence. The minimum acceptable resolution is to resolve these two emission peaks.

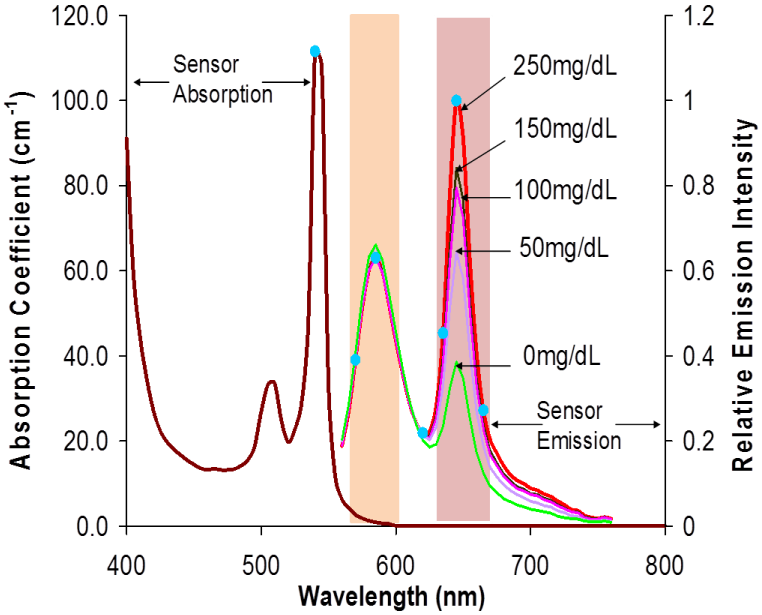

Figure 46. Excitation and emission spectra of sensor particles. For the absorption spectrum shown, [PtOEP] is 10nM. Environmental [glucose] is 250mg/dL. Blue circles and numbers indicate the wavelengths selected for the simulation.

For this application, a more appropriate high-efficiency hardware system that integrates delivery of excitation, collection of luminescence, and measurement of luminescent spectra is needed. It should have high throughput and obtain spectral resolution good enough for our luminescence-based implantable sensors. The aim of this chapter is to investigate system optimization methods to overcome photon loss at the fiber coupling of the designed optical system and a commercial spectrometer.

5.2 Two-detector system

To overcome the photon loss between the fiber coupling of the designed system and a commercial spectrometer, two optimization approaches were investigated. The first approach

was to replace the commercial spectrometer with a two-detector system. The second approach was to replace the commercial spectrometer with a customized spectrometer system, which will be discussed in section 5.3. The design requirements of the system optimization were 1) minimum spectral resolution of 60nm to resolve the two emission peaks at 585nm and 645nm; 2) reduce photon loss at the fiber coupling with the commercial spectrometer. The pros and cons of these two approaches will be discussed in section 5.3.4.

5.2.1 Method of two-detector system

5.2.1.1 System design

Because the luminescence generated from our sensors was broad-banded, and only the reference peak and oxygen sensing peak were used as key information, the spectral information at other wavelength ranges was not critical to the measurement of the sensor response, as long as the two emission peaks could be extracted. Therefore, a two-detector system with a long-pass dichroic mirror was designed to extract the desired spectral information. The dichroic mirror separated the two luminescence emission peaks, and two band-pass filters were used to isolate the two emission peaks of the reference dye (585nm) and the sensing dye (645nm). Emission photons were focused onto photodiode detectors (Figure 47), which also measure the power of the extracted emissions. Figure 47 is a simplified representation of this design.

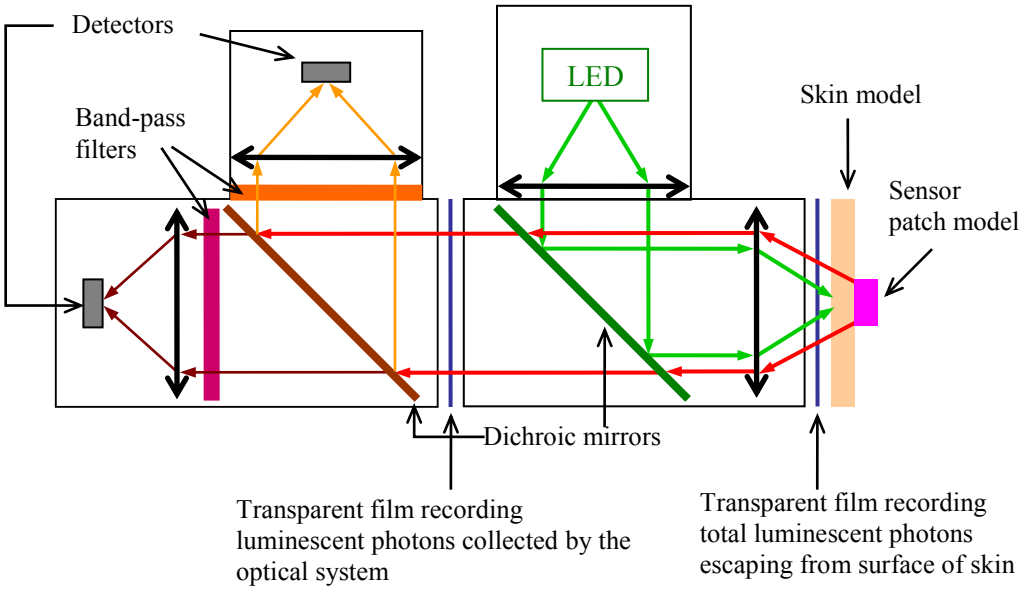

Figure 47. Scheme of two-detector system to extract two emission peaks at 585 and 645nm.

In section 3, the peak ratios of intensities of the emission at 645nm to 585nm and the percentage change in the peak ratios were calculated. The calculations below prove that the percentage change of the intensity of broadband spectra is still proportional to the concentration of glucose. Because the intensity of light source or the environment may change over time, time (t) is used in calculation. Here, $I_{ref}(585, t)$ is the emission intensity of the reference dye at a single wavelength (585nm), and $\sum I_{ref}(\lambda, t)$is the sum of emission intensities of reference dye within a broadband spectrum (λ was the wavelength, and t was the time), and since the reference emission was stable in various glucose concentrations, $I_{ref}(585, t)$ and $\sum I_{ref}(\lambda, t)$ were irrelevant to glucose concentrations (C). $I_{sen}(645, C, t)$ is the emission intensity of the sensing dye at a single wavelength (645nm), and $\sum I_{sen}(\lambda, C, t)$ is the sum of the emission intensities of the sensing dye

in a broadband. Because theoretically [29, 30], the $I_{sen}(\lambda, C, t)$is linearly correlated to glucose concentration (C) in linear operation range, there is a linear relationship:

$$I_{sen}(\lambda, C, t) = C \cdot k(\lambda, t) + m(\lambda, t) \tag{40}$$

Therefore, the percentage change of ratios of emission intensity at 645nm to that at 585nm should be linearly correlated to glucose concentration, which is shown in the following equations, where t_0 is the time when environmental glucose concentration is zero.

$$\%change(C, t) = \frac{I_{sen}(645, C, t)/I_{ref}(585, t)}{I_{sen}(645,0, t_0)/I_{ref}(585, t_0)} - 1$$

$$= \frac{[C \cdot k(645, t) + m(645, t)]/I_{ref}(585, t)}{m(645, t_0)/I_{ref}(585, t_0)} - 1$$

Thus,

$$\%change = \frac{[C \cdot k(645, t) + m(645, t)] \cdot I_{ref}(585, t)}{m(645, t_0) \cdot I_{ref}(585, t_0)} - 1 \quad \propto C \tag{41}$$

Because

$$\sum_a^b I_{sen}(\lambda, C, t) = \sum_a^b [C \cdot k(\lambda, t) + m(\lambda, t)] \tag{42}$$

$$\therefore = C \cdot \sum_a^b k(\lambda, t) + \sum_a^b m(\lambda, t) \quad \propto C$$

$$\%change(C, t) = \frac{\sum_a^b I_{sen}(\lambda, C, t)/\sum_c^d I_{ref}(\lambda, t)}{\sum_a^b I_{sen}(\lambda, 0, t_0) / \sum_c^d I_{ref}(\lambda, t_0)} - 1$$

$$\therefore \%change(C, t) = \frac{C \cdot \sum_a^b k(\lambda, t) + \sum_a^b m(\lambda, t)}{\sum_a^b m(\lambda, t_0)} \cdot \frac{\sum_c^d I_{ref}(\lambda, t)}{\sum_c^d I_{ref}(\lambda, t_0)} - 1 \tag{43}$$

which still has a linear relationship with glucose concentration (C).

In the equations above, $[a, b]$ and $[c, d]$ are the wavelength ranges of the band-pass filters extracting the spectra of emission from the sensing dye and the reference dye, respectively. $I_{sen}(\lambda, 0, t_0)$ is the baseline when the glucose concentration is zero. From the equations above, we can see that the percentage changes maintain a linear relationship with the glucose concentrations when the broad-banded spectra were extracted.

According to Equation 43, the linearity (R-squares) were not affected by the wavelength ranges theoretically, since the percentage change is theoretically linearly related glucose concentration. The sensitivities (slope of percentage change versus glucose concentrations) were relevant to the wavelength range ($[a,b]$) according to the following equations.

$$slope = \frac{\sum_{a\ll\lambda\ll b} k(\lambda, t)}{\sum_{a\ll\lambda\ll b} m(\lambda, t_0)} \cdot \frac{\sum_{c\ll\lambda\ll d} I_{ref}(\lambda, t)}{\sum_{c\ll\lambda\ll d} I_{ref}(\lambda, t_0)} \tag{44}$$

Where, t_0 is the time when glucose concentration is zero.

Regardless the signal drifting with time, thus:

$$\frac{\sum_{c\ll\lambda\ll d} I_{ref}(\lambda, t)}{\sum_{c\ll\lambda\ll d} I_{ref}(\lambda, t_0)} \approx 1 \tag{45}$$

After averaging the data over time:

$$\therefore slope \approx \frac{\sum_{a\ll\lambda\ll b} k(\lambda, t)}{\sum_{a\ll\lambda\ll b} m(\lambda, t_0)} \approx \frac{\sum_{a\ll\lambda\ll b} k(\lambda, t)}{\sum_{a\ll\lambda\ll b} m(\lambda, t)} \tag{46}$$

5.2.1.2 Selection of filters

To determine suitable wavelength ranges of the band-pass filters ($[a, b]$ and $[c, d]$ as shown in Figure 48), calculations were performed with MATLAB. Because the sensitivity (slope) and linearity (R-square) are the factors relevant to the performance of sensors, the goal of optimization is to maximize the sensitivity (slope) and linearity within the wavelength ranges

that still maintain enough intensity for experimental measurement. According to Equation 43, the percentage change is theoretically linearly related to glucose concentration, thus linearity is not relevant to wavelength range. In Figure 48, the lower boundary of wavelength range of sensing dye is around 610nm, thus the upper boundary (d) of the wavelength range ([c, d]) of reference dye need to be smaller than 610nm. To avoid the overlap of wavelength range of excitation light source, the lower boundary (c) of the wavelength range need to be bigger than 550nm, if a band-pass green excitation filter with FWHM of 10nm at 530nm is used. In order to maximize the emission intensity over ([c, d]) and minimize the interference from light source and emission of sensing dye, the wavelength range ([c, d]) was determined to be 550 – 610nm, thus the FWHM of emission filter for the reference dye can be 560-600nm.

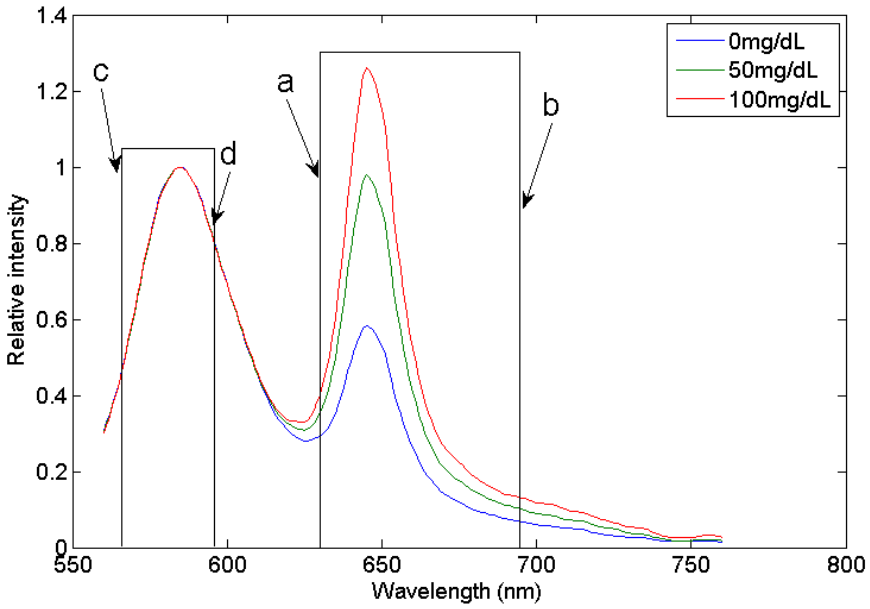

Figure 48. Relative intensity of emission. Legend is glucose concentrations.

The k(λ, t) and m(λ, t) were calculated using MATLAB and are shown in Figure 49 and 50, respectively, so from the figures, it can been seen that k(λ, t) and m(λ, t) change over λ

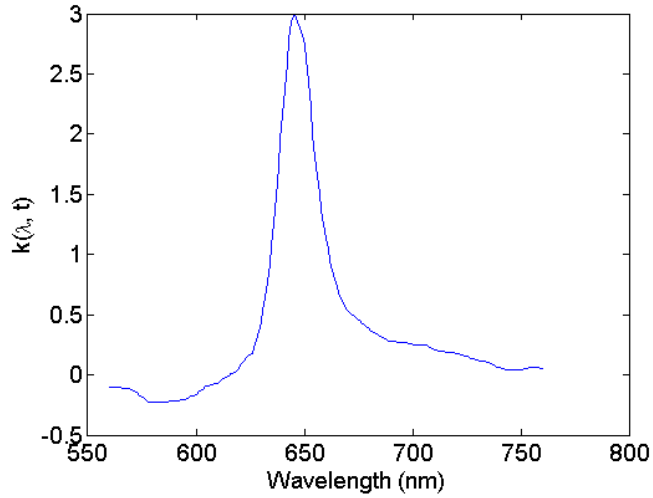

Figure 49. k(λ, t) over λ

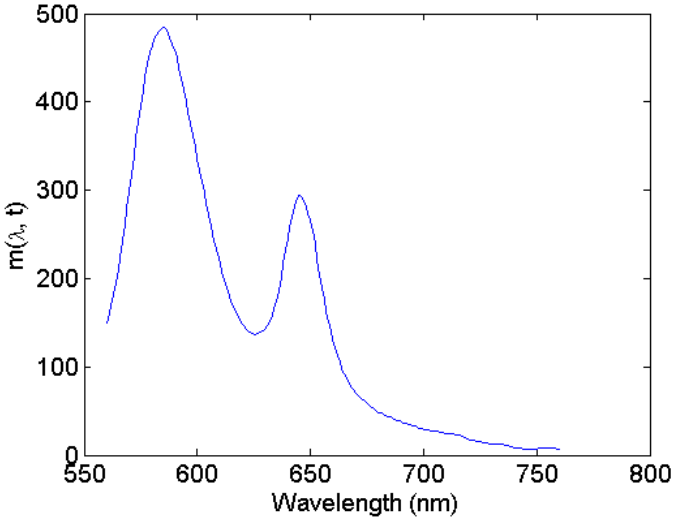

Figure 50. m(λ, t) over λ

Figure 51 is a plot of the calculated slopes of percentage changes versus glucose concentrations, which is the ratio of $\sum k(\lambda, t)$ to $\sum m(\lambda, t)$ over $\lambda \in [a, b]$. In Figure 51, the slopes (sensitivities of the response to glucose) increase until "a" reaches 650nm. However, the sum of the emission intensities $\sum I_{sen}(\lambda, C, t)$ (Figure 52) decreases as "a" increases (Figure 48). Therefore, "a" needs to be a wavelength that balances the sensitivity and the intensity. The lower boundary of the emission of sensing dye is 610nm, thus lower boundary (*a*) can be around 630±5nm, and upper boundary (*b*) can be any wavelength longer than 650nm.

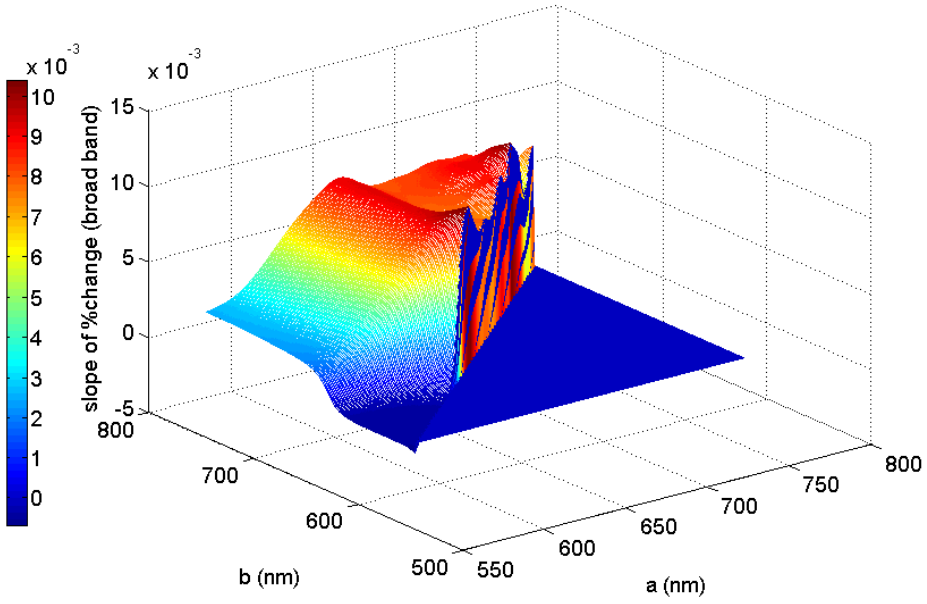

Figure 51. Slope of percentage changes

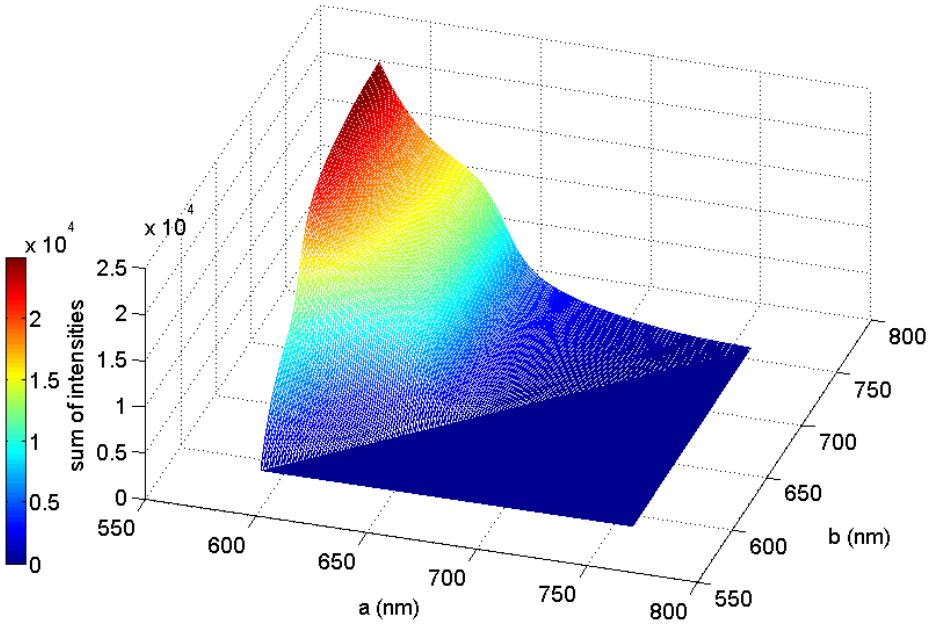

Figure 52. Sum of intensities of emission from sensing dye.

5.2.1.3 Selection of detectors

The criteria of the selection detectors of the two-detector system are 1) sensitive enough to respond the light on the order of 10nW (Given the attainable excitation light input is 1mW, and the output is on the order of 10nW after going through a ~1mm thick skin phantom estimated from the equation in Figure 19); 2) proper wavelength range (500-700nm); 3) active area big enough (bigger than the size of the focusing spot that is 2mm in diameter); 4) compact; 5) low-cost; 6) easy to mount.

For the required sensitivity, wavelength range and cost, silicon photodiodes are selected, because GaP photodiodes cannot attain the required sensitivity, Ge photodiodes are not for the visible wavelength range but for NIR wavelength range, and InGaAs photodiodes are costly

compared with silicon devices. As the active area needs to be bigger than 2mm in diameter, the photodiode DET110 (Thorlab) was chosen, because it has active area as 13mm^2 (3.6mm×3.6mm) , which matches the focusing spot size. Moreover, this photodiode is already mounted on a 1-inch optical coupler, which provides easy mounting of 1-inch optics and lens tubes. Below is the specification (Table 6 and Figure 53) of this photodiode.

Table 6. Specifications of DET110 from Thorlabs.

Detector:	Silicon PIN	**Housing:**	Black Anodized Aluminum
Spectral Response:	350-1100nm	**Size:**	ϕ1.43" x 1.67"
Peak Wavelength:	960nm+/-50nm	**Output:**	BNC, DC-Coupled
Rise/Fall Time[1]:	20ns	**Bias:**	12V Battery (Type A23)
Diode Capacitance:	20pF	**Mounting:**	8-32 (M4) Tapped Hole
NEP:	1.2 x 10^{-14}W/√HZ	**Diode Socket:**	TO-5, Anode Marked
Dark Current:	10nA	**Damage Threshold:**	100mW CW
Active Area:	13mm^2 3.6mm x 3.6mm square		0.5 J/cm^2 (10ns pulse)
Linearity Limit:	1mW		

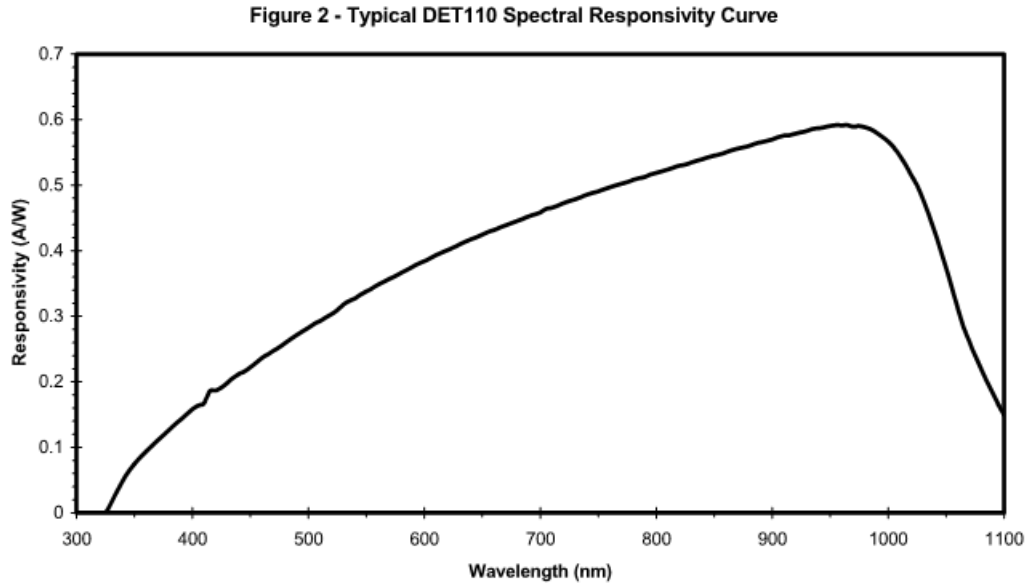

Figure 53. Spectral responsivity of DET110.

5.2.1.4 *In vitro* experimental evaluation of the two-detector system

After selection of the components of filters, dichroic mirror, and the detectors, the prototype of the two-detector system was constructed. The experimental evaluation of the system was then performed both without a phantom, as well as with three phantoms of different thicknesses: 0.44, 0.65 and 2.3mm. Each measurement was repeated 10 times to calculate the signal to noise ratio (SNR). The LED light source (LS-30, Sandhouse, Dunedin, Florida, λ_{peak}=530nm) was turned on for 20min before starting any measurement. The sensor patch was attached onto a glass slide with double-sided sticky tape, and then was covered by the phantoms.

5.2.2 Results of the system design

Figure 54 is a diagram of the final two-detector system. A long-pass dichroic mirror (at 610nm) split the luminescence emission at 610nm, and two band pass filters (580±20nm and 645±20nm) were used to extract two emission peaks of reference dye (585nm) and indicating dye (645nm). Lenses before detectors focus light onto sensitive areas on detectors.

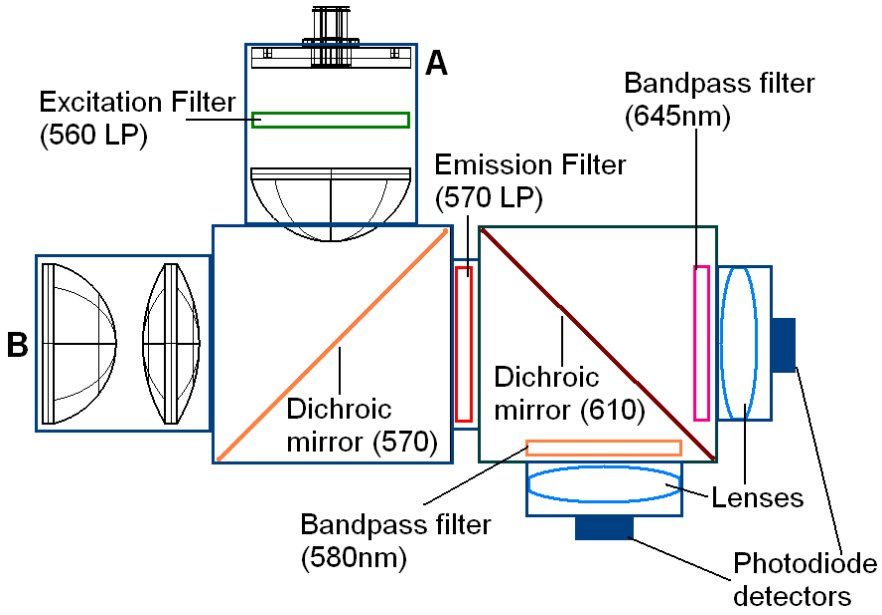

Figure 54. Diagram of optimized two-detector system.

5.2.3 Results of experimental evaluation of the two detector system

The two-detector system was constructed as shown in Figure 55. The 570nm long pass dichroic mirror is from Omega, and the 610nm long pass dichroic mirror is from Chroma Technology Corp. The two band pass filters (Chroma Technology Corp) are 580±20nm and 645±20nm. The two photodiode detectors (DET110, Thorlabs) have spectral response range from 350 to 1100nm, and active area of 13mm^2, and linearity limit of 1mW. A highly-scattering skin phantom was used to cover a sensor patch mobilized on a glass slide. Ten measurements were made for each phantom. In Figure 56, emission peak ratios were the ratios of two current signals from detectors. As shown, SNR decreased from 450 to 81 with phantom thickness increasing from 0.44mm to 2.3mm. However, 2.3mm is thicker than average dermis [62], thus for sensors implanted in dermis, these results indicate that this system will be high SNR for *in vivo* measurement. The detectable thickness of phantom using fiber bundle and the commercial spectrometer we used before were around 0.5~1mm depending on the concentration of the sensors, thus the detectable thickness using the two-detector system was 1.3 thicker than that of fiber bundle. The two-detector system is straightforward to design and construct; however, a given conformation is only useful for a typical emission pair (585nm and 645nm). Filters and dichroic mirrors must be specified for each type of sensor, so if the emission peaks are changed for different sensors, all filters and dichroic mirrors need to be changed accordingly.

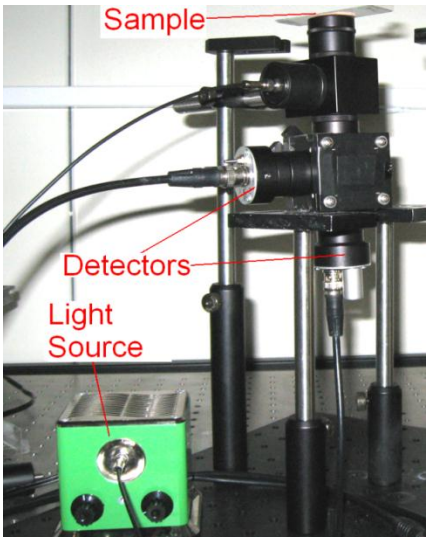

Figure 55. picture of two-detector system

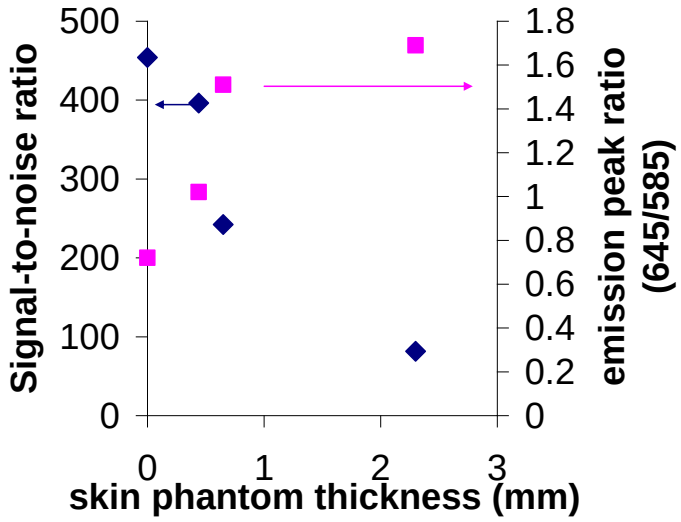

Figure 56. Signal-to-noise ratio and emission peak ratio versus skin phantom thickness.

5.3 Customized spectrometer

The approach of replacing the commercial spectrometer with a customized spectrometer was studied as an alternative to the two-detector system. The pros and cons of these two approaches would be discussed later.

5.3.1 Method of system design

The key to customizing the spectrometer was to find a proper entrance aperture of the spectrometer system that allowed as much light input as possible into spectroscopic system while maintaining sufficient spectral resolution for our luminescent sensors (minimal: 60nm). As long as the system can resolve the emission peaks of the reference and sensing dyes respectively, the spectral resolution is good enough. Therefore, theoretical analysis was performed to understand the key factors and the design of a suitable system. Following the standard spectrometer design, Figure 57 shows the scheme of the system integrating the functions of excitation delivery, luminescence collection and spectrum measurement.

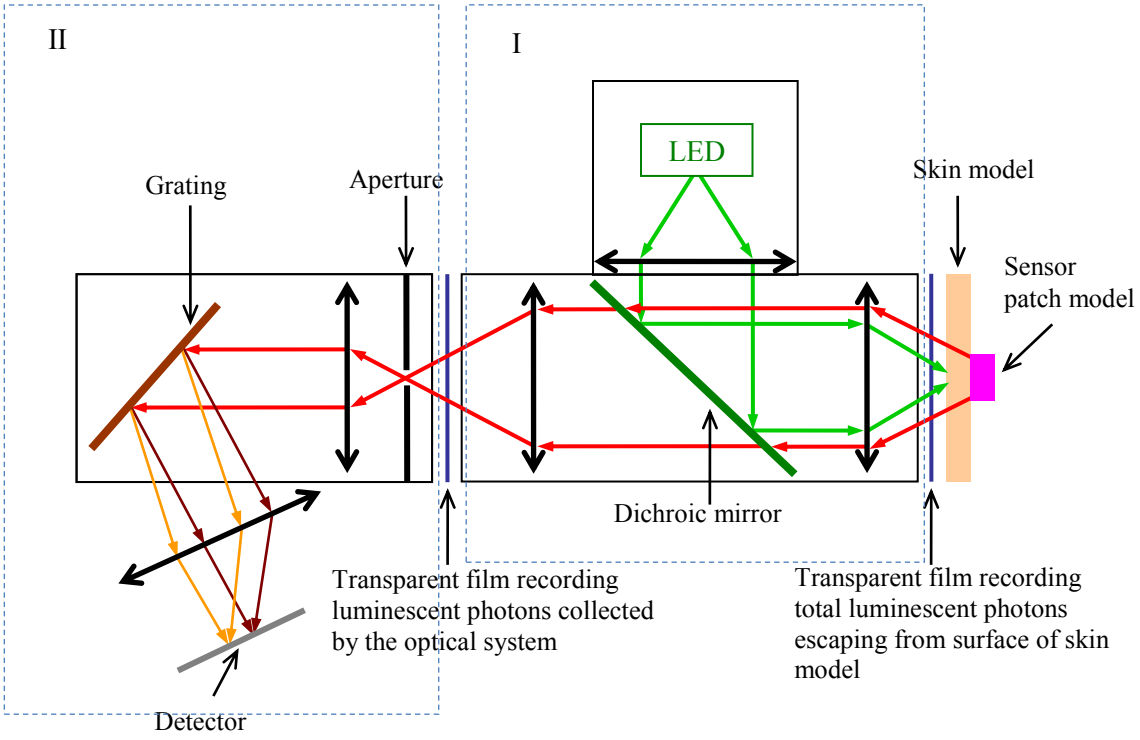

Figure 57. Scheme of optimized system integrating delivery of excitation light, collection of luminescent light, and spectrum measurement.

Part I is the optical system to deliver excitation and collect emission light designed in section 4. Part II is the layout of the customized spectrometer. The detected spectral intensity was recorded on the detector film (in simulations) in Figure 57. The image size could be controlled by aperture size, which also controlled the throughput. While aiming to achieve the minimal spectral resolution of 60nm, the aperture size, collection lenses and detector size would be optimized to optimize the system throughput, and the lenses also would be optimized to reduce system aberrations in order to optimize the system bandpass.

Figure 57 shows that the luminescence light escaping from skin (phantom) was collected by Part I, and it was imaged onto the entrance aperture plane on Part II. Also in Part II, the luminescence light was collimated, dispersed and finally focused onto the detector plane. Luminescence light that originated from the input focal plane of the optical system went through collimation, focusing, and again, collimation, and focusing. In reviewing this optical layout, a new possibility was conceived: it should be possible to relocate the aperture/slit from Part II to a place as depicted in Figure 58 next to the sensor/tissue. In this case, the two additional focusing/collimating lenses are not needed. To investigate the effect of the position of the aperture, additional simulations were performed to compare the photons collected by the detectors.

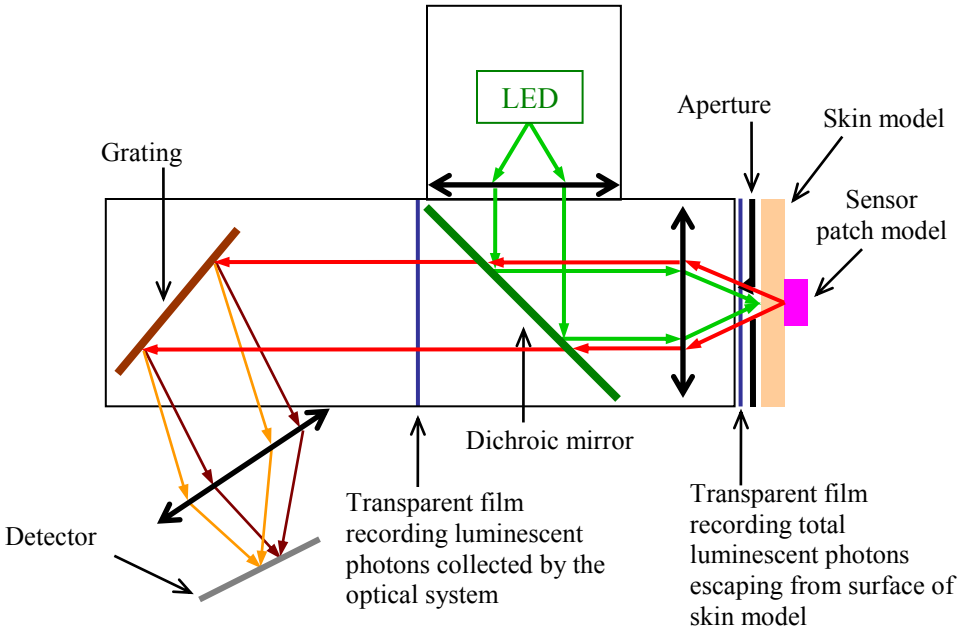

Figure 58. Scheme of the optimization system with slit placed in front of the skin/phantom.

The simulations for comparison these two designs (Figure 57 and Figure 58) were run with OptiCAD. The Simulation-I (Figure 59) was for the design depicted in Figure 57, and simulation-II was for the design depicted in Figure 58. In both groups of simulations, the power of the input excitation light was normalized to 1.

Simulation-I: the luminescence light was passing through slit 1 (Figure 59), and slit 1 was positioned on the focal plane of the focusing part in the middle of Figure 59. The luminescence was focused onto slit 1, was collimated, was dispersed by the grating, and finally was focused onto the detector. The lenses for “collecting”, “focusing”, and “collimating” luminescence are the same, and the lenses for “focusing” and “collimating” have a symmetric

configuration, because this configuration has minimal spherical aberrations and the highest throughput. A focusing mirror was chosen instead of lenses, because it introduces zero chromatic aberrations.

Simulation-II: the slit used to define the entrance aperture of the system, was positioned right in front of the skin/phantom as slit 2 in Figure 59. The grating, focusing mirror and detector were also moved towards the dichroic mirror.

In both groups of simulations, the widths of slits considered were 0.6, 1, 1.4, 2mm. Three phantom models with different thicknesses (268, 576, 1010μm) were used in simulations to simulate the capability of these systems when a phantom was placed on the sensors. The photon capture films depicted in Figure 59 were used to collect collimated luminescence in both simulation-I and II, and the photon distributions on these two films were analyzed to compare these two designs. The simulations were performed both without phantom models and with the phantom models of three different thicknesses (268, 576, and 1010μm).

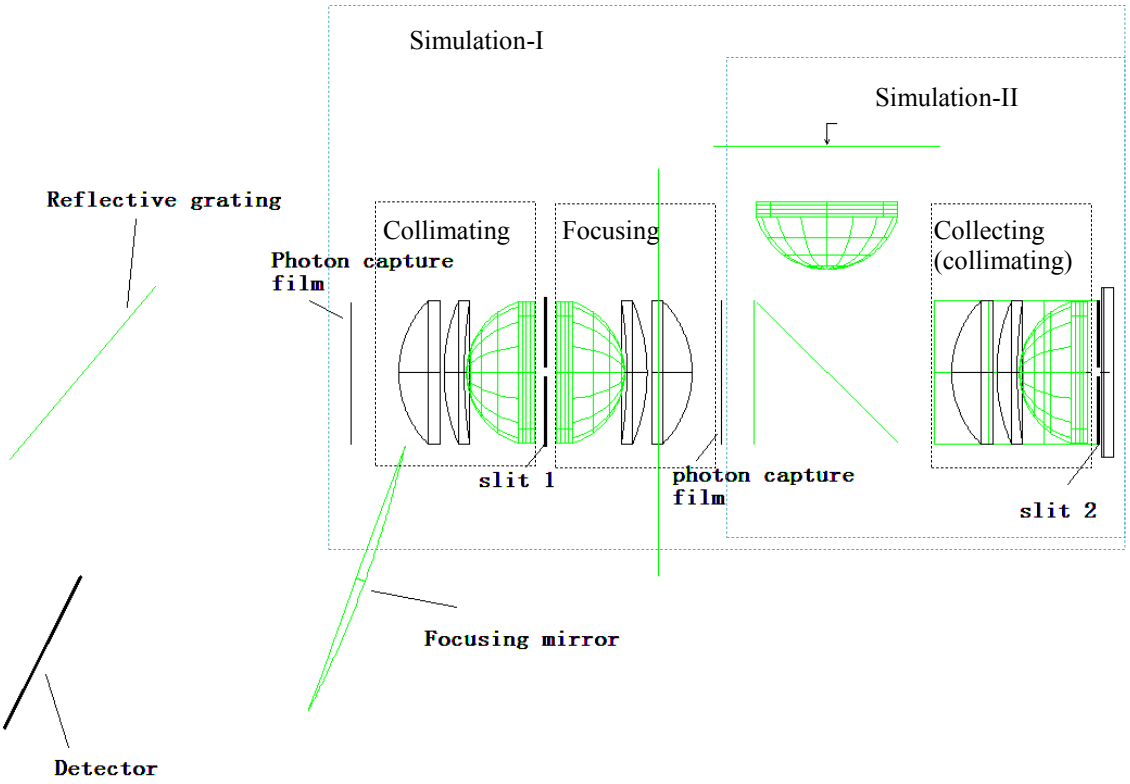

Figure 59. Scheme of simulation system for optimization

5.3.1.1 Selection of dispersing components

After the optimization of the structure of the system, the specific components such as grating and detectors need to be determined. Although diffraction gratings do not provide a transmission as high as dispersion prisms, the dispersive angle is bigger than that of most prisms, thus it can enable a more compact setup. Moreover, the absolute efficiency of a diffractive grating can be more than 60% which is acceptable in practice. Among the diffraction gratings, there are four common types, and these are reflective ruled gratings, holographic gratings, echelle gratings and transmission gratings. Echelle gratings are special low period gratings designed for use in high

orders. They are generally used for high resolution spectroscopy. Because high resolution is not necessary for this system, it is not necessary to choose a more expensive Echelle grating. Transmission grating cannot enable a compact system without adding extra mirrors, which may make the system more bulky. Holographic gratings do not suffer from periodic errors, thus ghosted images are nonexistent. They are suitable in applications such as Raman spectroscopy, where the signal to noise ratio is an essential concern. Reflective ruled grating typically can achieve higher efficiency than holographic gratings due to their blaze angles [154]. Taking all pros and cons into consideration, the reflective ruled gratings was chosen, because it is more efficient than holographic gratings, less expensive than Echelle and holographic gratings, and it can allow a more compact system build.

The luminescence emission of our sensors is in the range of 550~800nm. Among commercially available reflective ruled gratings, there is one blazed wavelength 750nm within this range. Figure 60(a) and (b) contain the plots of the absolute efficiency of two gratings blazed at 750nm and with 600 and 1200 grooves/mm obtained from www.thorlabs.com. The 600-groove grating has blaze angle of 13º and 1200-groove grating has a 26.44º blaze angle. The gratings yield an improvement in performance as the angle of incidence tends toward the blaze angle, since the efficiency curve tends towards the efficiency of Littrow configuration. However, in practice we cannot usually permit this configuration since the diffracted field will be in the vicinity of the incident field. [155] Thus, in order to have the difference between the angle of incident beam and the blazed angle as small as possible, a grating of a larger blazed angle (26.44º) is a superior option. Considering the size of the incident beam, a 30x30mm square grating blazed at 750nm with 1200 grooves/mm was chosen.

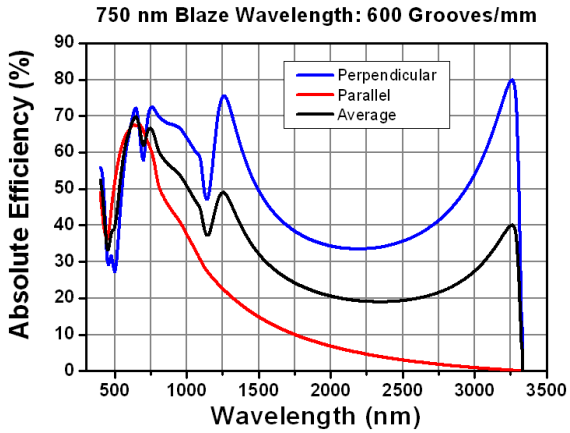

(a)

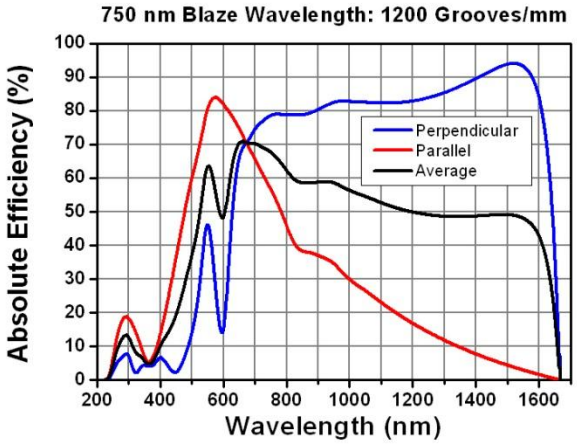

(b)

Figure 60. Absolute efficiency of gratings blazed at 750nm. (a) 600 grooves/mm. (b) 1200 grooves/mm[156]

5.3.1.2 Selection of detector arrays

The detector array of a spectrometer is, besides the grating, the main component in the system. There are three types of detector arrays used in spectrometers: CCD, photodiode and CMOS arrays. The main parameters taken into considering are as below. [157]

1) Pixel number – the number of pixels arranged in the line

2) Pixel dimensions – the pixel width and height

3) Pixel pitch - the distance between the center of two pixels

4) Sensitivity (v/lx*s) – the wavelength dependent ratio of electrical signal output to the optical signal input. Sensitivity is one of the most important factors to the sensor system, because the detector needs to be able to detect weak signal which was attenuated by skin. Thus, the sensitivity of detector needs to be ~10-100v/lx*s for our sensor system (the fluorescent from 1.7mm is estimated to be around 1E-5~7E-4 lx which depends on the concentration of particles, the dye concentration, quantum yield, and the intensity of the excitation light.).

5) Wavelength range – the range of wavelengths where the detector can detect the radiation. Wavelength range needs to match the wavelength range of sensor emission (560~660nm).

6) Dark signal – the output signal without illumination

7) Saturation exposure – the illumination level at which the output signal stays constant with increasing the luminance.

8) Linearity range – the luminance range where the electrical signal output is proportional to the impinging energy. Linearity is critical to the system as well, because the operation range of the sensor system depends on the response linearity of the sensors and detectors. The whole sensor system will be affected less if the detector has better linearity.

9) Dynamic range – the range in which the detector is capable of accurately measuring the input signal. It is one of the most critical factors to the sensor system. According to the

simulation results showed in Figure 19, the relationship of ratios of output intensity to that of input and implantation depth(μm) is: y = 0.013exp(-0.0045x), thus varying the implantation depth within the range of 400~1700μm that is the range of dermis, the output signal from the depth of 400μm is 347 times more than that from the depth of 1700μm. Since the intensity of the output signal depends on the implantation depths, and varies around 300, that a detector needs to be of a dynamic range more than 300.

10) Pixel non-uniformity – the output signal difference of the pixels under same illumination conditions [%].

A CCD (charge-coupled device) is a device for the movement of electrical charge, usually from within the device to an area where the charge can be manipulated. The photoactive region is metal-oxide capacitors (gate electrode). During the illumination by the spectrum focal line, a charge (electron-hole pairs) is produced under the gate. A potential well is created by applying a voltage to the gate electrode. The charge is confined in the potential well associated with each pixel by the surrounding zones of higher potential (see detail in Figure 61). A control circuit drives each capacitors to transfer the charge to its neighbor (operating as a shift register). The last capacitor in the array dumps its charge in to a charge amplifier, which converts the charge into a voltage. By repeating this process, the control circuit converts all of the charges of the pixels into a sequence of voltages. [158]

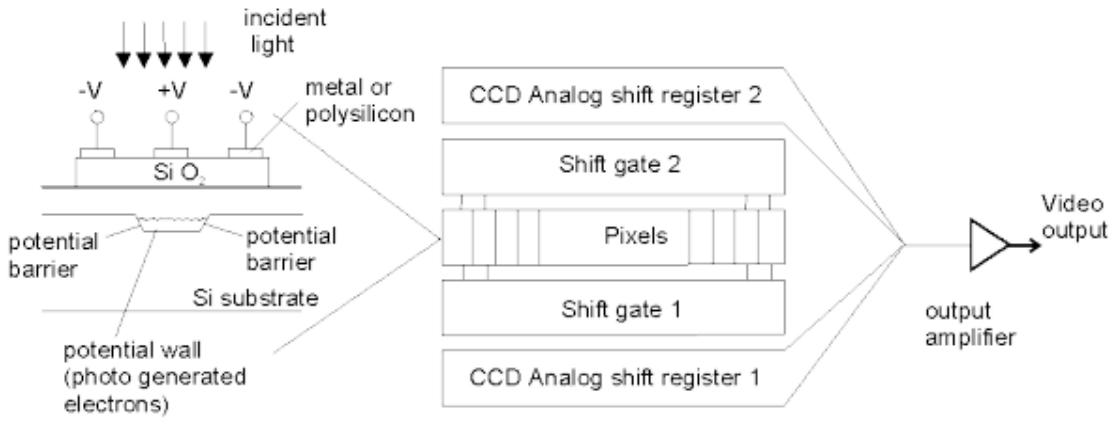

Figure 61. Operation principle of a CCD array [157]

A photodiode is a type of photo-detector which is capable of converting light into an electric signal (either current or voltage). A photodiode is a p-n junction or PIN structure. When a photon of sufficient energy impingings the diode, it excites an electron, thus creating a free electron and a positively charged electron hole (photoelectric effect). If the photon absorption occurs in the junction's depletion region, these carriers are swept from the junction by the built-in field of the depletion region. Thus, electron holes move toward the anode, and electrons move toward cathode, and thus a current is produced. The total current is the sum of both the dark current and the light current. 1-D photodiode arrays consist of several photodiodes (pixels) arranged in a line. The current generated by photon absorption is integrated by an integration circuitry associated with this pixel. During a sampling period the sampling capacitor connects to the output of the integrator through an analog switch. Figure 62 is the operation scheme of a photodiode array. [157, 159]

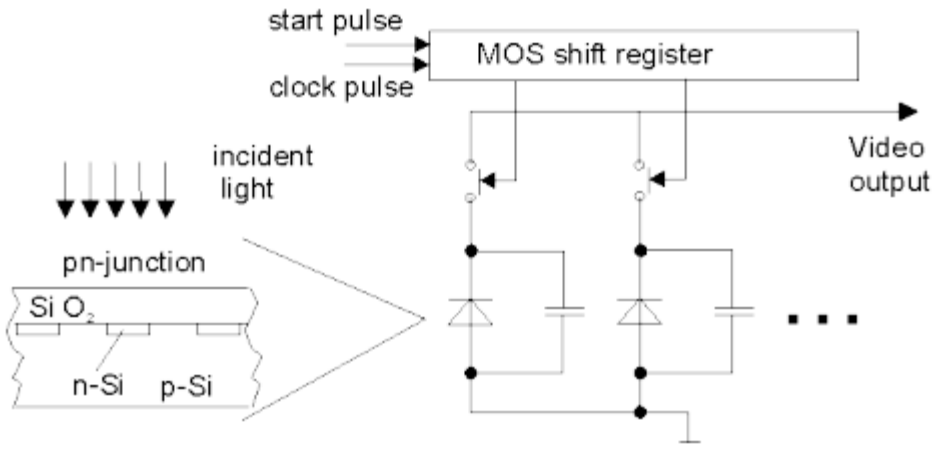

Figure 62. Operation principle of photodiode arrays [157]

CMOS (complementary metal-oxide-semiconductor) arrays also use MOS (metal-oxide-semiconductor) structures as pixels like the CCD arrays. The basic difference is that the charge-to-voltage conversion takes place directly in the pixel cell, while CCD transfers the charge of each pixel to the next pixel until the last one, and converts the charge into voltage. The photon-voltage conversion of CMOS arrays consists of two steps. The photon is converted to electron, and then the charge (electron) is converted to voltage. Figure 63 shows the scheme of a CMOS line array. [157, 160]

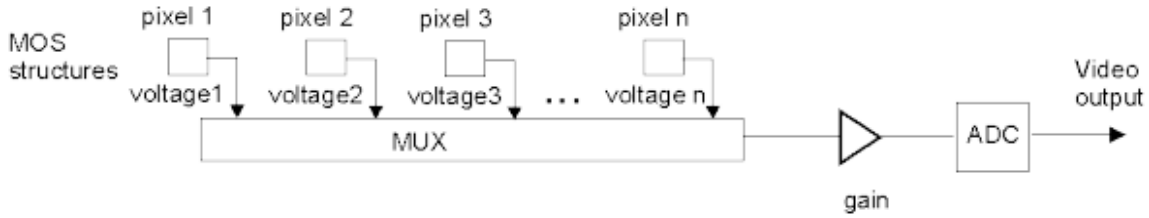

Figure 63. Operation principle of CMOS arrays. [157]

Other detectors such as APD (Avalanche Photodiode) and PMT (Photomultiplier) are more expensive than the detectors discussed above. PMT requires external high voltage supply, which will also make the system more bulky.

The detectable wavelength range of silicon-based detector arrays extends from 200 to 1100 nm, because wavelengths longer than 1100nm have lower photon energy lower than the band gap energy. For the application of our luminescence sensors, which emit from 550-800nm, any silicon-based detector arrays satisfies this wavelength range. Table 7 below is the comparison of feature and performance between CCD and CMOS. From Table 7, it is clear that each technique has pros and cons, thus the choice was mainly dependent on the types of applications. Because the luminescent signal we want to detect is weak and eve attenuated by skin, we want a detector has small noise. The luminescent signal varied a lot versus the implantation depth, thus the detector needs to have a good dynamic range. Because the system noise of CCD is relatively lower than that of CMOS, and the dynamic range of CCD is better than CMOS, the choice of detectors was among different types of CCD arrays.

Table 7. Feature and performance comparison [161]

Feature	CCD	CMOS
Signal out of pixel	Electron packet	Voltage
Signal out of chip	Voltage (analog)	Bits (digital)
Signal out of camera	Bits (digital)	Bits (digital)
Fill factor	High	Moderate
Amplifier mismatch	N/A	Moderate
System Noise	Low	Moderate
System Complexity	High	Low
Sensor Complexity	Low	High
Camera components	Sensor + multiple support chips + lens	Sensor + lens possible, but additional support chips common
Relative R&D cost	Lower	Higher
Relative system cost	Depends on Application	Depends on Application
Performance	CCD	CMOS
Responsivity	Moderate	Slightly better
Dynamic Range	High	Moderate
Uniformity	High	Low to Moderate
Uniform Shuttering	Fast, common	Poor
Uniformity	High	Low to Moderate
Speed	Moderate to High	Higher
Windowing	Limited	Extensive
Antiblooming	High to none	High
Biasing and Clocking	Multiple, higher voltage	Single, low-voltage

Other than wavelength range, the sensitivity, pixel dimension, and dynamic range take priority affecting detector selections, because these three factors are relevant to the detection limitation, image size, and image power. Another factor is cost, since the whole system is aimed to be cost-effective. Considering all key parameters, the SONY IXL511 (specifications were shown in Table 8 and Figure 64) and Toshiba TCD1304AP (specifications were shown in Table 9 and Figure 65) linear CCD-array devices were chosen as they are of good sensitivity around 160-200v/(lx*s), acceptable dynamic range which is around 300, and pixel size is 8μm×200μm, and it is not expensive. Since a control PCB board for TCD1304AP was directly available, the

electric circuit design was not required for TCD1304AP, thus the TCD1304AP was chosen to most expeditiously construct a custom spectrometer.

Table 8. Optical and electrical characteristics of SONY IXL511

Item	Symbol	Min.	Typ.	Max.	Unit	Remarks
Sensitivity 1	R1	150	200	250	V/(lx • s)	Note 1
Sensitivity 2	R2	—	1800	—	V/(lx • s)	Note 2
Sensitivity nonuniformity	PRNU	—	5.0	10.0	%	Note 3
Saturation output voltage	VSAT	0.6	0.8	—	V	—
Dark voltage average	VDRK	—	3.0	6.0	mV	Note 4
Dark signal nonuniformity	DSNU	—	6.0	12.0	mV	Note 4
Image lag	IL	—	1	—	%	Note 5
Dynamic range	DR	—	267	—	—	Note 6
Saturation exposure	SE	—	0.004	—	lx • s	Note 7
5V current consumption	I VDD	—	5.0	10.0	mA	—
Total transfer efficiency	TTE	92.0	98.0	—	%	—
Output impedance	ZO	—	250	—	Ω	—
Offset level	VOS	—	2.8	—	V	Note 8

Table 9. Optical and electrical characteristics of TCD1304AP

CHARACTERISTIC	SYMBOL	MIN	TYP.	MAX	UNIT
Sensitivity	R	110	160	—	V / lx·s
Photo Response Non Uniformity	PRNU	—	—	10	%
Register Imbalance	RI	—	—	3	%
Saturation Output Voltage	V_{SAT}	450	600	—	mV
Dark Signal Voltage	V_{MDK}	—	2	5	mV
Total Transfer Effeiciency	TTE	92	95	—	%
Dynamic Range	DR	—	300	—	—
Saturation Exposure	SE	—	0.004	—	lx·s
DC Power Dissipation	PD	—	25	75	mW
DC Signal Output Voltage	V_{OS}	1.5	2.5	3.5	V
Output Impedance	Z_o	—	0.5	1.0	kΩ
Image Lag of Electronic Shutter	VLAGICG	—	—	10	mV

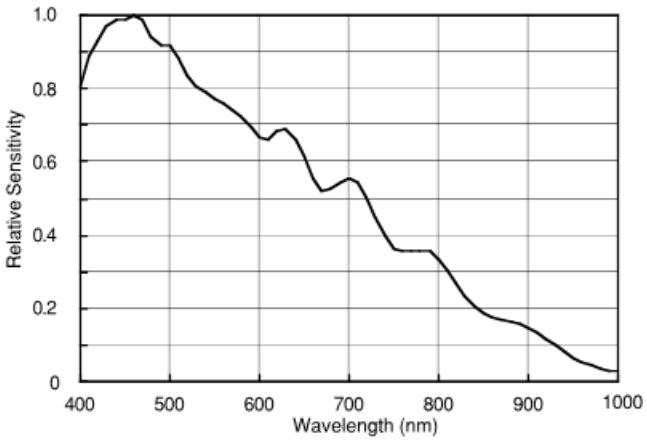

Figure 64. Spectral response of SONY IXL511.

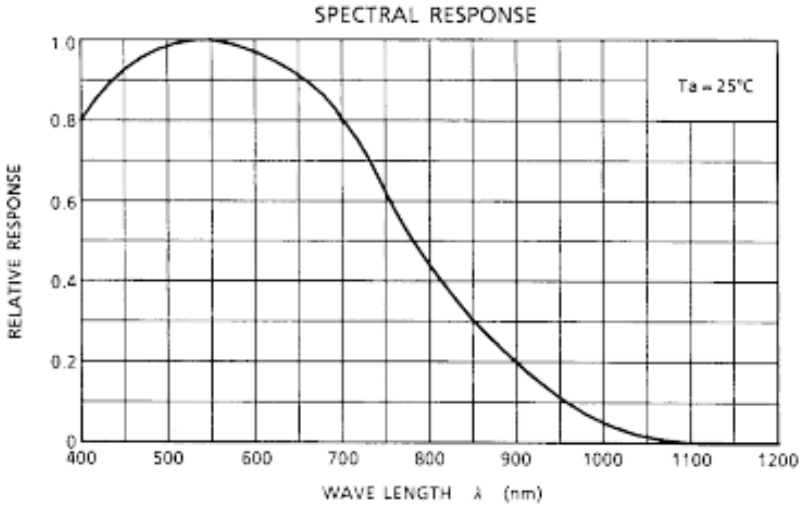

Figure 65. Spectral response of TCD1340AP

The prototype system was assembled on an optical breadboard for initial evaluation. The control circuit was a PCB mother-board of an Ocean Optics USB4000/2000 spectrometer (purchased from Ebay). The excitation light power input into the system was 17.2μw, and

filtered by a band-pass filter (530±10nm). Optical posts were used for fixing the optics in the prototype system. This is not as compact as desired, but the future work on further miniaturizing the system after all optical evaluations are completed to prove specifications are met.

5.3.1.3 Experimental evaluation of the customized spectrometer system

Experimental evaluations were performed by comparing the designed system to the bifurcated fiber bundle system previously used for in vitro and in vivo studies (NA=0.22, core=200μm, 37 excitation fibers and 41 emission fibers). The skin phantoms with different thicknesses were used for experimental evaluation. Samples were the RITC, and the mixture of PtOEP and RITC solutions. A PDMS mold with a 5mm diameter hole was immobilized on a plastic petri-dish with a double-sided tape, and the sample solutions were poured into the mold. The phantoms were attached to the bottom of the petri dishes, and the excitation light was directed onto the phantoms. Two light sources (580±20nm and 645±20nm) were also used as calibration light sources. Ocean Optics USB4000 was used to collect spectra of the bifurcated fiber bundle. The excitation light (input=17μW) with a band-pass filter (530±10nm). Integration time varied from 1ms to 500ms, and average of spectra was 2, and the number of boxcar smoothing was 15.

5.3.2 Results of the system design

Figures 66 - 68 contain the results of simulation-1 and simulation-II depicted in Figure 59. The solid lines are the results of simulation-I which simulated the slit positioned in the focal plane of focusing lenses. The solid circles are results of simulation-II which simulated the slit positioned right in front of the skin phantoms. In the legend, 0.6 (I), 1.0 (I), 1.4 (I) and 2.0 (I) represent the simulated results when the slit width =0.6, 1, 1.4, and 2mm in simulation (I) that was described previously; and 0.6 (II), 1.0 (II), 1.4 (II), 2.0 (II) represent the simulated results in simulation-II.

Figure 66 (a)-(d) are the intensity of luminescence photons captured on the photon capture film (Figure 59) versus the angles between the photons impinging on the film and the normal of the film. As shown in Figure 66, there are more photons with smaller incident angles as the slit is near the skin phantom when there is no skin model, with a 0.5mm or 0.75mm thick skin model. The difference between the results of slit positions with 0.75mm and 1mm skin model is not obvious. Figure 67 (a)-(d) are the integrated power versus the incident angles. Figure 68 (a)-(d) are the integrated power over the incident angles to the normal of the plane of the "transparent film" in simulation-I and II (Figure 52). Figure 68 (a)-(d) are the normalized integrated power versus incident angles. In Figure 63(a), within 2 degree, there are 57.3% (slit=0.6mm), 47.5% (slit=1mm), 40.8% (slit=1.4mm) and 35.4% (slit=2mm) integrated power when the slit is positioned in the focal plane of focusing optics which is far from the skin, in contrast, when the slit is positioned right in front of the skin model, the integrated power is 62.8% (slit=0.6mm), 58.6% (slit=1mm), 54.7% (slit=1.4mm), and 54.0% (slit=2mm) integrated power. From the integrated power, we can see that there is more photon power within a smaller incident angles and there is more photon power collected totally with slit positioned right in front of the skin model when the skin model is 0, 0.5 or 0.75mm. When the skin model is 1mm, there is less photon power within a smaller incident angles and less photon power collected totally when the width of the slit is 0.6 and 1mm. The normalized integrated power reveals that a greater fraction of total power can be captured within a small angle (<2º) when the skin model is thinner than 0.75mm. The difference resulting from the slit position is not obvious when skin model goes to 1mm; this may be attributed to the lower excitation power reaching the sensor. Overall, the simulation results indicate that the slit placed in front of the skin (phantom) increased the degree of collimation of luminescence photons. Moreover, the system with a slit in front of skin is simpler to construct, and therefore this design was used in the experimental work.

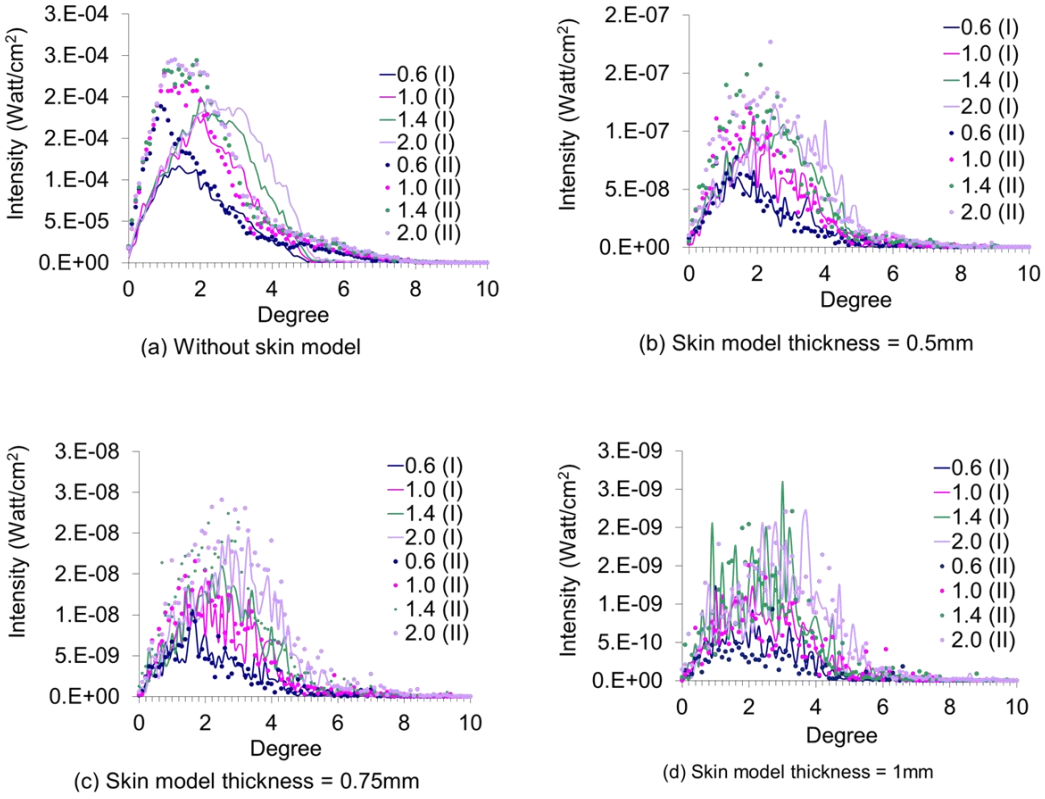

Figure 66. Intensity distribution of photons collected on the "transparent film" in Figure 52. The inputs in all simulations were 1watt.

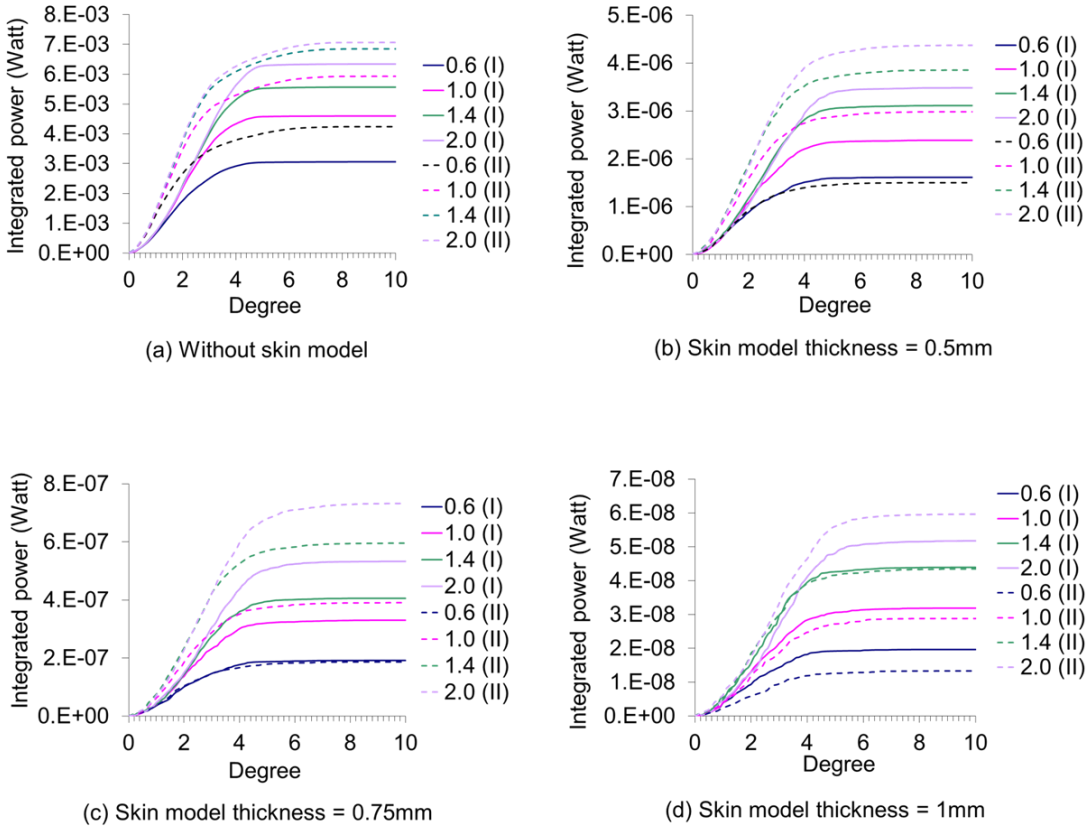

Figure 67. Integrated power of photons collected on the “transparent film” in Figure 52. Inputs of excitation light were 1watt in simulations.

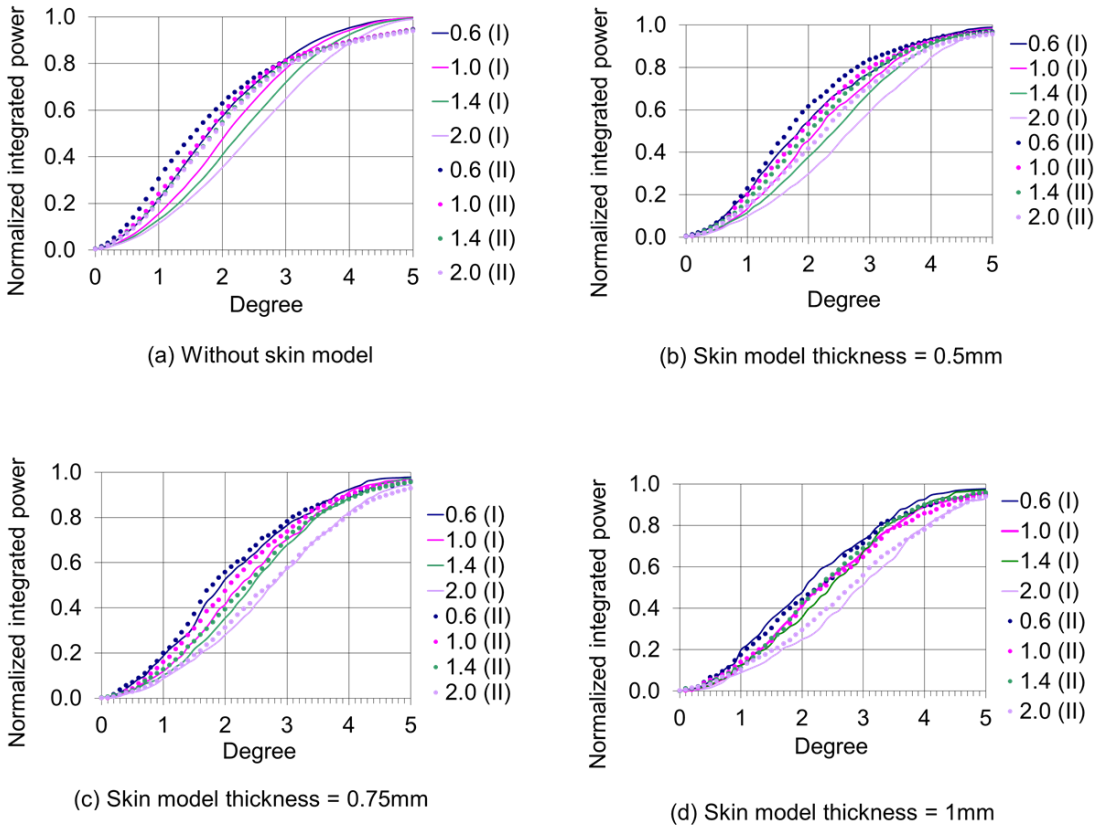

Figure 68. Normalized integrated power.

Thus, the entrance slit was designed to be on the focal plane of the excitation light according to the design as shown in Figure 69. However, it is noted that this design could not collect as much luminescence photons as those collected by the design shown in Figure 51, in which the entrance slit was placed on the focal plane of focal plane of emission light. Because the excitation light is confined by the entrance slit, it is necessary to study the influence of the focal spot of excitation light on the luminescence photons escaping from the skin surface. Thus, simulations were performed to study the influence, and Figure 64 shows the simulated result. Blue diamonds are the results when the skin model thickness was 1mm, and pink circles are the results when the skin model thickness was 0.5mm. The luminescent emission was normalized to 1. The skin model positions are the distance relative to a lens (LA1951, Thorlab), which was used in the simulations. The orange vertical line represents the where the focal plane of the lens is. As shown in this figure, the maximum of the escaping luminescence photons are reached before the focal plane of the lens. Thus, it would be better to make the optics which collect the excitation light from LED and deliver it to the system adjustable so as the make the spot size converging angle of the excitation adjustable. Since the spot size of the excitation light would be confined by the entrance slit, it is necessary to use a lens with a smaller focal length to make the incident spot size smaller. Thus a half-ball high refractive index lens with 8mm diameter was used as the front lens placed in front of the slit. It is able to minimize the spot size of the excitation light as well as increase the numerical aperture of the system.

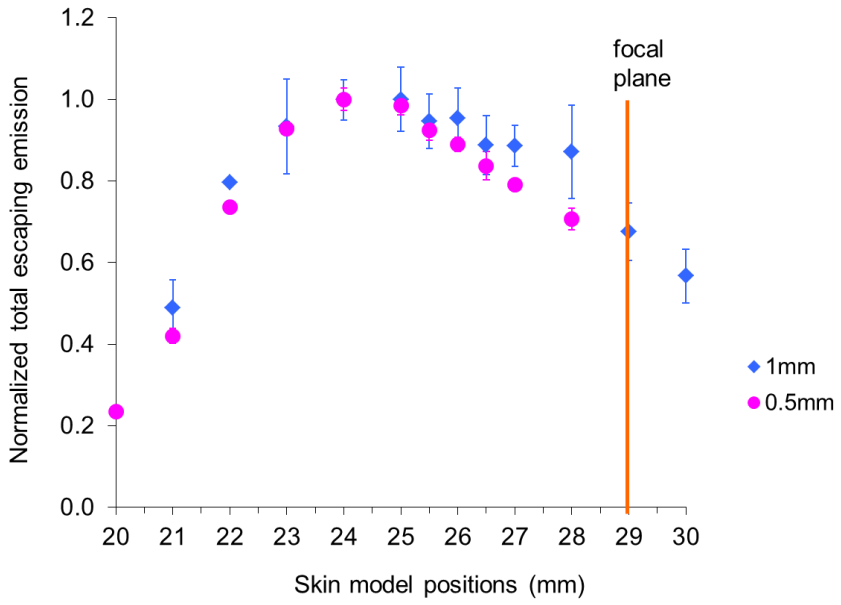

Figure 69. Normalized total escaping luminescent emission. X-axis was the skin model position relative to the lens. Error bars are 1 standard deviations.

The final design of the customized spectrometer is shown in Figure 70. The grating (NT 46-078, Edmund Optics) was ruled at 750nm with 1200/mm groove density, and the size is 30mm×30mm. The concave mirror (NT 43-470, Edmund Optics) is 50mm in diameter, and is of 50mm focal length. The detector (TCD1304AP) is from Toshiba, which is the same as the one used in Ocean optics USB4000. The half-ball lens (NT 90-860, Edmund Optics) is 8mm in diameter and of high refractive index (LaSFN9). A 1mm slit was chosen for the measurement of the two peaks at 585nm and 645nm, and Figure 66 shows the spectral response of the system. With a 1mm slit, the luminescent photons collected by this customized system is simulated to be ~100 times higher than that collected by the fiber bundle system.

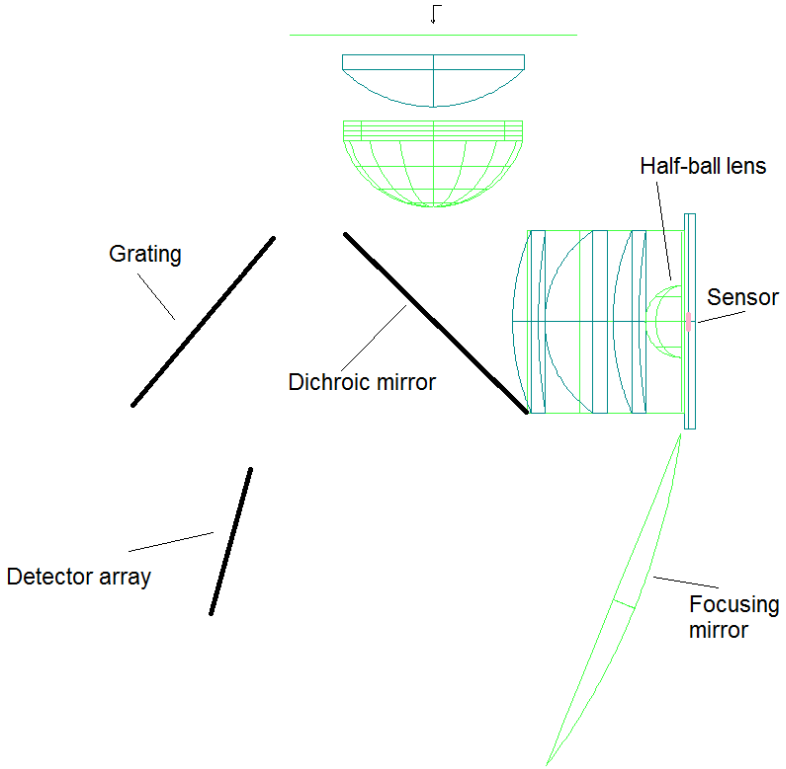

Figure 70. Final design of the customized spectrometer system

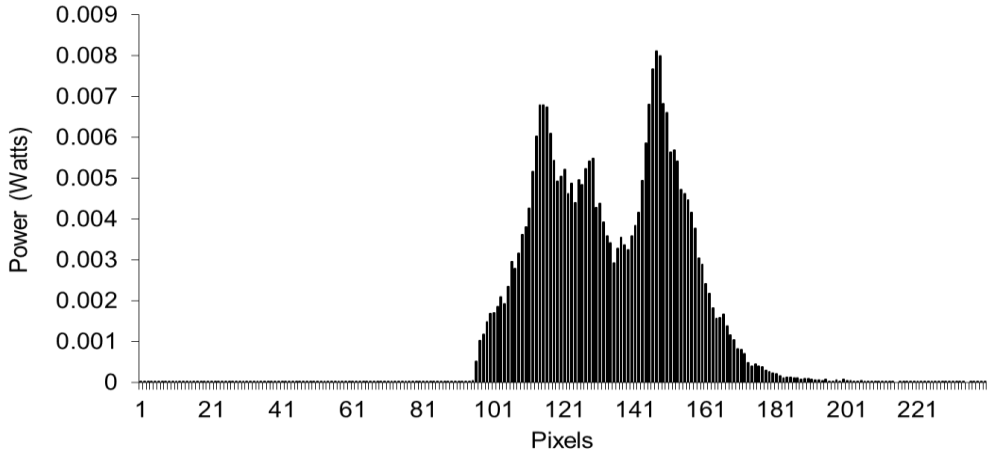

Figure 71. Simulated spectral response of the emissions at 585 and 645nm on the detector obtained by the system with a 1mm slit.

5.3.3 Results of experimental evaluation of the customized spectrometer

The comparisons of the hardware system and fiber bundle system testing results are presented in Figure 72-75. Figure 72 (a) and (b) are the spectra of the two light sources obtained by the hardware system and the fiber bundle system, and the integration time (IT) was kept 1ms in both measurements. The two light sources were obtained from the white light source (LS-1, Ocean Optics) filtered by two band pass filters (580±20nm and 645±20nm). In Figure 72(a), the peaks of the spectra obtained by the hardware system were around 9000 and 7000 photon counts. In Figure 68(b), the peak of 580nm was around 15000 photon counts which was higher than that obtained by the hardware system, but the peak of 645nm was only around 500 photon counts. The problem may be attributed to the poor fiber coupling or inner misalignment of the fiber bundles. Figure 73(a) and (b) are the spectra of the two light sources covered by a 1.24mm phantom, and the integration time was kept 500ms in both measurements. In Figure 73, the peaks

of the spectra obtained by the hardware system is 10 times higher than that obtained by the fiber bundle system. Figure 74 (a) and (b) show the spectra of the two light sources covered by a 1.74mm phantom, and the integration time was kept 500ms in both measurements. The peaks of the spectra obtained by the hardware is 8 times higher than that obtained by the fiber bundle. Figure 75 (a) and (b) show the spectra of the two light sources covered by a 2.48mm phantom. The peaks of the spectra obtained by the hardware is around 8 times higher. These measurements of the light sources aimed to compare the collection efficiency of these two systems, and the results agreed well with estimations. Because the numerical aperture (~0.8-0.9 depends on the input light source size) of the customized system is around 4 times higher than that (0.22) of the fiber bundle, and only around half of the fibers are for emission collection, thus the collection efficiency of the designed system is expected to be around 8 times higher than that of fiber bundle system. For sensor interrogations, the efficiency of the delivery of excitation needs to be considered. Figure 76-79 show the comparisons of interrogation efficiency of these two systems. Figure 76 compares the conditions without phantoms. When the integration time was 8ms, the spectra of the emission from the samples obtained by the hardware system were ~100time higher than that obtained by the fiber bundle. When the phantom (thickness=0.50 mm) was attached and the integration time was kept 500ms, in Figure 77, the photon counts of customized spectrometer were still ~100 times than that of the fiber bundle. When the phantom (0.95mm) was used, in Figure 78 (b) there were no detectable signals observed by the fiber bundle. This increase of overall interrogation efficiency of the customized system is even higher than the gain in collection efficiency. This is mainly because the delivery efficiency of the excitation light of the customized system is also higher than that of fiber bundle. The excitation light delivered by the customized system was well focused and penetrated into the skin phantom, while the excitation light delivered by fiber bundle diverged and the intensity arriving at the sensors is smaller. In

contrast, a spectral trend can be detected with the customized spectrometer with 500ms integration time. The shorter wavelength range (around 580nm) was strongly attenuated, but the signal of longer wavelength range was detected. This was expected in simulations, because the skin model absorbs most emission at shorter wavelength. In simulations, the photon counts detected by the customized spectrometer system were 100 times higher than that detected by fiber bundle. The customized system should be more capable than the fiber bundle system for in vivo measurement, in which the luminescence signal was strongly attenuated by animal skin.

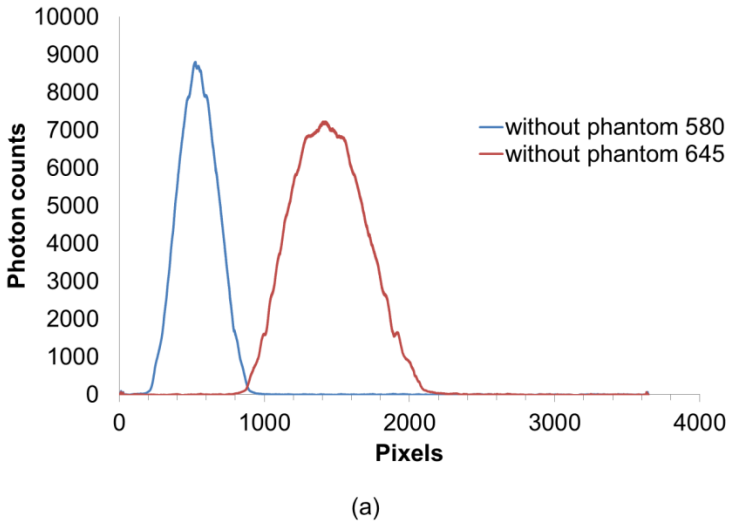

Figure 72. Spectra of the two light sources without a phantom covered (a) obtained by the hardware system, IT=1ms; (b) obtained by the fiber bundle, IT=1ms

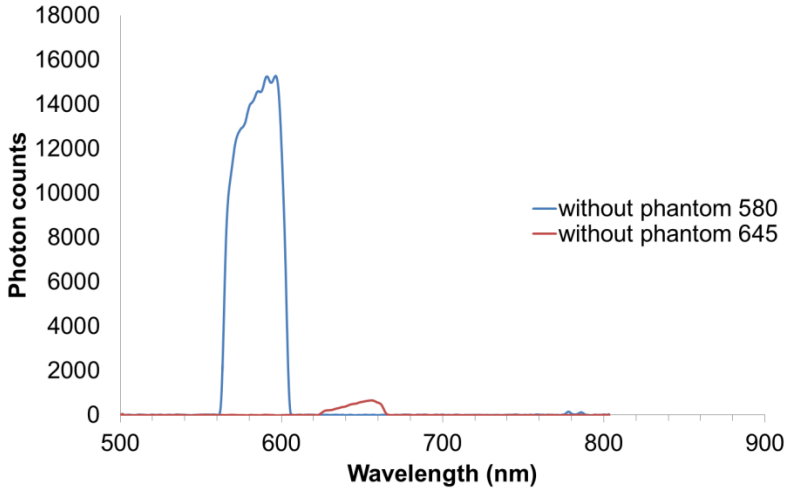

(b)

Figure 72. Continued.

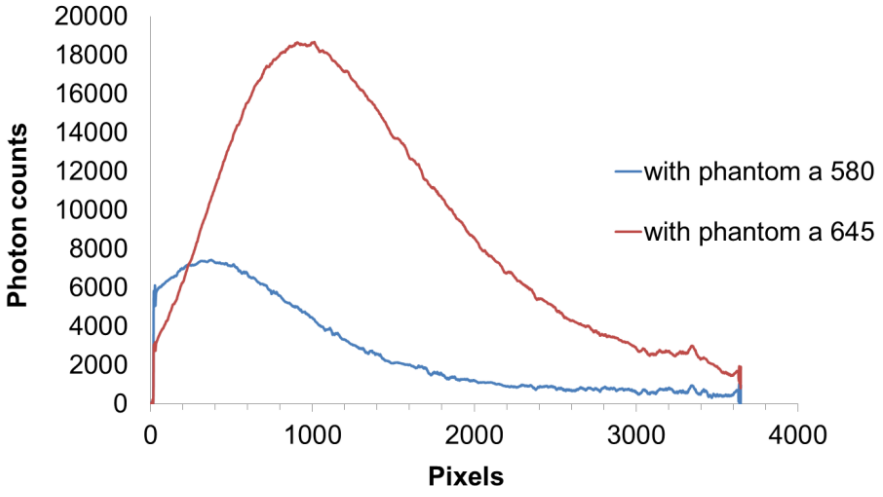

(a)

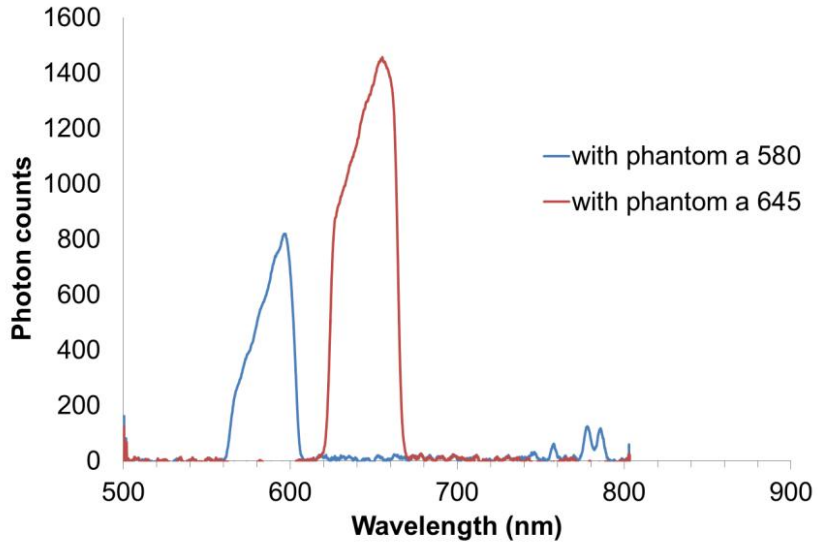

(b)

Figure 73. Spectra of the two light sources with a 1.24mm phantom covered (a) obtained from the hardware system, IT=500ms; (b) obtained from the fiber bundle, IT=500ms

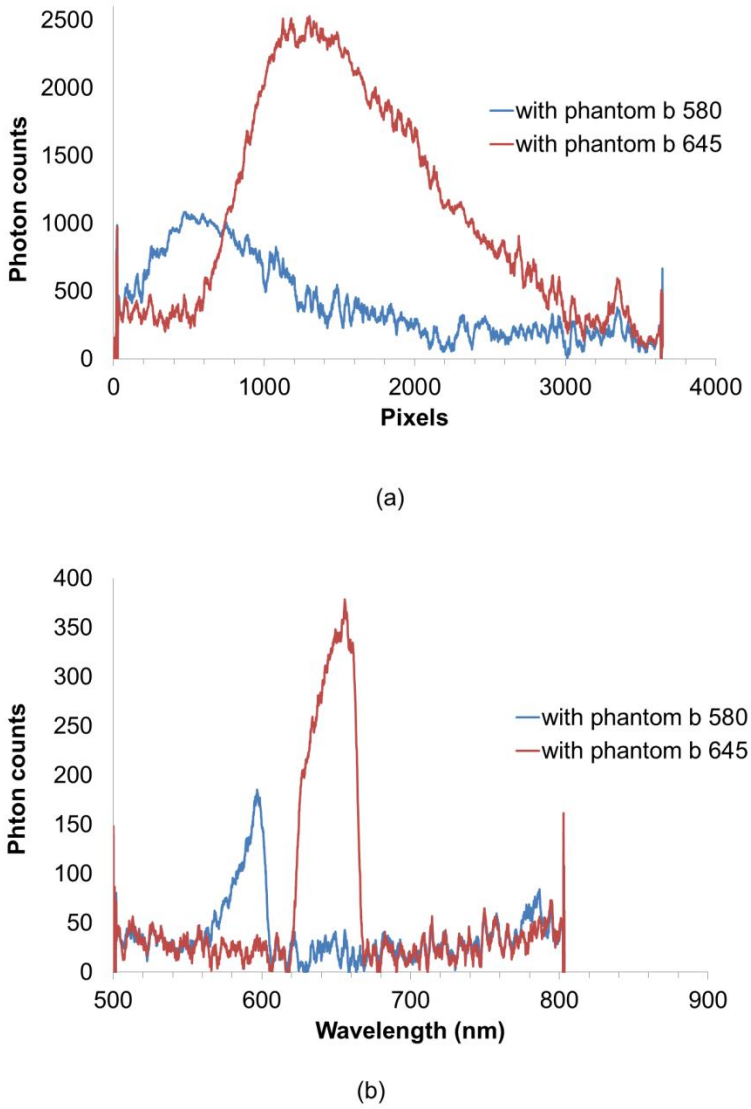

Figure 74. Spectra of the two light sources with a 1.74mm phantom covered (a) obtained from the hardware system, IT=500ms; (b) obtained from the fiber bundle, IT=500ms

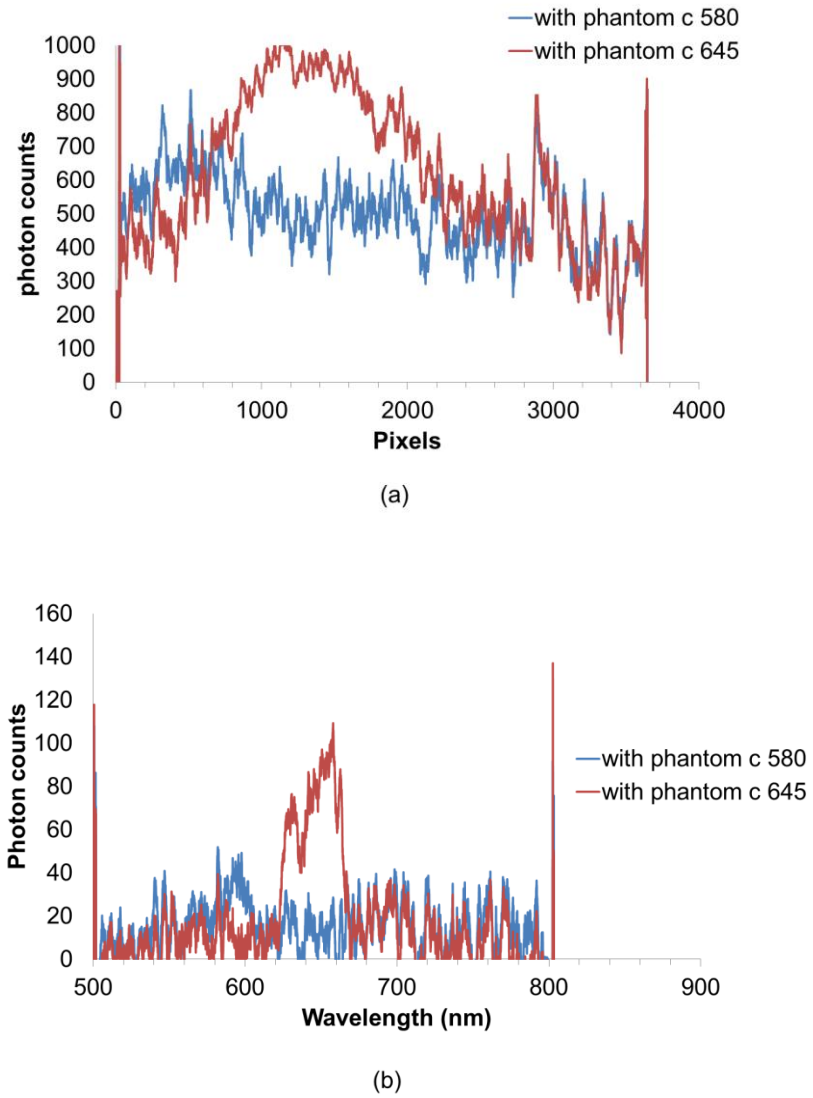

Figure 75. Spectra of the two light sources with a 2.48mm phantom covered (a) obtained from the hardware system, IT=500ms; (b) obtained from the fiber bundle, IT=500ms

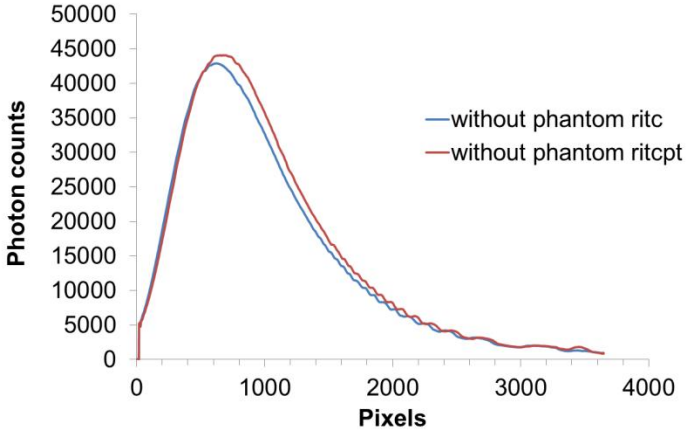

(a)

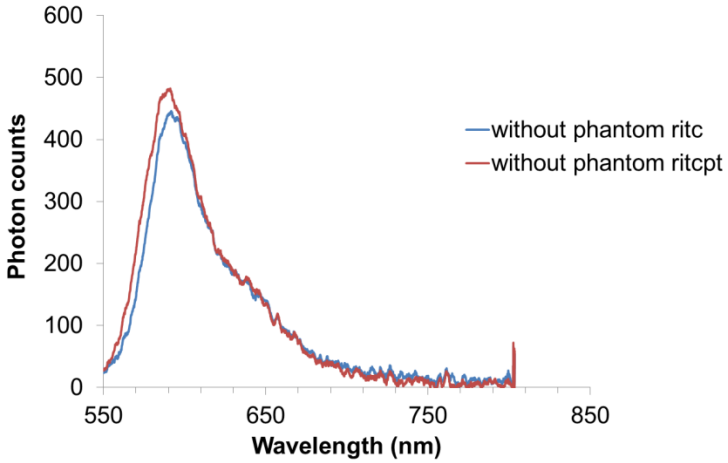

(b)

Figure 76. Spectra of the emission from RITC solutions and the mixture of RITC and PtOEP solutions, which was not covered by a phantom (a) obtained from the hardware system, IT=8ms; (b) obtained from the fiber bundle, IT=8ms

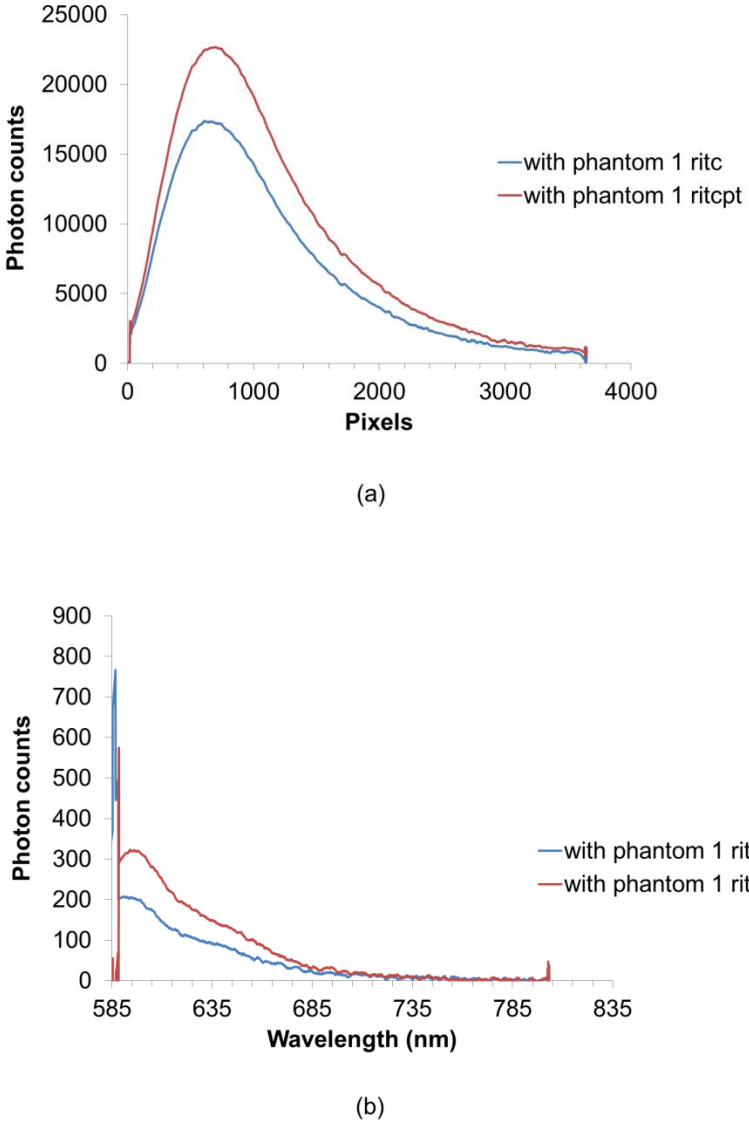

Figure 77. Spectra of the emission from RITC solutions and the mixture of RITC and PtOEP solutions, which was covered by a 0.50mm phantom (a) obtained from the hardware system, IT=500ms; (b) obtained from the fiber bundle, IT=500ms

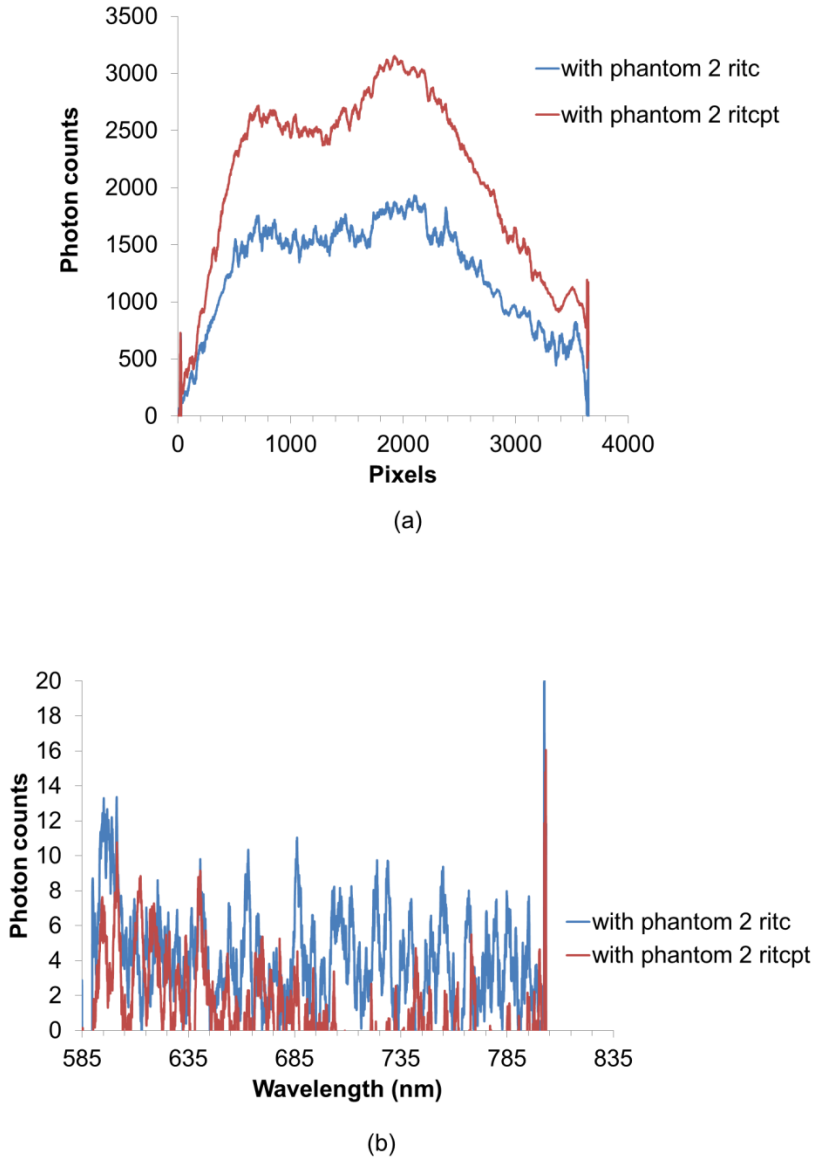

Figure 78. Spectra of the emission from RITC solutions and the mixture of RITC and PtOEP solutions, which was covered by a 0.96mm phantom (a) obtained from the hardware system, IT=500ms; (b) obtained from the fiber bundle, IT=500ms

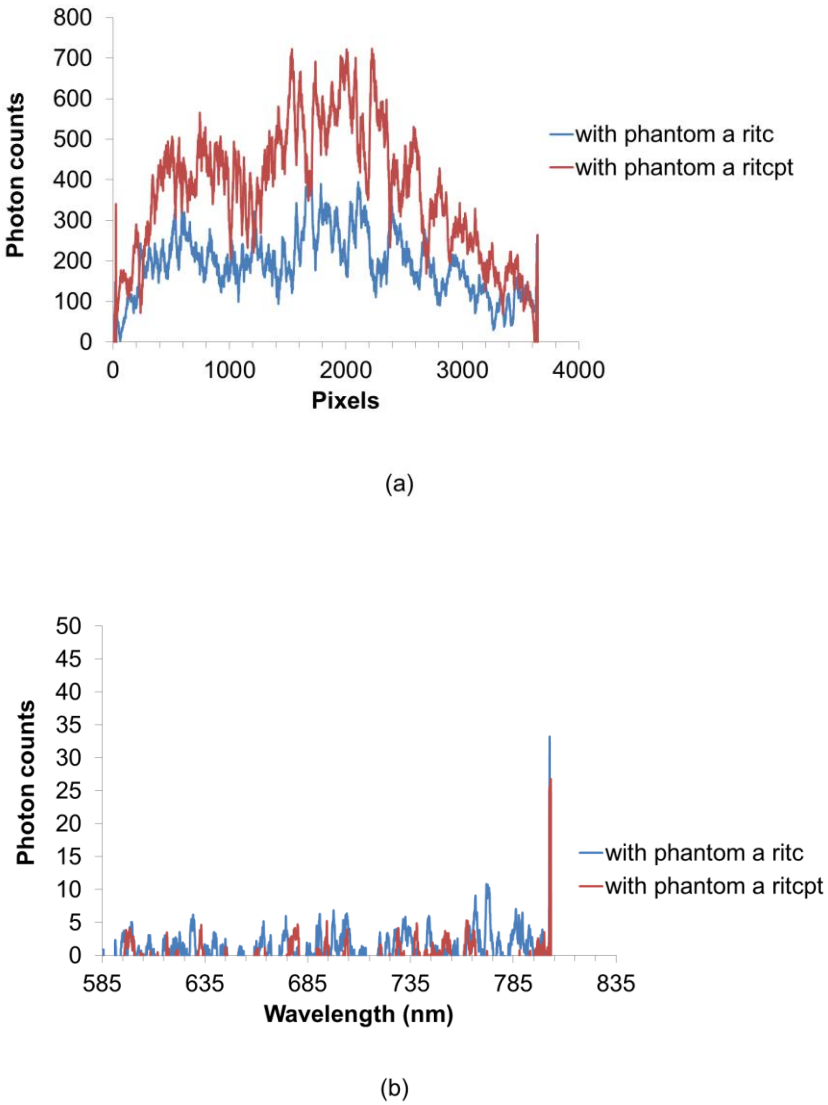

Figure 79. Spectra of the emission from RITC solutions and the mixture of RITC and PtOEP solutions, which was covered by a 1.24mm phantom (a) obtained from the hardware system, IT=500ms; (b) obtained from the fiber bundle, IT=500ms

5.4 Comparison of these two approaches of system optimization

Table 10 is a comparison of the two optimization approaches. For the resolution of these two systems, it is determined by the band-width of the band pass filters of the two-detector system, whereas, it can be determined by the width of entrance slit of the customized spectrometer. Thus, changing the slits can enable the change of resolutions for the customized spectrometer, and changing filters also can enable the change of resolution for the two-detector system. Application of the two-detector system is limited to a degree by the filters and dichroic mirror, because the wavelength range is fixed. The application of the customized spectrometer is relatively more flexible that of the two-detector system, because as long as the emission is within the wavelength range of the grating in the customized spectrometer the emission can be measured by the customized spectrometer. For the application of luminescent sensor measurement, the two-detector system can only measure two emissions, while the customized system can measure luminescent emissions of more than two dyes, if desired. If just intended for the measurement of two emissions, the CCD in the customized system can be replaced with discrete photodiode detectors to increase the photon capture efficiency, since the active area of the photodiode detector is often bigger than that of a 1-D CCD array. However, the two-detector system is easier to assemble and immobilize than the customized spectrometer. The cost of these two systems are almost the same, each cost around $400. In experimental evaluations, both systems showed good SNR and the capability of working on a thick skin phantom (~1mm). However, the spectra obtained by the prototype of the customized spectrometer showed more stray light and noise than the fiber bundle, which needs to be overcame in the future. The main source of stray light of the custom system is coming from the backscattered excitation light, since there is no ideal excitation filter and the fluorescent signal is always much weaker than that of excitation light. To reduce the stray light, another long-pass filter (575nm LP) will be needed to block more back

scattered excitation light leaking from the dichroic mirror, and some optics might need to be adjusted to reduce the aberrations.

Table 10. Comparison of two optimization methods

	Two-detector system	Customized spectrometer
Resolution	adjustable	adjustable
Detectors	photo-diode	CCD array
Extra Filters	3	0
Simulation	Compare photon counts on detector films	
Application	Fixed pair of emission	Luminescent emission within the wavelength range of the grating
Complexity	low	more
Total Price	moderate	moderate

5.5 Conclusions

To deploy dermal implants for on-demand monitoring, a matched optoelectronic system for interrogation of sensors is needed. It was observed that the efficiency of the system designed in the last section was compromised due to losses from fiber connections and the entrance aperture of the commercial spectrometer used in experimental evaluation; >99.9% photons collected by the system were lost at the entrance plane of the current spectrometer. This finding highlights the different demands placed on optical sensors. The current trends of spectrometer design are aimed at obtaining high spectral resolution by minimizing the entrance aperture and slit width; this results in decreased signal due to the trade-off between spectral resolution and input energy. However, for luminescence measurements, it is common that only specific, relatively broad bands of the spectrum are of interest. Furthermore, luminescent signals collected from tissue or implants will be strongly attenuated by tissue scattering and absorption; therefore, signal power

should take priority over spectral resolution. Thus, a more appropriate high-efficiency hardware system to interrogate luminescent sensors is needed. Two optimization approaches were applied to solve the photon loss problem: a two-detector system and a customized spectrometer. Experiments of two-detector system in static in vitro experiment showed good SNR. The customized spectrometer was designed to maximize the throughput while maintaining a sufficient spectral resolution. Compared with the two-detector system, the customized spectrometer is more flexible, since the two-detector system is only able to measure one specific pair of luminescence emission, if the emission peaks change, (e.g. sensors are redesigned), the filters and mirrors have to be changed. However, the customized system has more stray light and noise, which need to be optimized in the future. Both systems overcome the problem of significant photon loss compared to commercial spectrometers by maximizing the input energy of luminescent photons while maintaining the required spectral resolution. The customized system can be directly coupled to an analog-to-digital converter and integrated circuits, which offers potential for a single compact and portable device for field use with luminescent diagnostic systems as well as our dermally-implanted sensors.

6. CONCLUSIONS

Dermally-implanted luminescent microparticle glucose sensors are being developed in our lab to enable minimally-invasive on-demand monitoring of glucose. To interrogate the sensors in vivo, it is necessary to design a matched optoelectronic system for delivery of excitation light, collection of luminescence, and measurement of luminescence the response with high efficiency. In my research, light propagation in skin and interaction with implanted microparticle sensors were studied using modeling, and an optical system based on the modeling results was designed, evaluated, and finally the optimization of the system was performed.

Three-dimensional, multi-wavelength simulations of light interaction with tissue and luminescent materials revealed the key factors influencing the generation and collection of fluorescence from sensors implanted in the dermis at different depths and concentrations, which provides critical information for the work of hardware design. The results of simulations to predict sensor *in vivo* performance showed that the spectral distortion resulting from the absorption and scattering of the skin, particle size, or particle concentrations has minimal influence over the predicted ratiometric measurements indicating that the in vivo data will only require minimal calibrations in the future.

An optical system of high efficiency to interrogate dermally-implanted microparticle sensors was designed and constructed. The silicone-based skin phantoms which match the maximum value of the published optical properties of human skin were developed as the permanent evaluation medium to minimize the animal use. This skin phantom is also useful in testing system design and facilitated system optimization of optical instrument system for dermal diagnostic. Experimental validations showed a good agreement with results of simulations, proving the accuracy of measured optical properties of developed skin phantom, and the

accuracy of the simulation system including Monte Carlo ray-tracing and geometric ray-tracing. Evaluation of the hardware system with developed skin phantoms indicated that there should be no obstacles for the optical hardware to meet expectations for *in vivo* analysis of implants. However, a significant photon loss was observed at the connections of hardware and the commercial spectrometer, which needs to be overcome for optimal performance.

Two optimization approaches were applied to solve the photon loss problem, and the two approaches are the two-detector system and the customized spectrometer. Experiments of two-detector system in static in vitro experiment showed good SNR. The customized system is hundred times more efficient to measure luminescent light than the fiber bundle and commercial spectrometer while the spectral resolution is still good enough. Compared with the two-detector system, the customized spectrometer is more flexible, since the two-detector system is only able to measure one specific pair of luminescence emission, if the emission peaks change, the filters and mirrors have to be changed. However, the customized spectrometer system has more stray light and noise, which needs to be optmized in the future. Both systems solve the problem of significant photon loss by maximizing the input energy of luminescent photons while maintaining the required spectral resolution.

In the future, a multi-layered skin phantom or micro-fluidic structured skin phantom can be developed based on the current work of skin phantoms to enable a more accurate skin phantom system. Though the system was designed for luminescent intensity measurement, because it separates fluorescence emissions spectrally, the detected signals can also be processed to measure the fluorescence life time. The optimized system can be modified into a more compact system, and it can be directly coupled to an analog-to-digital converter and integrated circuits, which offers potential for a single compact and portable device for field use with luminescent diagnostic systems as well as our dermally-implanted sensors.

REFERENCES

1. T. Acker, and H. Acker, "Cellular oxygen sensing need in CNS function: physiological and pathological implications," J Exp Biol **207**, 3171-3188 (2004).

2. G. L. Coté, "Noninvasive and minimally-invasive optical monitoring technologies," J. Nutr. **131**, 1596S-1604S (2001).

3. J. Park, C. S. Kim, and M. Choi, "Oxidase-coupled amperometric glucose and lactate sensors with integrated electrochemical actuation system," Ieee T Instrum Meas **55**, 1348-1355 (2006).

4. "Cholesterol," http://en.wikipedia.org/wiki/Cholesterol (Accessed 09 2011).

5. "What is diabetes?," http://www.idf.org/diabetesatlas/what-is-diabetes (Accessed 09 2011).

6. "National diabetes fact sheet, 2007," (2007), http://www.cdc.gov/diabetes/pubs/pdf/ndfs_2007.pdf (Accessed 09 2011).

7. "Diabetes mellitus," http://en.wikipedia.org/wiki/Diabetes_mellitus (Accessed 09 2011).

8. "National Diabetes Information Clearinghouse (NDIC)," http://diabetes.niddk.nih.gov/DM/pubs/glucosemonitor/ (Accessed 09 2011).

9. "The Diabetes Control and Complications Trial Research G. The Effect of Intensive Treatment of Diabetes on the Development and Progression of Long-Term Complications in Insulin-Dependent Diabetes Mellitus.," N Engl J Med. **329**, 977-986 (1993).

10. K. G. M. M. Alberti, P. Z. Zimmet, and W. Consultation, "Definition, diagnosis and classification of diabetes mellitus and its complications part 1: Diagnosis and classification of diabetes mellitus - Provisional report of a WHO consultation," Diabetic Medicine **15**, 539-553 (1998).

11. J. Gerich, " Diabetic Control and the Late Complications of Diabetes," American family physician **16**, 85-91 (1977).

12. J. M. M. Evans, R. W. Newton, D. A. Ruta, T. M. MacDonald, R. J. Stevenson, and A. D. Morris, "Frequency of blood glucose monitoring in relation to glycaemic control: observational study with diabetes database," British Medical Journal **319**, 83-86 (1999).

13. M. I. Harris, "Frequency of blood glucose monitoring in relation to glycemic control in patients with type 2 diabetes," Diabetes Care **24**, 979-982 (2001).

14. L. Kennedy, "Self-monitoring of blood glucose in type 2 diabetes - Time for evidence of efficacy," Diabetes Care **24**, 977-978 (2001).

15. R. Ballerstadt, and J. S. Schultz, "A fluorescence affinity hollow fiber sensor for continuous transdermal glucose monitoring," Anal. Chem. **72**, 4185-4192 (2000).

16. J. R. Lakowicz, I. Gryczynski, Z. Gryczynski, J. D. Dattelbaum, L. Tolosa, and G. Rao, "Novel methods for fluorescence sensing," Proceedings of SPIE - The International Society for Optical Engineering **3602**, 234 (1999).

17. J. R. Lakowicz, and H. Szmacinski, "Fluorescence lifetime-based sensing of pH, Ca^{2+}, K^{+} and glucose," Sens. Actuators, B **11**, 133-143 (1993).

18. J. R. Lakowicz, H. Szmacinski, and R. B. Thompson, "Fluorescence-lifetime-based sensing: applications to clinical chemistry and cellular imaging," in *Ultrasensitive Laboratory Diagnostics*(SPIE, Los Angeles, CA, USA, 1993), pp. 2-17.

19. J. S. Schultz, and G. Sims, "Affinity sensors for individual metabolites," Biotechnol. Bioeng. Symp. **9**, 65-71 (1979).

20. M. J. McShane, S. Rastegar, M. Pishko, and G. L. Cote, "Monte Carlo modeling for implantable fluorescent analyte sensors," IEEE Trans. Biomed. Eng. **47**, 624-632 (2000).

21. R. Ballerstadt, A. Gowda, and R. McNichols, "Fluorescence resonance energy transfer-based near-infrared fluorescence sensor for glucose monitoring," Diabetes Technol. Ther. **6**, 191-200 (2004).

22. M. J. McShane, "Potential for glucose monitoring with nanoengineered fluorescent biosensors," Diabetes Technol. Ther. **4**, 533-538 (2002).

23. M. J. McShane, D. P. O'Neal, R. J. Russell, M. V. Pishko, and G. L. Cote, "Progress toward implantable fluorescence-based sensors for monitoring glucose levels in interstitial fluid," in *Optical Diagnostics of Biological Fluids V*(Proc. SPIE, San Jose, CA, USA, 2000), pp. 78-87.

24. R. J. Russell, M. V. Pishko, C. C. Gefrides, M. J. McShane, and G. L. Cote, "A fluorescence-based glucose biosensor using concanavalin A and dextran encapsulated in a poly(ethylene glycol) hydrogel," Anal. Chem. **71**, 3126-3132 (1999).

25. S. Chinnayelka, and M. J. McShane, "Glucose-sensitive nanoassemblies comprising affinity-binding complexes trapped in fuzzy microshells," J. Fluoresc. **14**, 585-595 (2004).

26. S. Chinnayelka, and M. J. McShane, "Microcapsule biosensors using competitive binding resonance energy transfer assays based on apoenzymes," Anal. Chem. **77**, 5501-5511 (2005).

27. P. S. Grant, and M. J. McShane, "Development of multilayer fluorescent thin film chemical sensors using electrostatic self-assembly," IEEE Sensors J. **3**, 139-146 (2003).

28. M. J. McShane, "Microcapsule Glucose Sensors: Engineering systems with enzymes and glucose-binding sensing elements," in *Topics in Fluorescence*, J. R. Lakowicz, and C. D. Geddes, eds. (Springer Science, New York, 2006).

29. E. W. Stein, P. S. Grant, H. G. Zhu, and M. J. McShane, "Microscale enzymatic optical biosensors using mass transport limiting nanofilms. 1. Fabrication and characterization using glucose as a model analyte," Anal. Chem. **79**, 1339-1348 (2007).

30. E. W. Stein, S. Singh, and M. J. McShane, "Microscale enzymatic optical Biosensors using mass transport limiting nanofilms. 2. Response modulation by varying analyte transport properties," Anal. Chem. **80**, 1408-1417 (2008).

31. R. Long, S. Singh, and M. McShane, "Stability of response and in vivo potential of microparticle glucose sensors," in *Optical Diagnostics and Sensing VIII*(SPIE, San Jose, CA, USA, 2008), pp. 686307-686308.

32. S. Singh, and M. McShane, "Enhancing the longevity of microparticle-based glucose sensors towards 1 month continuous operation," Biosensors & Bioelectronics **25**, 1075-1081 (2010).

33. W. F. Cheong, S. A. Prahl, and A. J. Welch, "A Review of the Optical-Properties of Biological Tissues," Ieee J Quantum Elect **26**, 2166-2185 (1990).

34. M.-A. Mycek, and B. W. Pogue, *Handbook of biomedical fluorescence* (Marcel Dekker, 2003).

35. "Some biological chromophores," http://omlc.ogi.edu/classroom/ece532/class3/chromophores.html (Accessed 10 2011).

36. "Absorption spectra for biological tissues," http://omlc.ogi.edu/classroom/ece532/class3/muaspectra.html (Accessed 10 2011).

37. "Beer-Lambert law," http://en.wikipedia.org/wiki/Beer%E2%80%93Lambert_law (Accessed 09 2011).

38. L. Wang, and S. L. Jacques, "Monte Carlo modeling of light transport in multi-layered tissues in standard C," (1992).

39. "Luminescence," http://en.wikipedia.org/wiki/Luminescence (Accessed 09 2011).

40. "Basic photophysics," http://www.photobiology.info/Visser-Rolinski.html (Accessed 09 2011).

41. "Fluoresecence," http://en.wikipedia.org/wiki/Fluorescence#Quantum_yield (Accessed 09 2011).

42. "Scattering," http://en.wikipedia.org/wiki/Scattering (Accessed 08 2011).

43. "Optical properties - Scattering," http://omlc.ogi.edu/classroom/ece532/class3/scattering.html (Accessed 09 2011).

44. "Some biological scatterers," http://omlc.ogi.edu/classroom/ece532/class3/scatterers.html (Accessed 09 2011).

45. "Scattering functions," http://omlc.ogi.edu/classroom/ece532/class3/ptheta.html (Accessed 09 2011).

46. "Mean free path," http://www.euronuclear.org/info/encyclopedia/m/mean-fee-path.htm (Accessed 09 2011).

47. "Mean free path - physics," http://en.wikipedia.org/wiki/Mean_free_path (Accessed 09 2011).

48. "OptiCAD manual (2010)," http://www.opticad.com (Accessed 05 2010).

49. B. C. Wilson, and G. Adam, "A Monte-Carlo Model for the Absorption and Flux Distributions of Light in Tissue," Med. Phys. **10**, 824-830 (1983).

50. "Monte Carlo method," http://en.wikipedia.org/wiki/Monte_Carlo_method (Accessed 09 2011).

51. Q. Liu, C. F. Zhu, and N. Ramanujam, "Experimental validation of Monte Carlo modeling of fluorescence in tissues in the UV-visible spectrum," J. Biomed. Opt. **8**, 223-236 (2003).

52. S. Avrillier, E. Tinet, D. Ettori, J. M. Tualle, and B. Gelebart, "Influence of the emission-reception geometry in laser-induced fluorescence spectra from turbid media," Appl. Opt. **37**, 2781-2787 (1998).

53. M. Keijzer, R. R. Richardskortum, S. L. Jacques, and M. S. Feld, "Fluorescence spectroscopy of turbid media - autofluorescence of the human aorta," Appl. Opt. **28**, 4286-4292 (1989).

54. Q. Liu, and N. Ramanujam, "Relationship between depth of a target in a turbid medium and fluorescence measured by a variable-aperture method," Opt. Lett. **27**, 104-106 (2002).

55. T. J. Pfefer, K. T. Schomacker, M. N. Ediger, and N. S. Nishioka, "Light propagation in tissue during fluorescence spectroscopy with single-fiber probes," IEEE J. Sel. Topics. Quantum Electron. **7**, 1004-1012 (2001).

56. B. W. Pogue, and G. Burke, "Fiber-optic bundle design for quantitative fluorescence measurement from tissue," Appl. Opt. **37**, 7429-7436 (1998).

57. B. W. Pogue, and T. Hasan, "Fluorophore quantitation in tissue-simulating media with confocal detection," IEEE J. Sel. Topics. Quantum Electron. **2**, 959-964 (1996).

58. J. N. Qu, C. Macaulay, S. Lam, and B. Palcic, "Laser-induced fluorescence spectroscopy at endoscopy - tissue optics, Monte-Carlo modeling, and in-vivo measurements," Opt. Eng. **34**, 3334-3343 (1995).

59. J. N. Y. Qu, Z. J. Huang, and J. W. Hua, "Excitation-and-collection geometry insensitive fluorescence imaging of tissue-simulating turbid media," Appl. Opt. **39**, 3344-3356 (2000).

60. A. J. Welch, C. Gardner, R. Richards-Kortum, E. Chan, G. Criswell, J. Pfefer, and S. Warren, "Propagation of fluorescent light," Lasers Surg. Med. **21**, 166-178 (1997).

61. R. Drezek, K. Sokolov, U. Utzinger, I. Boiko, A. Malpica, M. Follen, and R. Richards-Kortum, "Understanding the contributions of NADH and collagen to cervical tissue

fluorescence spectra: modeling, measurements, and implications," J. Biomed. Opt. **6**, 385-396 (2001).

62. H. Zeng, C. MacAulay, D. I. McLean, and B. Palcic, "Reconstruction of in vivo skin autofluorescence spectrum from microscopic properties by Monte Carlo simulation," J. Photochem. Photobiol., B **38**, 234-240 (1997).

63. W. Zheng, Z. Huang, and S. Xie, "Autofluorescence spectrum of human bronchial tissue by Monte Carlo modeling," Acta-Photonica-Sinica **30**, 669-674 (2001).

64. G. I. Zonios, R. M. Cothren, J. T. Arendt, J. Wu, J. VanDam, J. M. Crawford, R. Manoharan, and M. S. Feld, "Morphological model of human colon tissue fluorescence," IEEE Trans. Biomed. Eng. **43**, 113-122 (1996).

65. V. Asadpour, M. H. Miranbeigi, F. Towhidkhah, and M. E. Khosroshahi, "Laser-Doppler blood-flowmetery modeling by Monte Carlo method," P Ann Int Ieee Embs **23**, 3252-3254, 4132 (2001).

66. T. Binzoni, T. S. Leung, and D. Van De Ville, "The photo-electric current in laser-Doppler flowmetry by Monte Carlo simulations," Physics in Medicine and Biology **54**, N303-N318 (2009).

67. F. F. M. Demul, M. H. Koelink, M. L. Kok, P. J. Harmsma, J. Greve, R. Graaff, and J. G. Aarnoudse, "Laser-Doppler Velocimetry and Monte-Carlo Simulations on Models for Blood Perfusion in Tissue," Applied Optics **34**, 6595-6611 (1995).

68. I. Fredriksson, M. Larsson, and T. Stromberg, "Optical microcirculatory skin model: assessed by Monte Carlo simulations paired with in vivo laser Doppler flowmetry," Journal of Biomedical Optics **13**, - (2008).

69. A. Jakobsson, and G. E. Nilsson, "Estimation of Sampling Depth in Laser Doppler Flowmetry Based on a Monte-Carlo Model," Proceedings of the Annual International Conference of the IEEE Engineering in Medicine and Biology Society, Vol 13, Pts 1-5, 1753-1754, 2400 (1991).

70. H. W. Jentink, F. F. M. Demul, R. G. A. M. Hermsen, R. Graaff, and J. Greve, "Monte-Carlo Simulations of Laser Doppler Blood-Flow Measurements in Tissue," Applied Optics **29**, 2371-2381 (1990).

71. V. G. Kolinko, F. F. M. deMul, J. Greve, and A. V. Priezzhev, "Acceleration of Monte-Carlo simulations of laser Doppler blood flowmetry by repeated use of photon trajectories.," Optical Diagnostics of Living Cells and Biofluids, Proceedings Of **2678**, 389-400, 560 (1996).

72. P. Li, S. N. Ma, and Y. Liu, "3-Layered Model Monte-Carlo Simulation of Skin for Laser Doppler Blood-Flow Measurement," International Conference on Photodynamic Therapy and Laser Medicine **1616**, 591-595, 628 (1993).

73. A. Liebert, N. Zolek, and R. Maniewski, "Decomposition of a laser-Doppler spectrum for estimation of speed distribution of particles moving in an optically turbid medium: Monte Carlo validation study," Physics in Medicine and Biology **51**, 5737-5751 (2006).

74. V. Rajan, B. Varghese, T. G. Van Leeuwen, and W. Steenbergen, "Depth sensitivity of laser Doppler perfusion imager: Quantification based on experiments and Monte Carlo simulations on static and dynamic scattering phantoms - art. no. 644506," P Soc Photo-Opt Ins **6445**, 44506-44506, 44236 (2007).

75. W. Rutten, T. Gellekum, and K. Jessen, "Investigation of Laser Doppler Techniques Using the Monte Carlo Method," Photon Transport in Highly Scattering Tissue, Proceedings Of **2326**, 277-288, 518 (1995).

76. G. Soelkner, G. Mitic, and R. Lohwasser, "Monte Carlo simulations and laser Doppler flow measurements with high penetration depth in biological tissuelike head phantoms," Applied Optics **36**, 5647-5654 (1997).

77. P. Starukhin, N. Kharish, A. Karpovitch, A. Lepilin, S. Ulyanov, and V. Tuchin, "Monte-Carlo simulation of Doppler shift for laser light propagation in human teeth," Photon Propagation in Tissues Iii, Proceedings Of **3194**, 429-434, 532 (1998).

78. P. Starukhin, S. Ulyanov, and V. Tuchin, "Monte-Carlo simulation of Doppler shift for laser light propagation in a highly scattering medium," International Workshop on Nonlinear Dynamics and Structures in Biology and Medicine: Optical and Laser Technologies **3053**, 42-47, 200 (1997).

79. M. D. Stern, "2-Fiber Laser Doppler Velocimetry in Blood - Monte-Carlo Simulation in 3 Dimensions," Applied Optics **32**, 468-476 (1993).

80. D. Arifler, R. A. Schwarz, S. K. Chang, and R. Richards-Kortum, "Reflectance spectroscopy for diagnosis of epithelial precancer: model-based analysis of fiber-optic probe designs to resolve spectral information from epithelium and stroma," Applied Optics **44**, 4291-4305 (2005).

81. F. Jaillon, W. Zheng, and Z. W. Huang, "Half-ball lens couples a beveled fiber probe for depth-resolved spectroscopy: Monte Carlo simulations," Applied Optics **47**, 3152-3157 (2008).

82. K. Jorgensen, A. Klinger, and R. L. Biltonen, "Nonequilibrium lipid domain growth in the gel-fluid two-phase region of a DC16PC-DC22PC lipid mixture investigated by Monte Carlo computer simulation, FT-IR, and fluorescence spectroscopy," Journal of Physical Chemistry B **104**, 11763-11773 (2000).

83. S. Mark, A. Salman, N. Grossman, J. Gopas, R. K. Sahu, and S. Mordechai, "Fluorescence Spectroscopy of H-ras Transfected Murine Fibroblasts: A Comparison with Monte Carlo Simulations," Biopolymers **93**, 132-140 (2010).

84. I. Pavlova, C. R. Weber, R. A. Schwarz, M. D. Williams, A. M. Gillenwater, and R. Richards-Kortum, "Fluorescence spectroscopy of oral tissue: Monte Carlo modeling with site-specific tissue properties," Journal of Biomedical Optics **14**, - (2009).

85. T. J. Pfefer, L. S. Matchette, A. M. Ross, and M. N. Ediger, "Selective detection of fluorophore layers in turbid media: the role of fiber-optic probe design," Optics Letters **28**, 120-122 (2003).

86. B. W. Pogue, and T. Hasan, "Quantitative fluorescence measurements from tissue using confocal detection," Laser-Tissue Interaction Viii, Proceedings Of **2975**, 202-207,462 (1997).

87. D. Arifler, C. MacAulay, M. Follen, and R. Richards-Kortum, "Spatially resolved reflectance spectroscopy for diagnosis of cervical precancer: Monte Carlo modeling and comparison to clinical measurements," Journal of Biomedical Optics **11**, - (2006).

88. S. H. Choi, "Fast and robust extraction of optical and morphological properties of human skin using a hybrid stochastic-deterministic algorithm: Monte-Carlo simulation study," Lasers Med Sci **25**, 733-741 (2010).

89. R. Zhang, W. Verkruysse, B. Choi, J. A. Viator, B. Jung, L. O. Svaasand, G. Aguilar, and J. S. Nelson, "Determination of human skin optical properties from spectrophotometric measurements based on optimization by genetic algorithms," Journal of Biomedical Optics **10**, 024030 (2005).

90. C. F. Zhu, G. M. Palmer, T. M. Breslin, J. Harter, and N. Ramanujam, "Diagnosis of breast cancer using fluorescence and diffuse reflectance spectroscopy: a Monte-Carlo-model-based approach," Journal of Biomedical Optics **13**, - (2008).

91. T. J. Pfefer, K. T. Schomacker, M. N. Ediger, and N. S. Nishioka, "Multiple-fiber probe design for fluorescence spectroscopy in tissue," Applied Optics **41**, 4712-4721 (2002).

92. C. F. Zhu, Q. Liu, and N. Ramanujam, "Effect of fiber optic probe geometry on depth-resolved fluorescence measurements from epithelial tissues: a Monte Carlo simulation," J. Biomed. Opt. **8**, 237-247 (2003).

93. E. Alerstam, S. Andersson-Engels, and T. Svensson, "White Monte Carlo for time-resolved photon migration," Journal of Biomedical Optics **13**, - (2008).

94. A. Liebert, H. Wabnitz, N. Zolek, and R. Macdonald, "Monte Carlo algorithm for efficient simulation of time-resolved fluorescence in layered turbid media," Optics Express **16**, 13188-13202 (2008).

95. J. Peter, and R. B. Schulz, "Time-resolved Monte Carlo simulation of optical and isotopic photons in hybrid phantoms," Ieee Nucl Sci Conf R, 2926-2928, 4698 (2004).

96. B. Y. Yu, H. Li, L. Q. Xu, and S. S. Xie, "Time-resolved diffuse spectroscopy in multilayer tissue and its Monte Carlo simulation - art. no. 60850R," Complex Dynamics and Fluctuations in Biomedical Photonics III **6085**, R850-R850, 208 (2006).

97. W. Verkruysse, G. W. Lucassen, J. F. de Boer, D. J. Smithies, J. S. Nelson, and M. J. C. van Gemert, "Modelling light distributions of homogeneous versus discrete absorbers in light irradiated turbid media," Phys. Med. Biol. **42**, 51-65 (1997).

98. L. Wang, and S. Jacques, "Monte Carlo Modeling of Light Transport in Multi-Layered Tissues in Standard C," (1992).

99. J. Wu, M. S. Feld, and R. P. Rava, "Analytical Model for Extracting Intrinsic Fluorescence in Turbid Media," Applied Optics **32**, 3585-3595 (1993).

100. "Tattoo," (2010), http://en.wikipedia.org/wiki/Tattoo (Accessed 10 2009).

101. S. L. Jacques, and M. Keijzer, "Dosimetry for lasers and light in dermatology: Monte Carlo simulations of 577-nm pulsed laser penetration into cutaneous vessels," in *Lasers in Dermatology and Tissue Welding* (SPIE Los Angeles, CA, USA 1991), pp. 2-13.

102. M. J. C. Van Gemert, S. L. Jacques, H. J. C. M. Sterenborg, and W. M. Star, "Skin Optics," IEEE Trans. Biomed. Eng. **36**, 1146-1154 (1989).

103. S. L. Jacques, S. Rastegar, M. Motamedi, S. L. Thomsen, J. A. Schwartz, J. H. Torres, and I. Mannonen, "Liver photocoagulation with diode laser (805 nm) versus Nd:YAG (1064 nm)," in *Laser-Tissue Interaction III*(SPIE, Los Angeles, CA, USA, 1992), pp. 107-117.

104. R. Long, and M. J. McShane, "Modeling of selective photon capture for collection of fluorescence emitted from dermally-implanted microparticle sensors," Conf. Proc. IEEE Eng. Med. Biol. Soc. **2007**, 2972-2975 (2007).

105. L. Wang, S. L. Jacques, and L. Zheng, "Conv—convolution for responses to a finite diameter photon beam incident on multi-layered tissues," Computer Methods and Programs in Biomedicine **54**, 141-150 (1997).

106. R. Long, S. Singh, and M. McShane, "Stability of response and in vivo potential of microparticle glucose sensors," L. C. Gerard, and V. P. Alexander, eds. (SPIE, 2008), p. 686307.

107. A. N. S. Institute, "Safe Use of Lasers," (1993), Accessed Z136.1

108. B. W. Pogue, and M. S. Patterson, "Review of tissue simulating phantoms for optical spectroscopy, imaging and dosimetry," Journal of Biomedical Optics **11** (2006).

109. B. Drexler, J. L. Davis, and G. Schofield, "Diaphanography in the diagnosis of breast cancer," Radiology **157**, 41-44 (1985).

110. J. Linford, S. Shalev, J. Bews, R. Brown, and H. Schipper, "Development of a tissue-equivalent phantom for diaphanography," Medical Physics **13**, 869-875 (1986).

111. D. J. Watmough, "Diaphanography - Mechanism Responsible for the Images," Acta Radiol Oncol **21**, 11-15 (1982).

112. D. J. Watmough, "Transillumination of breast tissues: factors governing optimal imaging of lesions," Radiology **147**, 89-92 (1983).

113. S. T. Flock, B. C. Wilson, and M. S. Patterson, "Total attenuation coefficients and scattering phase functions of tissues and phantom materials at 633 nm," Medical Physics **14**, 835-841 (1987).

114. L. I. Grossweiner, "Optical Dosimetry in Photodynamic Therapy," Lasers in Surgery and Medicine **6**, 462-466 (1986).

115. L. I. Grossweiner, J. H. Hill, and R. V. Lobraico, "Photodynamic Therapy of Head and Neck Squamous-Cell Carcinoma - Optical Dosimetry and Clinical-Trial," Photochemistry and Photobiology **46**, 911-917 (1987).

116. S. L. Jacques, and S. A. Prahl, "Modeling Optical and Thermal Distributions in Tissue during Laser Irradiation," Lasers in Surgery and Medicine **6**, 494-503 (1987).

117. W. M. Star, "Light dosimetry in vivo," Physics in Medicine and Biology **42**, 763-787 (1997).

118. W. M. Star, J. P. Marijnissen, and M. J. van Gemert, "Light dosimetry in optical phantoms and in tissues: I. Multiple flux and transport theory," Physics in Medicine and Biology **33**, 437-454 (1988).

119. D. T. Delpy, M. Cope, P. V. d. Zee, S. R. Arridge, S. Wray, and J. S. Wyatt, "Estimation of optical pathlength though tissue from direct time of flight measurement," Phys. Med. Biol **33**, 1433-1442 (1988).

120. T. J. Farrell, M. S. Patterson, and B. Wilson, "A diffusion theory model of spatially resolved, steady-state diffuse reflectance for the noninvasive determination of tissue optical properties in vivo," Medical Physics **19**, 879-888 (1992).

121. M. Firbank, M. Oda, and D. T. Delpy, "An improved design for a stable and reproducible phantom material for use in near-infrared spectroscopy and imaging," Physics in Medicine and Biology **40**, 955-961 (1995).

122. S. L. Jacques, "Time resolved propagation of ultrashort laser pulses within turbid tissues," Applied Optics **28**, 2223-2229 (1989).

123. S. J. Madsen, B. C. Wilson, M. S. Patterson, Y. D. Park, S. L. Jacques, and Y. Hefetz, "Experimental tests of a simple diffusion model for the estimation of scattering and absorption coefficients of turbid media from time-resolved diffuse reflectance measurements," Applied Optics **31**, 3509-3517 (1992).

124. M. S. Patterson, B. Chance, and B. C. Wilson, "Time resolved reflectance and transmittance for the non-invasive measurement of tissue optical properties," Applied Optics **28**, 2331-2336 (1989).

125. B. Chance, S. Nioka, J. Zhang, E. F. Conant, E. Hwang, S. Briest, S. G. Orel, M. D. Schnall, and B. J. Czerniecki, "Breast cancer detection based on incremental biochemical

and physiological properties of breast cancers: a six-year, two-site study," Acad Radiol **12**, 925-933 (2005).

126. C. E. Cooper, and R. Springett, "Measurement of cytochrome oxidase and mitochondrial energetics by near-infrared spectroscopy," Philos Trans R Soc Lond B Biol Sci **352**, 669-676 (1997).

127. E. Gratton, S. Fantini, M. A. Franceschini, G. Gratton, and M. Fabiani, "Measurements of scattering and absorption changes in muscle and brain," Philos Trans R Soc Lond B Biol Sci **352**, 727-735 (1997).

128. D. J. Hawrysz, and E. M. Sevick-Muraca, "Developments toward diagnostic breast cancer imaging using near-infrared optical measurements and fluorescent contrast agents," Neoplasia **2**, 388-417 (2000).

129. J. C. Hebden, "Advances in optical imaging of the newborn infant brain," Psychophysiology **40**, 501-510 (2003).

130. B. W. Pogue, J. D. Pitts, M. A. Mycek, R. D. Sloboda, C. M. Wilmot, J. F. Brandsema, and J. A. O'Hara, "In vivo NADH fluorescence monitoring as an assay for cellular damage in photodynamic therapy," Photochemistry and Photobiology **74**, 817-824 (2001).

131. B. C. Wilson, P. J. Muller, and J. C. Yanch, "Instrumentation and Light Dosimetry for Intraoperative Photodynamic Therapy (Pdt) of Malignant Brain-Tumors," Physics in Medicine and Biology **31**, 125-133 (1986).

132. P. R. Cooper, "Refractive-Index Measurements of Paraffin, a Silicone Elastomer, and an Epoxy-Resin over the 500-1500-Nm Spectral Range," Appl. Opt. **21**, 3413-3415 (1982).

133. F. P. Bolin, L. E. Preuss, R. C. Taylor, and R. J. Ference, "Refractive-Index of Some Mammalian-Tissues Using a Fiber Optic Cladding Method," Appl. Opt. **28**, 2297-2303 (1989).

134. M. Lualdi, A. Colombo, B. Farina, S. Tomatis, and R. Marchesini, "A phantom with tissue-like optical properties in the visible and near infrared for use in photomedicine," Laser Surg. Med. **28**, 237-243 (2001).

135. "Mie scattering calculater," http://omlc.ogi.edu/calc/mie_calc.html (Accessed 09 2009).

136. "Inverse adding-doubling," http://omlc.ogi.edu/software/iad/index.html (Accessed 09 2009).

137. S. Prahl, "Inverse Adding-Doubling for optical property measurements," (2007), http://omlc.ogi.edu/software/iad/ (Accessed 09 2010).

138. S. A. Prahl, M. J. C. Vangemert, and A. J. Welch, "Determining the Optical-Properties of Turbid Media by Using the Adding-Doubling Method," Appl. Opt. **32**, 559-568 (1993).

139. A. N. Bashkatov, E. A. Genina, V. I. Kochubey, and V. V. Tuchin, "Optical properties of human skin, subcutaneous and mucous tissues in the wavelength range from 400 to 2000 nm," Journal of Physics D-Applied Physics **38**, 2543-2555 (2005).

140. "Skin Optics," http://omlc.ogi.edu/news/jan98/skinoptics.html (Accessed 07 2011).

141. S. L. Jacques, R. D. Glickman, and J. A. Schwartz, "Internal absorption coefficient and threshold for pulsed laser disruption of melanosomes isolated from retinal pigment epithelium," L. J. Steven, ed. (SPIE, 1996), pp. 468-477.

142. S. L. Jacques, and D. J. McAuliffe, "The melanosome: threshold temperature for explosive vaporization and internal absorption coefficient during pulsed laser irradiation," Photochem Photobiol **53**, 769-775 (1991).

143. S. A. Prahl, "Light Transport in Tissue," (University of Texas at Austin, 1988)PhD.

144. E. K. Chan, B. Sorg, D. Protsenko, M. ONeil, M. Motamedi, and A. J. Welch, "Effects of compression on soft tissue optical properties," IEEE J. Sel. Topics. Quantum Electron. **2**, 943-950 (1996).

145. V. V. Tuchin, S. R. Utz, and I. V. Yaroslavsky, "Tissue Optics, Light-Distribution, and Spectroscopy," Opt. Eng. **33**, 3178-3188 (1994).

146. S. Wan, R. R. Anderson, and J. A. Parrish, "Analytical Modeling for the Optical-Properties of the Skin with in vitro and in vivo Applications," Photochemistry and Photobiology **34**, 493-499 (1981).

147. R. R. Anderson, and J. A. Parrish, "The Optics of Human-Skin," Journal of Investigative Dermatology **77**, 13-19 (1981).

148. S. L. Jacques, "Origins of tissue optical properties in the UVA, visible, and NIR regions," in *OSA TOPS on Advances in Optical Imaging and Photon Mirgration*(1996), pp. 364-369.

149. S. L. Jacques, C. A. Alter, and S. A. Prahl, "Angular dependence of HeNe laser light scattering by human dermis," Lasers Life Sci **1**, 309-333 (1987).

150. J. M. Lerner, and A. Thevenon, "The optics of spectroscopy," http://www.astronomiainumbria.org/advanced_internet_files/spettroscopia/Teoria/reticoli_teoria/Optics_Spectroscopy.pdf.

151. "Dispersion (optics)," http://en.wikipedia.org/wiki/Dispersion_(optics) (Accessed 09 2011).

152. "Diffraction grating handbook," http://gratings.newport.com/library/handbook/handbook.asp (Accessed 08 2011).

153. C. Palmer, "Diffraction grating handbook," http://optics.sgu.ru/~ulianov/Students/Books/Applied_Optics/E.%20Loewen%20Diffraction%20Grating%20Handbook%20(2005).pdf (Accessed 10 2011).

154. "Grating selection guide," http://www.thorlabs.com/NewGroupPage9.cfm?ObjectGroup_ID=1123 (Accessed 09 2011).

155. I. J. Wilson, "Spectrograph Mount Grating Efficiency," J Opt **9**, 45-49 (1978).

156. "Absolute efficiency of gratings," www.thorlabs.com (Accessed 09 2011).

157. "Basics of spectral measurement," (2005), http://www.jeti.com/cms/images/Jeti_com/down/Basics/basics.pdf (Accessed 10 2011), Accessed 2.

158. "Charge-coupled device," http://en.wikipedia.org/wiki/Charge-coupled_device (Accessed 10 2011).

159. "Photodiode," http://en.wikipedia.org/wiki/Photodiode (Accessed 10 2011).

160. "CMOS," http://en.wikipedia.org/wiki/Cmos (Accessed 10 2011).

161. "CCD vs CMOS," http://www.teledynedalsa.com/corp/markets/ccd_vs_cmos.aspx (Accessed 01 2012).